MANIPULATION OF SINGLE DNA MOLECULES THROUGH NANO-FLUDIC DEVICES:
SIMULATION AND THEORY

Yanqian Wang

A dissertation submitted to the faculty at the University of North Carolina at Chapel Hill in partial fulfillment of the requirements for the degree of Doctor of Philosophy in the Department of Physics.

Chapel Hill
2016

Approved by:

Adam R. Hall

Jack Ng

Richard Superfine

Sean Washburn

Yue Wu

ABSTRACT

Yanqian Wang: Manipulation of Single DNA Molecules through Nano-fludic Devices: Simulation and Theory
(Under the direction of Michael Rubinstein)

Nanofludic platforms such as solid-state nanopores and nanochannels enable the manipulation of DNA molecules and have the potential to be a low-cost and high-efficiency DNA sequencing device.

DNA nanopore translocation is a process where DNA moves from one chamber to another through a nanopore. To get into the pore, the molecule entropy decreases and free energy increases. In order to thread the DNA throughout the pore, an electric bias is applied to overcome the entropic energy barrier. The occupation of DNA impedes the ion transport and creates a blockage current of which the amplitude and duration provide the information on the DNA sequence since different bases (or base pairs) can be discriminated through different magnitude of blockage. Mining DNA sequence from the electric current profile requires an accurate knowledge of the passage time of a given base along the molecule. Our model assumes that the translocation process at high fields proceeds too fast for the chain to relax, and thus the distribution of translocation times of a given monomer are controlled by the initial conformation of the chain (the distribution of its loops). The model predicts the translocation time distribution is determined by the distribution of initial conformation as well as by the thermal fluctuations to the conformation during the translocation process.

Narrow nanochannels require high threshold electric fields to achieve DNA translocation, leading to short dwell times of DNA in these channels. Nano-funnels integrated with nano-channels reduce the free energy barrier and lower the threshold electric field required for DNA translocation. A focused electric field within the funnel increases the electric force on the DNA, compresses the molecule, and increases the osmotic pressure at the nano-channel entrance which facilitates the entry at lower electric fields. Besides controlling the speed of the molecule's movement, appropriately designed nano-funnels such as parabolic shaped ones can also function as tweezers that allow the trapping and stable control of the position of the DNA molecule. A combination of a series of nano-funnels devices enable a wider range of location and speed manipulation and can assist genome mapping and sequencing when equipped with base detector.

To my family, I couldn't have done this without you.

TABLE OF CONTENTS

LIST OF FIGURES

LIST OF ABBREVIATIONS AND SYMBOLS

a	diameter(width) of a polymer backbone
AFM	atomic force microscopy
b	Khun length
bp	basepair
c	concentration of monomers
c_s	salt concentration
ds-	double-stranded
DNA	deoxyribonucleic acid
e	elementary charge
E	electric field
E_t	threshold electric field
DL	Debye Layer
EOF	electro-osmotic flow
f_{conf}	confinement gradient force
f_{drag}	hydrodynamic drag force
f_{eh}	electrohydrodynamic force
f_{el}	electrostatic force
f_{elas}	elastic force
f_{osm}	osmotic gradient force
f_{stall}	stall force
F	free energy
F_{conf}	conformational part of the chain free energy
F_{ent}	entropic part of the chain free energy
F_{int}	interaction part of the chain free energy
g_T	number of monomers in a thermal blob
J_c	capture rate

k_B Boltzmann's constant

l_B Bjerrum length

l_p persistence length

L size of a polymer

$L_{channel}$ length of the nanochannel

L_{funnel} length of the nanofunnel

N degree of polymerization

q   charge per a Khun monomer

q_{eff} effective charge per a Kuhn monomer

q_{red} reduced charge per a Kuhn monomer

Q   hydraulic flux

r_D Debye screening length

R_e end-to-end distance

R_g radius of gyration

$R_{||}$ the longitude size of a polymer in a channel

ss-   single-stranded

t time

T absolute temperature

TEM   transmission electron microscopy

UNC   University of North Carolina (at Chapel Hill)

v   excluded volume of a monomer

V electrostatic potential

w effective width of a rod-like monomer

ΔF free energy barrier

ϵ_{LJ} interaction parameter of the Lennard-Jones potential

η solution viscosity

κ inverse Debye screening length, $r_D = \kappa^{-1}$

μ	electrophoretic mobility
ζ	friction coefficient
ξ	correlation length of a semidilute polymer solution
ξ_H	hydrodynamic screening length
ξ_T	thermal blob size
Π	polymeric osmotic pressure
τ	chain relaxation time
τ_{Rouse}	Rouse relaxation time
τ_{Zimm}	Zimm relaxation time

CHAPTER 1:   Introduction

Section 1.1:   DNA manipulation and sequencing

Accurate genome sequencing is the key to deciphering the secrets of life and is vital for both fundamental research and medical diagnostics. In the past few decades, researchers have been eagerly developing and improving sequencing technologies. In 1977, Frederick Sanger and colleagues[104] proposed a DNA sequencing method based on chain-terminating dideoxynucleotides by polymerase and analyze each piece of dideoxynucleotides. During sequencing, the target DNA molecule is cut at known sites into fragments and separated using gel electrophoresis. By measuring the length of these DNA fragments and overlapping them with the aid of a computational algorithm, genomic information can be constructed. The Sanger method was the basis of the 13-year Human Genome Project[72], and demonstrated great accuracy and has been widely used since then.

Although the Sanger method is the most accurate DNA sequencing technique available today, it suffers from several limitations, which result in its high cost and long processing times. For example, applying gel electrophoresis to measure the lengths of DNA fragments requires large quantities of samples, which means that time-consuming and expensive cell cultures must be performed to provide sufficient quantities of cells. In some cases, not all species of cells can be cultured, which prevents the Sanger method from being used to sequence these species genomes. Even if the target cell culture is available, the genome of those replicated cells may not be exactly the same as the original culture due to genomic instability, genetic heterogeneity, and laboratory selection of genotype. The second issue with the Sanger method is that the measurement of DNA fragment lengths is on an ensemble basis, which can average out heterogeneity that may have biological and clinical significance. The third issue is that efficiency in measuring these genome fragments can only be increased so much. The electrophoretic separation of DNA fragments is based on length-dependent reptation motion of DNA molecules in a gel or nanoarray. Increasing the electric field can potentially accelerate the process, but will stretch the molecule and fail to completely separate DNA fragments due to length-independent electrophoretic mobility. Once the sizes of the fragments are determined, a search for overlapping sequences of the fragments requires alignment with a pre-existing sequence of the genome. However, such sequence maps of the genome are often not known.

There are many other ways besides the Sanger method that enable researchers to study DNA, and

many of them involve the mechanical control of the molecules position and movement. The incorporation of the mechanical control of a single DNA molecule into the DNA sequencing platform can facilitate the sequencing[115, 92]. For example, there are several techniques used to mechanically manipulate DNA[13], including atomic force microscopy (AFM)[46], micropipettes[13], optical tweezers[26], and fixed force magnetic tweezers[92]. These techniques can be divided into either fixed-position methods, such as AFM, micropipettes, and optical traps, or fixed-force methods, like the magnetic trap technique.

Although these methods provide important information about DNA, there are advantages and drawbacks to all these techniques. For example, AFM can be used to image and stretch a single DNA molecule with high spatial positioning accuracy of up to 0.1 nm using a very stiff cantilever. However, AFM techniques generate more signal noise compared to other approaches. The micropipette technique is usually accomplished with a weaker cantilever to provide an additional mode of rotation compared to AFM manipulation. For both the optical and magnetic trapping methods, researchers tether a micron-sized bead to the free end of a DNA molecule. In an optical trap system, the bead is approximately 0.5 μm in size and is controlled via a trapping laser, which creates forces as high as 100 pN. Compared to the optical trapping method of DNA, the magnetic tweezer method provides easy rotation of the molecule and its weak stiffness results in a constant force that depends on bead size. Besides these DNA manipulation techniques, researchers have also adopted flow field systems[13] to study the static properties of the DNA molecule, such as tension when the molecule is stretched.

In addition to mechanical manipulation, electric fields can be utilized to control the position and movement of single DNA molecules. Once dissolved in aqueous solution, the backbone of DNA carries a negative charge which allows the electrostatic force to pull the molecule in the opposite direction of the electric field. The electric field applies force along the whole molecule rather than pulling only at the ends, which enables it not only to stretch the DNA molecule, but also to move it at various speeds. For example, an electric field can drive the DNA molecule in bulk solution at a constant speed, which is referred to as free electrophoresis[70, 53]. Both Sanger's method and nanopore sequencing platform[75, 84, 19] apply the electric field to drive DNA molecules. While the electric field is employed to separate DNA fragments through gel electrophoresis in Sanger's method, the nanopore allows a direct study of the sequences of the DNA molecules utilizing the electric field. The latter scenario involves adding an electric bias across a nanopore to create an electric field inside the pore and in its vicinity, which allows the DNA molecules to be captured near the nanopore. The single DNA molecule, once captured by the electric field, can be further threaded through the nanopore, which is referred to as translocation. Translocation of the DNA strand through the nanopore is otherwise unfavorable in the absence of an electric field due to the molecule's increased conformational free energy. Similar dynamic processes in a restricted environment, such as a nanochannel[96, 51, 76], have

raised great research interest in recent decades.

Section 1.2:   Nanopore DNA sequencing

About two decades ago, a promising low-cost and high-throughput sequencing method was first introduced using a nanopore to perform single-molecule real-time sequencing. The nanopore is embedded into a thin membrane separating ionic buffer solution into two chambers - cis and trans. DNA molecules are initially placed in the cis chamber and an electric bias is applied across the membrane to drive the negatively charged DNA molecules to the trans side through the nanopore. During translocation, when the nanopore is partially occupied/blocked by a DNA strand, the resistance of the nanopore increases compared to its vacant state prior to and after translocation. Such a change in resistance can be monitored through the observation of ionic current passing through the nanopore under certain electric biases. In principle, the occupation of the nanopore with a different genomic base induces a distinct resistance. Therefore the passage of a molecule through the pore generates a temporal pattern of ionic current from which the DNA sequence can be read. The whole idea is to transform the spatial sequence of a DNA molecule into easily observed temporal signals, i.e. electric current traces . Although the invention of an orifice-based sensor appeared as early as the 1940s by Coulter[W.R. Hogg], in which the transport of blood cells through a pore allowed researchers to count and size the analytes, the leap of using a nanopore platform to sequence DNA did not occur until 1996, with the work of Kasianowicz *et al.*[43].

1.2.1:   Protein nanopores

In the work of Kasianowicz *et al.*[43], the authors embed an α-hemolysin protein pore into a lipid bilayer. They then introduce single-stranded poly(U) RNA homopolymers into the cis chamber and force the molecules to pass through the protein nanopore using an applied electric bias. In their study, Kasianowicz *et al.* observed three distinct current blockades. The blockade with the shortest dwell time was interpreted as the collision of RNA molecules with the nanopore orifice. The other two types of blockades corresponded to RNA translocation events featuring two different entry orientations (i.e., entry with either the 3' or 5" terminus of the RNA molecule). The authors observed that each passage event provided a trace of blockage current, which indicated at least three features of the translocation process, including dwell time, current levels, and rate of events. Translocation dwell time depends on molecules length and the events rate is linked to the concentration of the analytes. The levels of the current in principle can tell the sequence of the DNA/RNA molecule.

Using a nanopore to discriminate between nucleic acids was later attempted by Akeson and co-workers

[3], who studied how the current signal changed for different RNA and DNA molecules. In their work, the purine poly(A) molecule resulted in deeper blockages of current compared to the poly-pyrimidine poly(C) and poly(U) molecules; an observation which could not otherwise be explained by its primary structure and therefore was attributed to its voluminous secondary structure . In addition, the authors demonstrated a clear two-level current pulse during the translocation of a block co-polymer made of bases C and A. Meller *et al.* [74] also showed the capability of the α-hemolysin nanopore in distinguishing homopolymers and heteropolymers composed of nucleobases dA and dC .

A recently commercialized version of a protein nanopore based genome sequencing device was recently realized with the development of the MinION from Oxford Nanopore Technology. This $1000 device shows improved sequencing accuracy and has gained the attention of many researchers since its debut in 2015. The MinION can read up to 98 kilobases in length, though the average length is about 1 or 2 kilobases, with accuracies of greater than 90% [60].

Although the MinION uses enzymes as regulators to control the speed of translocation to improve the resolution, the reading precision is fundamentally limited by the simultaneous contribution of many bases to the current signal. More sophisticated algorithms, such as the Hidden Markov Model, have been applied to alleviate such difficulties. When these algorithms are paired with alignment strategies, the read-out accuracy can be improved by up to 99% for some analytes [42], which is comparable to other real-time sequencing technologies, such as SMRT [22], though still well below the accuracy of the Sanger sequencing method, which has an overall accuracy on the order of 99.95% [60].

1.2.2:   Solid-state nanopores

Although protein-based nanopores have atomically precise dimensions and consistent pore-molecule interactions, they are also fragile given the imperfect stability of the lipid bilayer. The dimensions of protein nanopores are also not tunable, which is a drawback for experimental design.

As an alternative to protein nanopores, solid-state nanopores, such as those fabricated from silicon nitride (SiN) have also demonstrated the power to discriminate among different nucleic acid polymers[35]. In contrast, solid-state nanopores are more flexible in terms of dimension and shape, and they are robust under many different thermal and chemical conditions [58], unlike protein nanopore experiments.

It is theoretically possible to create solid-state nanopores of any desired size, although current fabrication technology is unable to achieve as high a precision compared to protein nanopores[11]. In addition, even though the fabrication of some nanopores can be controlled with sub-nanometer precision [6], the thickness of the solid-state nanopore is overall greater than protein pores [58]. This is disadvantageous, because thicker

membranes and nanopores tend to enable greater numbers of translocating bases to contribute to the current signal, which complicates and lowers the accuracy of the sequence read-out. Despite the unsatisfactory status quo of fabrication, solid-state nanopores are generally easier to fabricate into arrays for parallel analysis [120], and integrate with other electronic [85] and optical devices [73].

Since a thick membrane results in the occupation of multiple nucleobases inside the nanopore and thus their simultaneous contributions to the electrical current signal. This makes it difficult to identify bases from the current traces. The emergence of new membrane materials enables researchers to fabricate ultra-thin nanopores. For example, a nanopore fabricated on a graphene membrane can be as thin as 0.34 nm, which is comparable to the size of a single nucleotide and much smaller than the 12-nucleotides long β-barrel region of a α-hemolysin nanopore [75]. Other promising substrates for nanopore fabrication include boron nitride (BN) and molybdenum disulfide (MoS2), the membranes of which can be just 1.1 nm [62] and 0.65 nm thick, respectively [61, 23].

Researchers have found that these kinds of ultra-thin nanopores have stronger interactions with DNA molecules, which is a double-edged sword[58]. Nanopores of thickness under 3 nm can slow the analytes translocation speed due to increased van der Walls interactions with the pore walls. Such intensified inter-actions can clog the pore and result in increased unreliability of the sequencing platform. Sometimes the material of the substrate itself can induce stronger interactions between the nanopore and analyte. For ex-ample, the slow translocation time of single-stranded DNA (ssDNA) through a graphene nanopore compared to a silicon nanopore of the same size is attributed to the hydrophobic adsorption of ssDNA to the graphene membrane [79, 38].

One large remaining challenge in solid-state nanopore sequencing is the rapidity of the translocation speed, which can be as fast as 30 base pairs(bp) per micro-second, faster than the allowed sequencing speed of around 1 bp per millisecond [58]. In general, a slower translocation speed can improve the temporal resolution of the read-out of the genome bases. Various strategies have been developed to slow down the translocation speed, such as by adding regulators to the DNA molecule[90] and changing the chemical/physical properties of the solvent and nanopore surface[15, 124, 114]. For example, lowering the temperature slows the motion of the ions and fluids, and also changes the DNA-nanopore interaction, leading to slower translocation speeds [119]. Researchers have also succeeded at elongating the translocation time by modulating the salt concentration and creating gradients between the cis and trans chambers[111, 118]. Decreasing the size of the counterions, $K^+ > Na^+ > Li^+$, can also slow down DNA molecules due to a different mechanism of binding counterions to DNA molecules[47].

Researchers have also found that the interaction between DNA and the nanopore accounts for the varia-tion of translocation speed under various experimental conditions[66, 119, 5, 52, 1]. This interaction between

the DNA and nanopore depends on the nanopore's shape, size and material. Aksimentiev *et al.* attributed the interaction to the hydrophobic adhesion between DNA and the nanopore walls [47]. In addition, cone-shaped nanopores can stretch double-stranded DNA (dsDNA) near the pore and facilitate the entry of the molecule due to the entropic interaction between the DNA and the nanopore [80]. In terms of material effects, researchers have observed that hafnium oxide (HfO2) nanopores slow DNA translocation by a factor of 10 compared to the same-sized nanopore made out of SiN [52]. Other nanopore membranes made of materials such as alumina oxide (Al2O3), BN, and graphene also slow translocation speeds by one order of magnitude in comparison to silicon counterparts [2, 62, 117]. Such slow-down was attributed to either the entropic, hydrophobic adhesion [4] or a contact friction [65] between DNA and the material inside nanopore wall.

The DNA and nanopore interaction is also tunable through modification of the nanopore's surface charge. The surface charge affects translocation by changing the electroosmotic flow and the electrostatic interaction of DNA and the nanopore wall. For instance, the negative charge on SiN nanopore walls can be inverted to positive by coating the surface with a pH-sensitive polymeric cushion[5]. Although this method can change the surface charge density by a factor of 5 under feasible experimental conditions, it increases noise in the current signal due to a higher membrane capacitance.

Hydraulic pressure is another way to control the translocation speed of the DNA molecule by exerting a hydrodynamic force on the DNA in addition to the electric-field-induced force. By carefully adjusting the pressure, the translocation time can be prolonged by at least an order of magnitude[64]. The pressure-induced force is independent of the analytes charge, which allows this hydraulic pressure method to manipulate neutral polymers.

The interplay of hydraulic pressure and electric-fields can trap DNA in the nanopore and result in ultra-long translocation processes [37, 7, 125]. For the slow translocation events, the translocation dynamics are different from those in the "fast" region of translocation events, for which non-equilibrium dynamics of the molecule apply. Slow translocation events allow the molecule to relax during the process. The first passage time analysis with Fokker-Planck equation can study the behavior in this regime[82, 83, 37]. One advantage of pressure modulated translocation over other methods, such as surface charge modification, is that it will not decrease the capture rate of the analyte or increase the noise of the current signal.

Mechanical devices can also be integrated into the nanopore sequencing system to help regulate the speed of translocation. For example, Keyser *et al.*[45] developed optical tweezers that could mechanically control a single DNA molecule by attaching a laser-steered bead to the end of that molecule. The deviation of the bead position from the focal point produces a restoring force on the bead, which is eventually transferred to the DNA. A balance of the stall/restoring forces, along with the electrical force, helps immobilize the

molecule. The magnitude of the electrical force can be obtained by measuring the displacement of the bead away from the focal point. In Keyser *et al.*'s experiments, dsDNA was found to have an effective charge of 0.5 e per base pair[44]. In their later experiments applying optical tweezers, the authors learned that the stall force increased with the decreasing nanopore size. Using this technique, they were able to reduce the translocation speed to 0.1 bp per millisecond, a reduction by 5 orders of magnitude[45].

Other mechanical control methods include magnetic tweezers, in which a magnetic field gradient is used to manipulate a DNA molecule that has been previously tethered to a magnetic-field-controlled bead[92]. However, the challenge of these mechanical strategies lies in the precise control of the bead. The Brownian motion of the bead and the molecule, especially when heated by a laser, decreases the resolution of the bead position, and at the same time increases the noise in the ionic current[58, 60, 108].

Besides slowing down the speed of translocation, researchers are developing new methods to better discriminate bases as they pass through the nanopore. One such method involves transverse electrodes, in which a pair of metal nanoelectrodes (such as freshly broken gold wires) are placed on the surface of the membrane at the location of the nanopore[127]. Zikic *et al.*[130] demonstrated that the tunneling current measured by the electrodes enabled the researchers to identify the four bases of ssDNA under different conditions of nanopore size and electric field strength [49, 50]. Another modification of this technology is to functionalize the transverse electrodes with different chemical reagents. When certain bases interact with the functionalized electrodes, they generate a transient tunneling current. The reagent can be customized to interact with different nucleotides. Since recognition is based on the transient current signal for each type of base, this method has the potential to realize sequencing under fast translocation speeds[39]. Other emerging methods to improve the distinguishability of bases includes the detection of current through nanogaps [94, 59] and graphene nanoribbon [79].

The rest of the dissertation has two parts. The first part aims to interpret the noise during the DNA translocation process and access its impact on the recognition of genome bases through nanopore sequencing platform. The second part introduces a novel nano-fluidic device- nano-funnel that can trap a single DNA molecule prior to its passage through the nano-channel and slow down the translocation process with prescribed funnel shapes.

CHAPTER 2: DNA Translocation through Nanopores

Polymer translocation through a nanopore is encountered in a number of biological processes and researchers have considered it as a possible method to achieve rapid gene sequencing. However, the molecular details of this process and even the dependence of translocation time on the polymer chain length are not completely understood. In this dissertation, we determined the distribution of translocation times for a given monomer of the polymer chain using both analytical calculations and 3D Langevin dynamic simulations of forced translocation. A theoretical model of forced translocation of a polymer chain through a nanopore is proposed in this chapter. The model allows one to calculate the translocation time of individual monomers within a polymer chain featuring a particular initial conformation. The results of the computer simulation confirm the dependence of monomer translocation time on the polymer chain conformation. This chapter also studies, both analytically and numerically, the broadening of the distribution of translocation times due to the distribution of initial conformations and the thermal fluctuations of the polymer chain during the translocation process.[1]

---

[1]This chapter is adapted from a manuscript that is contributed by Yanqian Wang, Sergey Panyukov, Qi Liao and Michael Rubinstein.

Section 2.1:   Introduction

The nanopore platform has shown promise as a low-cost, high-throughput genome sequencing method. Kasianowicz *et al.*[43] pioneered early experiments that studied the translocation of biological macromolecules through a nanoscale pore. The authors specifically investigated the passage of single-stranded RNA and DNA molecules in an electric field through a narrow ion channel in a lipid bilayer membrane. They found that blockaded ion current could be used to detect the passage of DNA or RNA through the channel and ideally identify individual nucleotides. The duration of this current blockage time was found to increase with the degree of polymerization, as described in the relationship $\tau_{trans} \propto N^{1.27}$, in which τ_{trans} is the translocation time and N is the polymer chain length.

Many subsequent experiments adopted Kasianowicz *et al.*'s method and emphasized the influence of the strength of the external field on the translocation time and translocation velocity of a biomolecule through a channel. For example, Meller *et al.*[75] measured the velocity of single-stranded DNA translocation driven by an electric field through a single α-hemolysin pore. Their results verified that polymers longer than the pore length transported at a constant speed, while the translocation velocity of shorter polymers increased inversely with the chain length. The translocation velocity increased nonlinearly with increased applied voltage.

These initial studies on nanopore technology eventually led to the recently commercialized MinION Nanopore[78] released by Oxford Nanopore Technologies, which has been widely used in genome sequencing research and has the ability to read genome of up to 10 kilobases with a 90% accuracy rate per base[60]. However, such accuracy is still well below Sangers sequencing method. The Oxford Nanopore is made of a protein nanopore embeded in a lipid layer. The base recognition is limited by the simultanous contribution to the current signals by multiple bases inside of the constriction part of the protein nanopore. Although applying a more sophisticated algorithm [54] to analyze the raw data such as the Hidden Markov Model[42] can improve the readout accuracy, the fixed dimension of Oxford Nanopore puts a restriction on the technology. Other researcher [56, 19, 79, 22, 105, 24, 32] seek to innovate the device itself. For instance solid state (SS) nanopore technology is more flexible in terms of dimensions and has the potential to enable single nucleotide read-out[112, 28, 60].

More recent experiments have focused on artificial SS nanopores [34], the dimensions of which can be systematically controlled[20]. In a typical experimental setup, a voltage potential is applied between two chambers, cis and trans, that have been separated by a membrane. The cis and trans chambers are connected by a single nanopore through the membrane. The potential creates a strong field both inside and near the nanopore. This field is what drags the polyelectrolyte chain, such as DNA, towards and through this channel.

(Compared to voltage-driven DNA translocation, the enzyme regulated translocation allows the passage of genome bases one at a time and results in a higher sequencing accuracy. But the experimental condition is also largely limited in order to keep the enzyme active.) If the polymer enters the pore, it blocks the measured ion current, providing information about the translocation process. Storm *et al.*[56] studied translocation of double-stranded DNA through a silicon oxide nanopore and found a power-law scaling of $\tau_{trans} \propto N^{1.27}$, which is different from the power-law relation obtained in many other results[27, 83]. Given the residence time as by far the most effective investigation tool for the translocation mechanism, different power-law relations of residence time will induce disparate or even conflicting fundamental understanding of the process. While studying polymer transolcation under a strong polymer-pore attraction, Krasilnikov *et al.*[48] observed that the residence time, the time duration that polymer occupies the nanopore, first increased and then decreased with molecular weight.

Besides experiments, a number of theoretical and simulation studies [40, 67, 29, 116, 10, 82, 9, 103, 55, 41, 27] has been devoted to the problem in the last decade. In the case of forced translocation, some researchers have claimed the dependence of $\tau_{trans} \propto N^{2\nu}$ for short chains, and $\tau_{trans} \propto N^{1+\nu}$ for long chains in the presence of an applied external field using a two-dimensional bond fluctuating model and two dimensional Langevin dynamics simulation, respectively [10, 40]. The Flory exponent ν is 0.5 for ideal chain and 0.588 for swollen chain. Lubensky and Nelson [66] introduced a coarse-grained microscopic model to study the time distribution for polymers to pass through a pore when the chain has strong interactions with the pore itself. The authors claimed that translocation speed significantly depends on the polymers interaction within the pore and the interaction also increases the skewness of the distribution of the residence times.

In spite of notable progress, the problem of polymer translocation is far from being completely understood. In particular, there have been few studies on the origin of the variation of forced translocation time for a DNA/RNA chain without hairpins. Most previous theoretical and computational research has focused on the average translocation time and its scaling dependence on polymer length and drag force. Although polymer conformation outside the pore is important for the dynamics of translocation, researchers have not accepted it as a primary factor controlling the distribution of translocation time.

In spite a notable progress, the problem of polymer translocation is far from being completely understood. In particular, there are few studies on the origin of the variation on forced translocation time of a chain without hairpins. Most previous theoretical and computational researches focus on the average translocation time and its scaling dependence on polymer length and drag force. Although polymer conformation outside the pore is important for the dynamics of translocation, researchers have not accepted it as a primary factor controlling the distribution of translocation time. This paper is aimed to evaluate the dependence of translocation time of a given monomer on polymer conformations before translocation. The translocation

time t_m is the time interval from the first monomer getting into the pore until monomer m entering the pore. Also we developed both analytical solution and Langevin simulations to estimate the width of translocation time distribution.

On the rest of this chapter, a theoretical model will first be developed, and the monomer translocation will be studied both under the model and through Langevin Dynamics simulations. Finally, the study of the distribution of translocation time will be compared for both approaches.

Section 2.2:   Model description

To study the behavior of DNA molecules under an electric field in a restricted environment, we can borrow concepts from polymer physics to deal with large-scale behaviors to obtain a "birds eye view" [83] and then pursue higher resolution analysis. In polymer physics, the biological molecule is modeled as a chain/polymer made of a number of connected segments/monomers while a charged molecule such as DNA in salty solution can be modeled as a polyelectrolyte[77, 101].

The basic physical properties of a DNA molecule consist of its contour length, persistence length, and effective width. The contour length is the size of the DNA molecule as it is stretched in a linear fashion. It can be calculated as the product of the total number of base pairs in the molecule and the height of a base pair (0.34 nm). Typically, λ-dsDNA with 48.5 kbp has a contour length of 16.5 μm, while T-4 dsDNA of 165 kbp has a contour length of 56 μm. The human (diploid) genome has 6 Gbp and its contour length can be as long as 2 m when fully stretched. However, DNA contour length is observed to increase once the DNA is labeled for imaging purposes with fluorescent stains. For example, when stained by YOYO-1, the contour length of λ-dsDNA increases to 21 μm[129].

The excluded volume interactions between segments of dsDNA, which determine the effective width of the molecule, come from two origins. First, the backbone of B-form dsDNA has been determined from the crystal structure to be about 2 nm in width, which creates a hardcore repulsive potential. Second, the negatively charged segments of DNA will repel each other due to the Coulombic effect, resulting in a larger effective width than just its backbone. The effective width also depends on the ionic strength of the solvent. Larger salt concentrations more effectively screen interactions between different strands of DNA. Such screening decreases the excluded volume of DNA strands and therefore the effective width. For example, the effective width of DNA is about 5 nm in a 0.1 M monovalent salt solution and can reach 20 nm in a 5 mM solution [97].

In general, ssDNA adopts a more flexible conformation, with a persistence length estimated to be around 2 nm, while hydrogen bonding and base stacking makes dsDNA rather stiff, with a persistence length of

about 50 nm. The persistence length of DNA depends on the ionic strength of the solvent due to Coulombic effects . It is found that persistence length decreases as the salt concentration increases due to screened Coulombic repulsion between segments before saturation, as explained by the Manning condensation theory [70]. The persistence length of dsDNA can be estimated as

$$l_p \approx 46.1nm + 6.3\lambda_D$$

where the Debye length, λ_D, at room temperature is estimated as a function of ionic strength, $I(M)$, in molar concentration,

$$\lambda_D(nm) \approx \frac{0.304}{\sqrt{cs(M)}}$$

[21].

Based on its dynamics, polymer translocation (PT) can be either active or passive. In the active case, the polymer is self-driven by either entropy or chemical potential, and stays in equilibrium during the whole process. Researchers have intensively studied the active translocation scenario using the Fokker-Planck equation under the assumption that the polymer has time to equilibrate/relax during the translocation process [83]. However, passive/forced translocation experiments usually proceed too fast for DNA to equilibrate, in which case t_m of the mth monomer is much shorter than the relaxation time,$\tau(m)$, of polymer segment of length m. Such fast translocation can be described by $t_m \ll \tau(m)$, which corresponds to a strong force F, $\frac{Fb}{k_B T} > \frac{1}{9\pi} m^{-\frac{1}{2}}$, pulling the chain in the pore. Only the study of fast, non-equilibrium translocation falls in the scope of this work.

In a translocation event, the chain is first captured [82, 115, 73] by the pore and pulled from the cis to trans side of the membrane partitioned chamber. Our model assumes the capture state of each polymer chain is fully relaxed on the cis side and with one end of the polymer pinned at the center of the pore. Once the monomer moves inside the pore, it will be pulled by the electrophoretic force in the presence of the pore's electric field. Under this pulling motion, monomers will move and the bonds between monomers will align towards the pore. However, not all monomers move at the same time. Only a monomer whose bond has been aligned with the pore will move, leaving the rest of the monomers on the cis side unperturbed by the pulling force. The moving velocity of the aligned monomer can be estimated from the balance of the pulling force at the pore, F, with the frictional drag, f , from the solvent.At the moment when the mth monomer is at the pore, monomers up to index m' are moving together towards the pore. They are assumed to have the same velocity, v_m, as well as friction coefficients, ξ. The number of monomers involved in moving $m' - m$ determines the speed of monomers in the pore, following $F = f = (m' - m) \cdot \xi \cdot v_m$ (Figure.2.1). Therefore,

the speed is determined by the chains conformation using the equation $m' - m = R_{m'}/b$, which is determined from the aligned conformation. After obtaining the traveling velocity, we can calculate the translocation time of the mth monomer (m could be any monomer indexed, from 0 to N) defined as the elapsed time from the initial captured state to the moment when the mth monomer is in the pore.

$$t_m \equiv \int_0^m \frac{b}{v_n} dn \qquad (2.1)$$

The translocation time of mth monomer, t_m, depends on the velocity and thus the conformation of the polymer chain. This connection between translocation time and conformation is referred to as fingerprinting. An identical polymer can adopt various initial conformations at the beginning of the translocation. Such variations independent of the translocation speed can deviate the translocation time from the average value by Δt. Even with the same inital conformation, the conformation can change during the translocation process due to the Brownian motion of each monomer. Under the assumption of fast/non-equilibrium translocation, the Brownian motion fluctuates the chain only on a local scale, as the translocation time is much smaller than chains relaxation time. This time-dependent variation in conformation adds additional fluctuation in time, δt. We show that those fluctuations can be deconstructed and examined through their dependence on system variables.

2.2.1: Brownian motion

The fundamental core of polymer dynamics begins with the study of Brownian motion[69]. Back in 1828, Robert Brown first experimentally observed the random motion of pollen particles suspended in water. This random motion became known as Brownian motion.

The theoretical side of Brownian motion was studied by Karl Pearson in 1905, who introduced the concept of the Pearson walk, though the solution to this problem was already known in Rayleigh's earlier work in 1880 and 1899 . Later, Einstein, Smoluchowski, and Langevin developed a theory for the time dependence of the position of a Brownian particle by idealizing Brownian motion as random walks. The famous Einsteinian relation gives the mean square displacement of the particle as proportional to the time elapsed with zero average displacement[83, 69].

$$\langle (x)^2 \rangle \propto time$$

2

---

[2]The angle brackets indicate that the variable inside is averaged over many random realizations of the process.

The Einstein relation describes the diffusion behavior of a particle, which has many random collisions with solvent molecules. In contrast, a qualitatively different motion is Newtonian motion, in which the distance traveled is the product of velocity and the time elapsed. This drift behavior is controlled by eternally imposed forces. The interplay of drift and diffusion can be investigated from theoretical formulisms, such as the Langevin and Fokker-Planck-Smoluchowski equations[69].

Smoluchowski equation and Langevin equation [69]   The Smoluchowski equation can be derived from the the generalization of the diffusion equation. By Fick's law, a macroscopic particle flux $j(x,t)$ is proportional to the gradient of the particle density in space, i.e. $j(x,t) = -D\frac{\partial c}{\partial x}$ where D is the diffusion coefficient. If there exists an external potential $U(x)$ with force $F = -\frac{\partial U}{\partial x}$, the particle moves with an average velocity $v = -\frac{1}{\zeta}\frac{\partial U}{\partial x}$, where ζ is friction coefficient and the particle is assumed large enough to fall into the classical scope. Combining both diffusion and drift effects, the flux is

$$j = -D\frac{\partial c}{\partial x} - \frac{c}{\zeta}\frac{\partial U}{\partial x} \tag{2.2}$$

The continuity equation relates the flux to the change of the particle density with respect to time:

$$\frac{\partial c}{\partial t} = -\frac{\partial j}{\partial x} \tag{2.3}$$

The Smoluchowski equation can be obtained using eq(2.2), eq(2.3) and Einstein relation $D = \frac{k_B T}{\zeta}$:

$$\frac{\partial c}{\partial t} = \frac{\partial}{\partial x}\frac{1}{\zeta}\left(k_B T\frac{\partial c}{\partial x} + c\frac{\partial U}{\partial x}\right) \tag{2.4}$$

Eq. 2.4 still holds if the density c is substituted by the probability distribution function $\psi(x,t)$ that a particle is found at location x and time t:

$$\frac{\partial \psi}{\partial t} = \frac{\partial}{\partial x}\frac{1}{\zeta}\left(k_B T\frac{\partial \psi}{\partial x} + \psi\frac{\partial U}{\partial x}\right) \tag{2.5}$$

One important point about the Smoluchowski equation is that if the potential is time-independent and there is no flux at the boundary, the distribution function ψ moves toward the equilibrium state that follows Boltzmann distribution:

$$\psi_{eq} = \frac{\exp(-\frac{U(x)}{k_B T})}{\int dx\exp(-\frac{U(x)}{k_B T})}$$

The Smoluchowski equation describes at least two possible states of solutions: the equilibrium state, in which the flux is zero; and a steady state solution, in which the system has a constant flux. In equilibrium,

the simplified equation for the one dimensional scenario can be written as:

$$\frac{1}{c(x)}\frac{\partial c(x)}{\partial x} = -\frac{\partial}{\partial x}\left(\frac{F(x)}{k_B T}\right)$$

This enables us to describe the particle concentration following the Boltzmann distribution:

$$c(x) = c_0 e^{-\frac{U(x)}{k_B T}}$$

By rearranging the Smoluchowski equation for the steady state as:

$$j(x) = -De^{-\frac{U(x)}{k_B T}}\frac{\partial}{\partial x}\left[c(x)e^{\frac{U(x)}{k_B T}}\right]$$

then both the concentration profile, $c(x)$, and the constant flux, $j(x) = j$, can be solved analytically once the free energy profiles are obtained. The concentration in the steady state is different from the one in equilibrium by an additional multiplier representing the flux effects:

$$c(x) = e^{-\frac{U(x)}{k_B T}}\left[c(0)e^{\frac{U(0)}{k_B T}} - \left(\frac{j}{D}\right)\int_0^x dx' e^{\frac{U(x)}{k_B T}}\right]$$

A representative application of the Fokker-Planck equation is the first hitting time problem, in which the particle undergoing a drift-diffusion process is either reflected or absorbed onto the boundaries. The active DNA translocation with the molecule equilibrated at each moment can be studied using the first-hitting-time model of a 1-D Brownian particle. In this model, the first hitting time (also known as first passage time) is the time the particle gets absorbed at x given its initial location at $x = 0$ at time $t = 0$ has a distribution

$$\psi(t) = \frac{|x|}{\sqrt{4\pi D t^3}}\exp(-\frac{x^2}{4Dt})$$

where D is the diffusion coefficient. Therefore the distribution of the first passage time of the active DNA translocation follows a Levy distribution, a skewed distribution with a fat tail.

An alternative perspective to study the Brownian motion is to examine the Langevin equation:

$$\zeta\frac{dx}{dt} = -\frac{\partial U}{\partial x} + f(t) \tag{2.6}$$

where the velocity of a particle is proportional to the sum of the forces exerted on it. The Langevin equation models the evolution of instantaneous velocity of a particle whose radius is much greater than the size of a single solvent molecule. It can be seen from above formula that Langevin equation is an extension of

Newton's law to include random forces. The random force fluctuates around zero average independently and is uncorrelated at different time moments. The random force $f(t)$ is assumed to have a Gaussian distribution:

$$\psi(f(t)) \propto \exp\left(-\frac{f(t)^2}{4\zeta k_B T}\right) \tag{2.7}$$

with moments

$$\langle f(t)\rangle = 0, \langle f(t)f(t')\rangle = 2\zeta k_B T \delta(t - t') \tag{2.8}$$

This assumption makes the Langevin equation equivalent to Smoluchowski equation.

If a free particle (zero drift) is at x_0 at $t = 0$, its position at time t is obtained from 2.6

$$x(t) = x_0 + \frac{1}{\zeta}\int_0^t dt' f(t')$$

Since the random force $f(t)$ is a Gaussian variable, $x(t)$, the linear addition of $f(t)$, is also a Gaussian variable. With the fact that

$$\langle x(t)\rangle = x_0$$

and

$$\langle (x(t) - x_0)^2\rangle = \frac{2k_B T}{\zeta}t = 2Dt$$

, the probability distribution of the single particle at time t is

$$\psi(x,t) = (4\pi Dt)^{-1/2}\exp\left(-\frac{(x - x_0)^2}{4Dt}\right) \tag{2.9}$$

Brownian motion of a single particle in a harmonic potential[69] A characteristic quantity describing the Brownian motion is the time correlation function $C_{AA}(t) = corr(A(t)A(0)) = \langle A(t)A(0)\rangle$. $C_{AA}(t)$ usually decreases with time for the correlation between $A(t)$ and $A(0)$ decreases. As time increases, the time correlation function $C_{AA}(t)$ approaches its asymptotic value $\langle A\rangle^2$ with a characteristic time scale called correlation time τ.

Consider the Brownian motion of a single particle in a harmonic potential $U = \frac{1}{2}kx^2$, where k is spring constant. The time correlation function of the location of the particle can be expressed as

$$\langle x(t)x(0)\rangle = \int dx \int dx' xx' G(x, x'; t)\psi_{eq}(x') \tag{2.10}$$

where the Green function $G(x, x'; t)$ is the probability density function finding a particle at location x at

16

time t given its location x' at time $t = 0$. Therefore the Green function is the solution to the Smoluchowski equation with the initial condition $G(x, x'; 0) = \delta(x - x')$.

$$\frac{\partial}{\partial t} G(x, x'; t) = \frac{1}{\zeta} \frac{\partial}{\partial x} \left(k_B T \frac{\partial G(x, x'; t)}{\partial x} + kxG(x, x'; t) \right) \tag{2.11}$$

Solving the PDE as eq(2.11) gives the solution

$$G(x, x'; t) = \left[\frac{2\pi k_B T}{k} \left(1 - \exp(-2t/\tau) \right) \right]^{-1/2} \exp \left[-\frac{k \left(x - x' \exp(-t/\tau) \right)^2}{2k_B T \left(1 - \exp(-2t/\tau) \right)} \right] \tag{2.12}$$

where $\tau = \zeta/k$ Although the explicit form of $G(x, x'; t)$ is unnecessary for obtaining the correlation time τ, it is helpful for the understanding the time evolution of the distribution.

In the case as $t \ll \tau$, the Green function exhibits the property of free diffusion, i.e.

$$G(x, x'; t) \simeq (4\pi Dt)^{-1/2} \exp \left(-\frac{(x - x')^2}{4Dt} \right) \tag{2.13}$$

In the other limit as $t \gg \tau$, the probability density function $G(x, x'; t)$ follows a time-independent Boltzmann distribution, i.e.

$$G(x, x'; t) \simeq \left(\frac{2\pi k_B T}{k} \right)^{-1/2} \exp \left(-\frac{kx^2}{2k_B T} \right) \tag{2.14}$$

The correlation time τ can be obtained through examining the decay rate of $\langle x(t)x(0) \rangle$.

$$\begin{aligned}
\frac{\partial}{\partial t} \langle x(t)x(0) \rangle &= \int dx \int dx' xx' \psi_{eq}(x') \left[\frac{1}{\zeta} \frac{\partial}{\partial x} \left(k_B T \frac{\partial G}{\partial x} + kxG \right) \right] \\
&= \int dx dx' G \psi_{eq}(x') \left[\frac{k_B T}{\zeta} \frac{\partial}{\partial x} \frac{\partial}{\partial x} (xx') - \frac{kx}{\zeta} \frac{\partial}{\partial x} (xx') \right] \\
&= -\frac{k}{\zeta} \int dx \int dx' xx' G(x, x't) \psi_{eq}(x') \\
&= -\frac{1}{\tau} \langle x(t)x(0) \rangle
\end{aligned} \tag{2.15}$$

where the step from the first line to second line use the trick of integral by parts. Consider the variance of x, $\langle x^2 \rangle = \frac{k_B T}{k}$, the time correlation function can be derived as

$$\langle x(t)x(0) \rangle = \frac{k_B T}{k} \exp(-t/\tau) \tag{2.16}$$

Since the characteristic time τ implies the time scale at which the memory of the initial state is lost, τ is also called relaxation time in polymer physics.

17

Similar results can be obtained from Langevin equation as well.

$$\zeta \frac{dx}{dt} = -kx + f(t) \tag{2.17}$$

with $\langle f(t) \rangle = 0$ and $\langle f(t)f(t') \rangle = 2\zeta k_B T \delta(t - t')$. The solution to eq(2.17) is

$$x(t) = \frac{1}{\zeta} \int_{-\infty}^{t} dt' \exp\left(-\frac{t - t'}{\tau}\right) f(t') \tag{2.18}$$

The time correlation function can be written as

$$\begin{aligned}
\langle x(t)x(0) \rangle &= \frac{1}{\zeta^2} \int_{-\infty}^{t} \int_{-\infty}^{0} dt_1 dt_2 \exp\left(-\frac{t - t_1 - t_2}{\tau}\right) \langle f(t_1)f(t_2) \rangle \\
&= \frac{2k_B T}{\zeta} \int_{-\infty}^{0} dt_2 \exp\left(-\frac{t - 2t_2}{\tau}\right) \\
&= \frac{k_B T}{k} \exp\left(-\frac{t}{\tau}\right)
\end{aligned} \tag{2.19}$$

Brownian motion of a single polymer chain [69]   Consider a polymer chain made of N beads and there is an interaction between two neighboring beads, referred to as a bond. There are $N - 1$ bonds in total. Let the position of nth bead be R_n and the objective is to study the dependence of the position vector $(R_1, R_2, \ldots R_N)$ on time t. The Brownian motion of a bead embedded within a chain is different from the Brownian motion of a free particle. For simplicity, the interaction in the bond is modeled as a spring potential $U = \frac{k}{2} \sum_{n=2}^{N} (R_n - R_{n-1})^2$. Therefore the Langevin equation associated with this potential is

$$\zeta \frac{dR_n}{dt} = -k(2R_n - R_{n+1} - R_{n-1}) + f_n(t) \tag{2.20}$$

with $n = 2, 3, \ldots, N - 1$. The random forces on different beads are uncorrelated to each other and their moments can be written as:

$$\langle f_n(t) \rangle = 0$$

$$\langle f_n(t) f_m(t') \rangle = 2\zeta k_B T \delta_{nm} \delta(t - t')$$

This is known as the Rouse model [69, 77]. For simplicity, we show here only the one-dimensional case of the system. However, the results of the three dimensional case differs from the one-dimensional one only up to a constant factor.

To simplify the problem, we first introduce two redundant variables R_0 and R_{N+1} with their values

$R_0 = R_1$ and $R_{N+1} = R_N$. Then eq(2.20) can be rewritten in continuous limit as

$$\zeta \frac{\partial R_n}{\partial t} = k \frac{\partial^2 R_n}{\partial n^2} + f_n(t) \tag{2.21}$$

with $n = 0, 1, \ldots, N$ and boundary conditions as

$$\frac{\partial R_n}{\partial n}\Big|_{n=0} = \frac{\partial R_n}{\partial n}\Big|_{n=N} = 0$$

The way to solve eq(2.21) is to adopt normal coordinates $(X_1, X_2, \ldots, X_N)$ defined as

$$X_p \equiv \frac{1}{N} \int_0^N dn \cos\left(\frac{p\pi n}{N}\right) R_n(t) \tag{2.22}$$

The inverse transformation is then

$$R_n = X_0 + 2 \sum_{p=1}^{\infty} X_p \cos\left(\frac{p\pi n}{N}\right)$$

, where X_0 represents the position of the centre of mass $\frac{1}{N} \int dn R_n = X_0$.

Equation 2.21 can be rewritten using normal coordinates as

$$\zeta_p \frac{\partial}{\partial t} X_p = -k_p X_p + f_p(t) \tag{2.23}$$

where

$$\zeta_0 = N\zeta; \quad \zeta_p = 2N\zeta, \text{ for } p = 1, 2, \ldots, N$$

$$k_p = \frac{2\pi^2 k}{N} p^2$$

$$\langle f_p(t) \rangle = 0$$

$$\langle f_p(t) f_q(t') \rangle = 2\delta_{pq} k_B T \delta(t - t')$$

As seen adopting the normal coordinates dissociates the correlation between the positions of different beads and reduces the problem to the one of a single particle at a harmonic potential. Applying the solution 2.19 to get the time correlation function of the center of mass X_0

$$\langle (X_0(t) - X_0(0))^2 \rangle = \frac{2k_B T}{N\zeta} t \tag{2.24}$$

19

and

$$\langle X_p(t)X_q(0)\rangle = \delta_{pq}\frac{k_BT}{k_p}\exp(-t/\tau_p) \tag{2.25}$$

where $p = 1, 2, \ldots$ and $q = 1, 2, \ldots$

$$\tau_p = \tau_1/p^2 \tag{2.26}$$

$$\tau_1 = \frac{\zeta_1}{k_1} = \frac{\zeta N^2 b^2}{3\pi^2 k_B T} \tag{2.27}$$

X_1 represents the motion of end-to-end size of the chain $R_N - R_1$. And X_p represents the motion of a subsection of the chain consisting of N/p beads (due to the term $\cos\left(\frac{p\pi n}{N}\right)$) with the length scale of $\sqrt{\frac{k_B T N}{k}}/p$ [30]. Those are important conclusions that will be utilized in the next section.

2.2.2:   Translocation time

At the time when the mth monomer is at the pore, the pulling force, F, is balanced by the friction force, f, on the moving segment from m^{th} monomer to m'^{th} monomer.

$$F = (m' - m) \cdot \zeta \cdot v_m \tag{2.28}$$

We assumed that each monomer in the moving segment had the same velocity as m^{th} monomer, v_m, and same friction coefficient, ζ. Also, since the pulling is strong and the movement is fast, the "active" segment adopts an almost straight line conformation, while monomers positioned far from the pore beyond m' are left unperturbed. Such a conformation can be expressed as

$$m' - m = R_{m'}/b \tag{2.29}$$

When we combine equations 2.29 and 2.28, we get the velocity of the monomer middle inside the pore

$$v_m = \frac{Fb}{\zeta R_{m'}}$$

The time it takes for the mth monomer to pass through the pore is b/v_m, which is the translocation time t_m.

$$t_m = \int_0^m \frac{b}{v_n} dn = \frac{\zeta}{F}\int_0^m R_{n'}(t_n)dn \tag{2.30}$$

20

The average translocation time is described by the following equation:

$$\bar{t}_m = \frac{\zeta}{F} \cdot [\int_0^{m'} \overline{R}_{n'} dn' - \frac{1}{2b} \overline{R}_{m'}^2]$$

(2.31)

, where $\overline{R}_n = \sqrt{R_n(t_n)^2} \approx nb^2$ is the ensemble-averaged distance of the nth monomer from the pore. Therefore, we can estimate the average translocation time scale with monomer index as

$$\bar{t}_m \approx \frac{\zeta b}{F} m^{3/2}$$

(2.32)

2.2.3:   Thermal fluctuations

Since we can determine the translocation time from the conformation of the polymer, the thermal fluctuation of the conformation, δR, will cause a fluctuation of translocation time, δt.

$$\delta t_m = \frac{\zeta}{F} \int_0^m \delta R_{n'} dn$$

(2.33)

where the relationship between n' and n follows 2.29, i.e. $n' - n = R_{n'}/b$. As the fluctuation results from random Brownian motion, only the amplitude will be of concern here.

$$\begin{aligned} \langle \delta t_m^2 \rangle &= \left(\frac{\zeta}{F}\right)^2 \int_0^m di \int_0^m dj \langle \delta R_{i'} \cdot \delta R_{j'} \rangle \\ &\simeq \left(\frac{\zeta}{F}\right)^2 \int_0^m di \int_0^m dj \langle \delta R_i \cdot \delta R_j \rangle \end{aligned}$$

(2.34)

Here we do the approximation of the fluctuation of the position of n'^{th} monomer:

$$\delta R_{n'}(t_n) = \delta R_{(n+R_{n'}/b)}(t_n) \simeq \delta R_n(t_n)$$

(2.35)

in the condition of $\delta R(n') \ll bn$.

The way to calculate the fluctuation correlation function $\langle \delta R_i \delta R_j \rangle$ is to write R_n in terms of normal coordinates, X_p, which are defined as

$$X_p \equiv \frac{1}{N} \int_0^n dn \cos\left(\frac{p\pi n}{N}\right) R_n(t)$$

with $p = 0, 1, 2, ...$

21

Then the coordinate of the nth monomer can be expanded as

$$R_n = X_0 + 2\sum_{p=1}^{\infty} X_p cos\left(\frac{p\pi n}{N}\right)$$

Applying above expansions, our correlation term equation 2.34 can be written as

$$
\begin{aligned}
\langle \delta R_i(t_i)\delta R_j(t_j)\rangle &= \int\int dpdq \langle (X_p(t_i) - X_p(0))(X_q(t_j) - X_q(0))\rangle cos\left(\frac{p\pi i}{N}\right)cos\left(\frac{p\pi j}{N}\right)\\
&= \frac{1}{2}\int dp\langle (X_p(t_i) - X_p(0))(X_p(t_j) - X_p(0))\rangle\left(cos\left(\frac{p\pi(i+j)}{N}\right) + cos\left(\frac{p\pi(i-j)}{N}\right)\right)\\
&\approx \frac{1}{2}\int dp\langle (X_p(t_i) - X_p(0))(X_p(t_j) - X_p(0))\rangle cos\left(\frac{p\pi(i-j)}{N}\right)\\
&\approx Y(|t_i - t_j|) - Y(t_i) - Y(t_j)
\end{aligned}
$$

(2.36)

where $Y(t) \equiv \int dp\left(\langle X_p(t)X_p(0)\rangle - \langle X_p(0)^2\rangle\right)cos\left(\frac{p\pi(i-j)}{N}\right)$. The third step in Eq. 2.36 assumes the fast decay of high frequency term with $cos\left(\frac{p\pi(i+j)}{N}\right)$ as p increases. In function Y, X_p corresponds to the local motion of chain segment consisting of N/p monomers with the length-scale the order of segment's ideal size $\left(\frac{Nb^2}{p}\right)^{\frac{1}{2}}$ in time-scale $\tau_p = \frac{\tau_1}{p^2}$. At time t,the fluctuation is governed by $p_t = \left(\frac{t}{\tau_1}\right)^{\left(-\frac{1}{2}\right)}$ mode.Therefore, the function Y can be estimated as:

$$
\begin{aligned}
Y(t) &\approx \frac{Nb^2}{p_t}\cdot\frac{N}{p_t}\delta_{ij}\\
&= b^2\left(\frac{N}{p_t}\right)^2\delta_{ij}\\
&= b^2 N^2\frac{t}{\tau_1}\delta_{ij}\\
&\approx \frac{k_B T\cdot t}{\zeta}\delta_{ij}
\end{aligned}
$$

(2.37)

When we plug into eq.2.34, we get $\langle \delta R_i(t_i)\delta R_j(t_j)\rangle \approx \frac{\min_{t_i t_j}}{\tau_1}(nb)^2\delta_{ij}$ which allows us to get eq.2.38

$$\langle \delta t_m^2\rangle = \int_0^m di\int_0^m dj\langle \delta R_i\cdot\delta R_j\rangle \approx mt\cdot\frac{k_B T\zeta}{F^2}$$

(2.38)

2.2.4: Conformational fluctuation

The fluctuation of the inital conformations, ΔR_n, is the position of nth monomer, R_n, away from its ensemble average $\langle R_n \rangle$. Here we assume the chain's configuration obeys the Gaussian distribution,

$$\Phi(R_n) = \left[2\pi \left(\langle R_n{}^2 \rangle - \langle R_n \rangle^2\right)\right]^{-1/2} exp \left[-\frac{(\Delta R_n)^2}{2\left(\langle R_n^2 \rangle - \langle R_n \rangle^2\right)}\right] \tag{2.39}$$

The fluctuation term in eq.2.39 is defined as $\Delta R_n \equiv R_n - \langle R_n \rangle$. The mean squared fluctuation in position is shown to have the same order of magnitude as the mean squared position:

$$\langle R_n^2 \rangle = \int \Phi(R_n)R_n^2 dR_n = 2\left(\langle R_n^2 \rangle - \langle R_n \rangle^2\right) = \langle (\Delta R_n)^2 \rangle \tag{2.40}$$

The fluctuation in translocation time due to the fluctuation in conformations can be written as:

$$\Delta t = \frac{\zeta}{F} \int_0^m \Delta R(n')dn \tag{2.41}$$

Since the polymer chain obeys the Gaussian distribution, the fluctuation of its conformation has a length-scale on order with the chain size, i.e. $\langle \Delta R_n{}^2 \rangle \approx R_n{}^2$.

$$\langle \Delta R_i \Delta R_j \rangle = \langle (\Delta R_i)^2 \rangle + \langle \Delta R_i \Delta (R_j - R_i) \rangle = \langle R_i{}^2 \rangle \approx ib^2 \tag{2.42}$$

Here we use the conclusion that $\langle \Delta R_i \Delta (R_j - R_i) \rangle = 0$, since the fluctuation of the distance from i^{th} to j^{th} monomer $(j > i)$ is uncorrelated to the fluctuation from monomer 0 to monomer i.

When we combine eq.2.42 and eq.2.41, we can obtain the conformational broadening of translocation time as:

$$\begin{aligned}
\langle \Delta t^2 \rangle &= 2\left(\frac{\zeta}{F}\right)^2 \int_0^m di \int_i^m dj \langle \Delta R_i \Delta R_j \rangle \\
&\approx \left(\frac{\zeta b}{F}\right)^2 m^3
\end{aligned} \tag{2.43}$$

Section 2.3: Simulation setup

We used and modified the software package DLPOLY V2 to conduct our simulations. In these simulations, forced translocation refers to the translocation that occurs under a driving force from the external field. For the 3D simulation, the membrane was perpendicular to the translocation direction and the nanopore was a

23

cylindrical void with length L and diameter w. The pore length was $L = 2\sigma$ and pore width was $w = 1.6\sigma$, in which σ was the size of the monomer. These dimensions were maintained throughout the simulations unless specified otherwise.

The polymer chain was represented as a string of beads connected by a spring using a coarse-grained bead-spring model. The membrane consists of fixed and regularly arranged atoms, which were considered a steric hindrance for the monomers. The monomers could not cross the membrane except through the pore. We used a bond potential connecting monomers i and j described by $U_{ij} = U_{ij}^{LJ} + U_{ij}^{ch}$, in which the first term is a trunked-shifted Lennard-Jones potential:

$$U_{ij}^{LJ} = \begin{cases} 4\epsilon_{ij}\left[\left(\frac{\sigma}{r_{ij}}\right)^{12} - \left(\frac{\sigma}{r_{ij}}\right)^{6} + \frac{1}{4}\right] & r_{ij} \leq 2^{1/6}\sigma, \\ 0 & r_{ij} \geq 2^{1/6}\sigma. \end{cases}$$

and the second term is a finite extensible nonlinear elastic bond potential:

$$U_{ij}^{ch} = -\frac{1}{2}kR_0^2 ln\left[1 - \left(\frac{r_{ij}}{R_0}\right)^2\right] \tag{2.44}$$

where $k = 30.0\epsilon/\sigma^2$ is the spring constant and $R_0 = 1.5\sigma$ is the maximum chemical bond length at which the elastic energy of the bond becomes infinite.

The motion of monomers is described by the Langevin Equation:

$$m_i \ddot{r}_i = -\nabla U_{ij} m_i \zeta \dot{r}_i + f_i(t)$$

, where U_{ij} is the interaction potential between the ith and j^{th} monomers at the bound potential(eq.2.44), and m_i, r_i and ζ_i are the mass, coordinate, and friction coefficient, respectively. All monomers were given the same mass, size, and friction coefficient. Here, $f_i(t)$ is the random force of the ith monomer, which is characterized by correlation functions

$$\langle f_{i\alpha}(t)\rangle = 0$$

$$\langle f_{i\alpha}(t)f_{j\beta}(t')\rangle = \delta_{ij}\delta_{\alpha\beta}\delta(t - t')2k_BT\zeta$$

in which α and β denote Cartesian coordinates.

Simulations were performed in the NVT ensemble with $k_BT = 1.0\epsilon$ using an integral time step $\Delta t = 0.01\tau_{LJ}$, in which $\tau_{LJ} = \sigma\left(\frac{m}{\epsilon}\right)^{1/2}$, which is the Lennard-Jones time. The simulation systems have periodic boundaries at in the directions other than x (i.e., the translocation direction). We used the reduced units and the friction coefficient was $\zeta = 4\tau_{LJ}^{-1}$. A pulling force was put on monomers inside the pore only, with a strength of $F = 8.0\frac{k_BT}{\sigma}cos\left(\frac{\pi x}{L}\right)$, where $x \in \left[-\frac{L}{2}, \frac{L}{2}\right]$ and $x = 0$ at the center of the pore. All the simulations

mentioned in this manuscript were Brownian simulation of 3D ideal chain translocations. The length of chain was 800 monomers. The thermal statistics were done by running the same initial conformation 400 times and for a total of 600 different initial conformations.

Section 2.4: Results and discussion

The section will show the dependence of the ensemble average translocation time, $\bar{t}_m$, and fluctuations of δt and Δt on both the monomer index, m, and the pulling force, F. We compared both an analytical approach and a Lagenvin dynamics simulation to study this question.

In the simulation, an ensemble of fully relaxed polymer chains are anchored at the pore on the cis side with various initial conformations, $\Gamma^1, \Gamma^2, \ldots$ For each of those conformations, Γ^i, we make identical copies in the simulations, $\Gamma^i_1, \Gamma^i_2, \ldots$. The translocation of each copy undergoes a different thermal history, and we recorded the translocation time for each monomer $t_m\left(\Gamma^i_j\right)$. The average translocation time was calculated by

$$\bar{t}_m = \frac{\Sigma_{i,j} t_m(\Gamma^i_j)}{\Sigma_{i,j}}$$

. Within the simulation, we analyzed the thermal fluctuation, δt, by taking the standard deviation of the distribution of the translocation time, i.e.,

$$\delta t_m(\Gamma^i) = \sqrt{\frac{\Sigma_j (t_m(\Gamma^i_j) - \bar{t}_m(\Gamma^i))^2}{\Sigma_j}}$$

, where $\bar{t}_m(\Gamma^i) = \frac{\Sigma_j t_m(\Gamma^i_j)}{\Sigma_j}$, and then average it over all conformations

$$\delta t_m = \frac{\Sigma_i \delta t_m(\Gamma^i)}{\Sigma_i}$$

. The fluctuation of translocation time due to the variations of initial conformations is calculated by

$$\Delta t_m = \sqrt{\frac{\Sigma_j (\bar{t}_m(\Gamma^i) - \bar{t}_m)^2}{\Sigma_i}}$$

. Details of the simulation protocol are provided in Section.2.3.

We assumed that for a given initial conformation of the polymer chain, our model could describe results of the simulations if the translocation time was much shorter than the relaxation time. Figure 2.3 compares the translocation time for two different initial conformations of the chain. Copies of the polymer chain starting from different initial conformations can be distinguished by both the analytical model and the simulation

results. The identification of conformation is referred to as fingerprinting, i.e., t_m is a fingerprint of initial conformation,

$$t_m = \frac{\zeta \cdot b}{F}(\frac{1}{b}\int_0^m R(m_1')dm_1)$$

.

In simulations, initial conformations of polymer chains are randomly distributed, so the average translocation time corresponds to an average of all possible initial conformations. In Figure 2.4, we compare how the monomer index depends on this translocation time for the model and simulations. The model predicts the average translocation time using the formula, $\bar{t}(m) \approx \frac{\zeta \cdot l_{bond}}{F}m^{1+\nu}$ (see Section.2.2.2). We conclude that predictions of average translocation time from the model agree with the simulations.

The magnitude of thermal fluctuation of the translocation time can be obtained only through Langevin Dynamics simulation and asymptotic analysis. First, we calculated the standard deviation of the translocation time for polymer chains featuring the same initial conformation within the simulation. Then the deviations were averaged over different initial conformations. We learned from the simulation that the dependence of the thermal fluctuation on the monomer index can be described as $\delta t_m \propto m^\beta$, where $\beta^{(\text{simulation})} = 1.16$. In Section.2.2.2, we found the theoretical asymptotic prediction of the thermal fluctuation of the translocation time was $\delta t_m \sim m^{0.5}t^{0.5}$ for the ideal polymer chain. If we assumed the average translocation time from the asymptotic result was $t_m \propto m^{1.50}$, then we obtained $\beta^{(\text{model})} = 1.25$, which is larger than the exponent obtained through simulation. However, if we used the average translocation time of our simulation value $\bar{t}_m \propto m^{1.36}$ instead of the asymptotic one, then the exponent of the thermal fluctuation became $\beta = 1.18$, which is quite close to the simulation value of β.

The other component of fluctuation, conformational fluctuation, Δt_m, is calculated in the simulation as the standard deviation of the thermally averaged translocation times for various initial conformations. We also calculated the translocation time as the numerical solution of translocation time under our model for each initial conformation in the absence of thermal perturbations. The scaling factor fitting from the simulation $\Delta t_m \propto m^\gamma$,$\gamma^{(\text{simulation})} = 1.5$, matched our numerical calculation based on our model $\gamma^{(\text{model})} = \frac{3}{2}$ for the ideal polymer chain (Section.2.2.2). Our results also show that the conformational fluctuation of the translocation time surpasses the thermal fluctuation as the conformational fluctuation increases faster with m (Figure 2.5).

This mismatch of scaling factors of translocation time between the model and simulation can be explained by three possible reasons. First, the model assumed rigid bonds of all polymer chains, while the bonds in the simulation will stretch if the associated monomer is pulled towards the pore. Second, the mismatch between the asymptotic results and the model could be attributed to the finite size effect of relatively short

chains. Third, our model assumed that the moving section (including $m' - m$ monomers) adopted a straight conformation. This assumption requires higher order corrections.

Section 2.5: Concluding remarks

We introduced a theoretical model to calculate the translocation time of each monomer for a given initial conformation of the polymer chain. We compared the theoretical predictions and simulation results for individual initial conformations and demonstrated that translocation time is sensitive to initial conformation of the chain, and thus can be used to fingerprint the chain conformation prior to translocation. The difference in the predicted translocation times between the model and the simulation for a single conformation was small compared to the difference between various initial conformations. Therefore, our theory can be used to characterize individual chain conformations.

The scaling dependence of the average translocation time of the mth monomer was derived using the long chain limit and characterized by the asymptotic value of the exponent $1 + \upsilon = 1.5$. Comparison of the model prediction to the simulation shows that analytical results of thermal/conformational broadening are in reasonable agreement. In addition, our model predicted the scaling law for thermal and conformational fluctuation and the correlation between initial conformation and translocation time. These predictions were also well supported by simulations.

In this work, we also investigated the ensemble average translocation time's dependence on the monomer index using both numerical calculation $t_m \propto m^{1.42}$ and simulation $t_m \propto m^{1.36}$, and compared these values with the asymptotic prediction of $t_m \propto m^{1.5}$ for the ideal polymer chain with a scaling exponent of $\nu = 0.5$. Using our model, we also studied the scaling properties of thermal fluctuation, $\delta t_m \propto m^{0.5} t^{0.5}$, and conformational broadening, $\Delta t_m \propto m^{1.5}$, which matched the simulation results within uncertainty.

There are two implications from this work. First, since the translocation time is very sensitive to initial chain conformation, in experiments the polymer can be confined in a stretched state to suppress the effect of fluctuation on translocation time. Second, the results of the monomer-index dependent dispersion of translocation time can improve the data analysis of the electric signal of the translocation events.
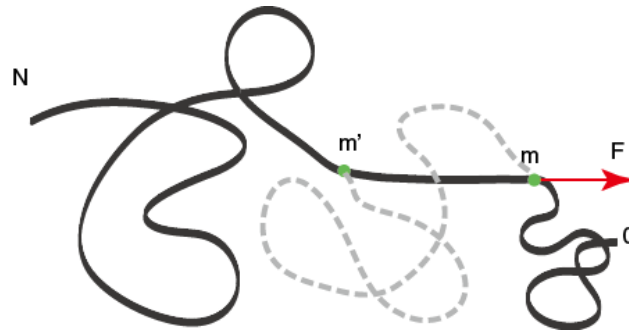
Figure 2.1: Forced translocation of the polymer through the nanopore resembles pulling a rope at a fixed location. Here m is the index of the translocating monomer (inside the pore), and $m\prime$ is the furthest monomer affected by the applied force. Only the aligned strand is subject to the pulling force (i.e., the section between the mth and $m\prime^{\text{th}}$ monomer). The dotted curve is the original conformation of the polymer chain prior to the threading motion through the nanopore.
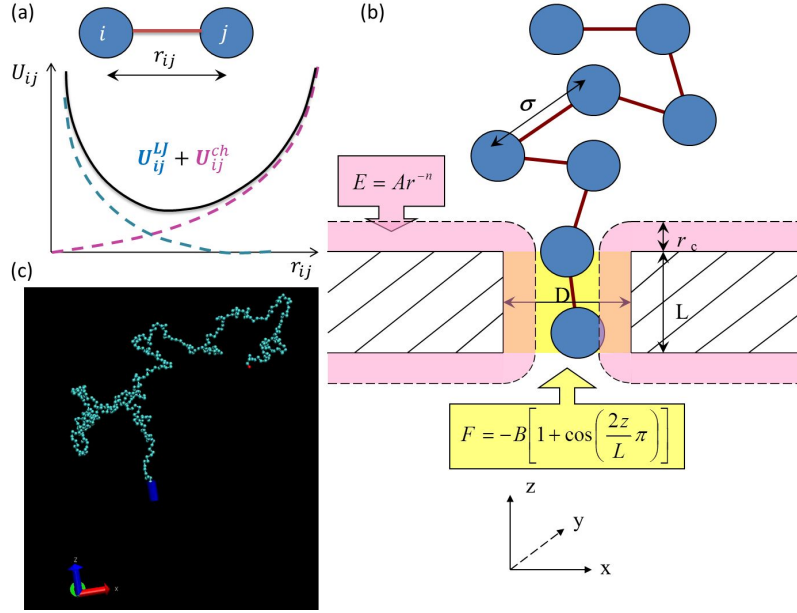
Figure 2.2: The setup of 3D Langevin Dyanmics simulation of translocation. (a) The bond potential connecting beads i and j is $U_{ij} = U_{ij}^{LJ} + U_{ij}^{ch}$, where the first term is a trunked-shifted Lenard-Jones potential and second one is a finite extensible nonlinear elastic bond potential. (b)The membrane is perpendicular to the translocation direction and the nanopore is a cylindrical void with length L and diameter w. The pore length $L = 2 \cdot \sigma$ and pore width $w = 1.6\sigma$are maintained if not specified otherwise, where σ is the size of monomer.(c) The chain is pinned at the pore before translocation.
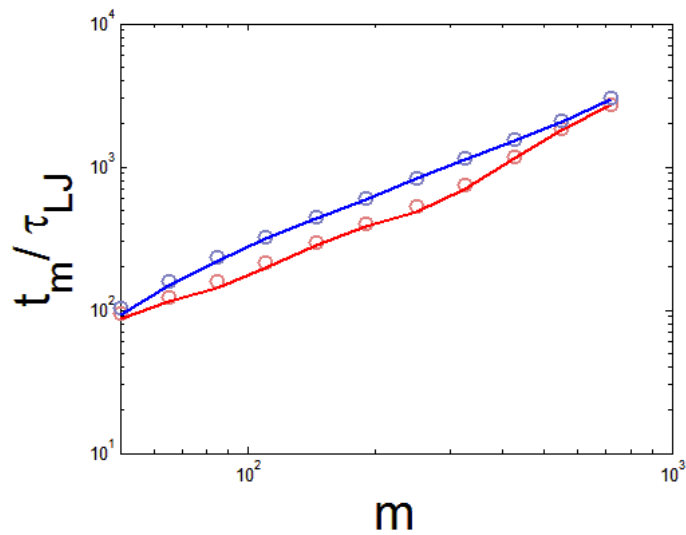
Figure 2.3: The traces of the translocation times from two chains with distinct initial conformations. Simulation results of the translocation times (circles) matched the predictions of the model(lines) for two randomly chosen initial polymer conformations. Both predictions of the thermal-averaged translocation time under the model and the simulation matched each other and were well separated for different initial conformations (blue and red). Therefore, translocation time can be considered as a fingerprint of initial polymer conformation.
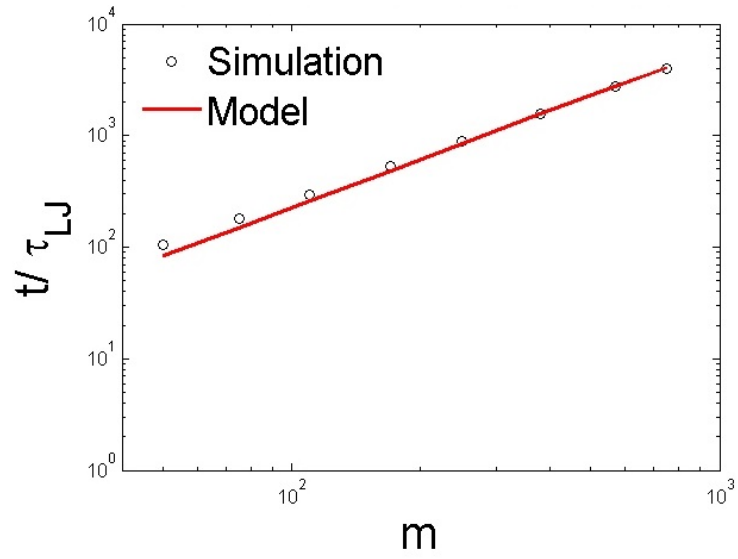
Figure 2.4: A log-log plot of average translocation time $\langle t(m) \rangle$ vs. m from the 3D simulations (circles) of the ideal polymer chain compared to our model(line). The length of the chain was $N = 800$ monomers, which passed through a nanopore of length,$L = 2.0\sigma$. Scaling exponent was fitted between m= [400,700] with uncertainty +/-0.01.
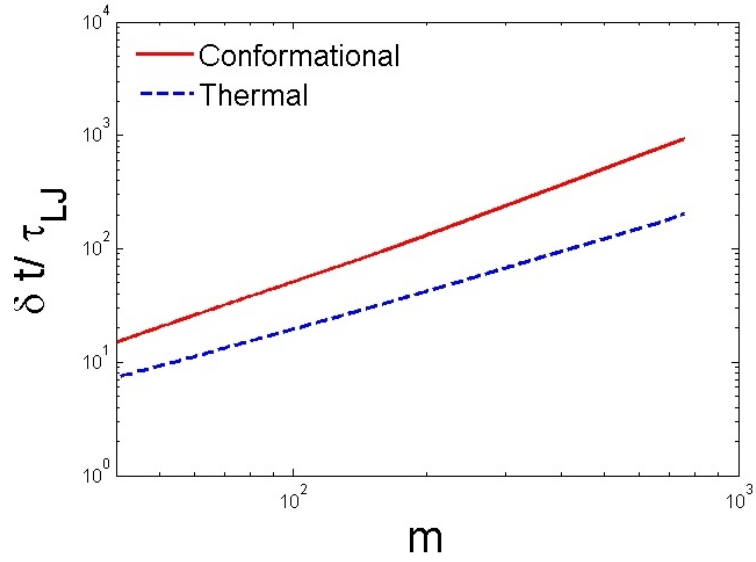
Figure 2.5: A log-log plot of the thermal broadening (dash line) and the conformational broadening (line). Scaling factor is fitted between m= [400,700] with uncertainty +/-0.01. The amplitude of thermal fluctuation is much smaller and increase slower with index than conformational fluctuation.
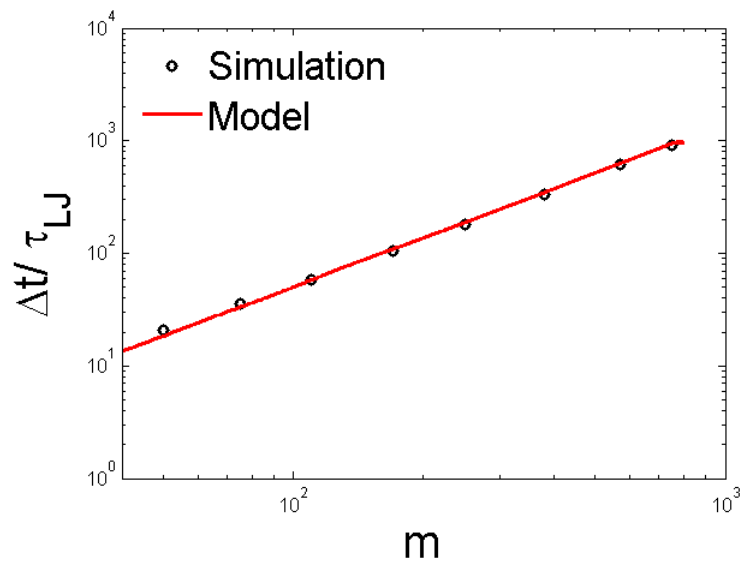
Figure 2.6: Comparing the simulation results of conformational broadening (circles) with the model's prediction (line). The scaling factor was fitted between m = [400,700] with an uncertainty of +/- 0.01.

CHAPTER 3:   Single ds-DNA molecules in nanochannels

Section 3.1:   Introduction

Like nanopores[12, 19, 110, 91, 57], nanochannels also can be utilized for the determination of genome information on a per molecule basis.[98, 59, 57, 51, 97] However, the detection technology in those two platforms can be different. In the nanopore system, a digest of electric signals can reveal either the nucleotide sequence on a scale of base pair by the depth of the blockage current or the length of a DNA molecule by the dwell times of the current blockades.[12, 57, 79] The nanochannel platform employs the optical technology to map the genomic information of single DNA molecules, instead of the electric measurements in nanopore practice[97]. The difference is due to the high electrical resistance that a long nanochannel possesses (as nanochannels are generally longer than nanopores), which makes the axial ionic conductance of the nanochannel less sensitive to the presence of DNA molecules.

When a single DNA molecule is confined to a nanochannel, it can be stretched to about half of its full length.[97] Such a linearization of the DNA provides a map from the positions of the base pairs to the genomic order of them. The enzyme cuts the DNA molecule into fragments on the sites of specific motif. The fluorescent-stained fragments relax and diffuse apart and their lengths are measured through the optical imaging. Despite of the restriction enzyme cutting[98] in nanochannels, nick-labeling[122] DNA and denaturation mapping[95] of DNA also use the optical technology for determine the relative location of the target motifs. Similar to Sangers method[104], the optical mapping within a nanochannel provides the length measurement of the fragmented DNA molecules and therefore offers the frame for assembling the genome. However, the optical mapping has the advantage of preserving the ordering of the fragments, as the fragments within the nanochannel cannot interpenetrate each other due to the excluded-volume interaction.

The assembly of genome from the digest of the lengths of the DNA fragments requires a thorough understanding of the statics of single DNA molecules confined to the nanochannel, such as the dependence of the length on the contour length and the nanochannel width. This problem will be addressed in the first part of this chapter. [1]

The entry of DNA from the reservoir into a nanochannel is driven by the high field in the nanochannel and in the immediate vicinity of the nanochannel entry.[82] The strength of the electric field decays

---

[1]This chapter is adapted from the theoretical part of a manuscript, which is contributed by Yanqian Wang, Sergey Panyukov and Michael Rubinstein.

quadratically with the distance from the nano-entrance increases, only the portion of the electric field imme-diately surrounding the entrance contributes to the nanochannel entry. Experimental and theoretical studies have found that this electric field outside nanochannel has small additional contribution to facilitate the nanochannel entry.[126, 83] Driving a micron-sized DNA molecule such as T4-phage DNA into a nano-scale channel requires a strong electric field to overcome the entropic barrier. The strong electric field results in a fast migration speed that impedes the trapping of the DNA within the nanochannel. There have been a number of experimental efforts [25, 18, 65, 123, 62] to slow down the DNA molecule: Their methods included increasing the solution viscosity, decreasing its temperature, and introducing nanochannel arrays. The un-derstanding of the driving force on the DNA is crucial in developing strategies to slow down the molecule and many efforts were made on the related research.[63, 44, 126, 35, 116] The study of this electric-induced force, i.e. the electro-hydrodynamic force will be also presented in this chapter.

Section 3.2: Physical properties of ds-DNA molecule

We model double-stranded DNA (ds-DNA) stained with an intercalating dye, as a semiflexible chain with persistence length $l_p \simeq 50nm$, backbone diameter $a \simeq 2nm$ and contour length L ($21\mu m$ for λ-DNA and $72\mu m$ for T4 DNA).[81, 93, 33] The ds-DNA backbone is negatively charged and is surrounded by positively charged counterions dissolved in a polar aqueous solvent. The bare charge of the chain backbone is two elementary charge e per basepair (bp) with the bare linear charge density $2e/bp$ ($5.9e/nm$). The counterion condensation process reduces the net charge of the backbone to the Manning value of e/l_B , where l_B is Bjerrum length, which is defined as the distance at which two elementary charges interact with electrostatic energy equal to the thermal energy k_BT , where k_B is Boltzmann constant and T is absolute temperature

$$l_B = e^2/(\epsilon k_B T) \tag{3.1}$$

The Bjerrum length is $l_B = 7\mathring{A}$ in water at room temperature with dielectric constant $\epsilon \simeq 80$. Correspond-ingly, the counterion (Onsager-Manning) condensation reduces the bare linear charge density by the factor of 4 from $2e/bp$ to $0.5e/bp = 0.14e\mathring{A}^{-1}$.

The remaining uncondensed mobile counterions are localized within double-layer "coat" around backbone with thickness equal to the Debye length. The Debye screening length depends on the concentration c_s of monovalent ions in the electrolyte solution

$$r_D = (8\pi l_B c_s)^{-1/2} \tag{3.2}$$

which is $r_d \simeq 1nm$ in a 70 mM aqueous solution of monovalent electrolyte. The effective diameter d of ds-DNA can be derived from the excluded volume interaction between two charged cylinders[113] which gives a value of $d \simeq 6nm$ for a typical 70 mM monovalent electrolyte solution. In this case, the Kuhn monomers of ds-DNA are cylindrical-like objects with length $b = 2l_p \simeq 100nm$ and diameter $d \simeq 6nm$. These Kuhn segments repel each other with excluded volume $v \approx b^2d = 6 \times 10^4 nm^3$ (approximately equal symbol means equal up to a constant factor).[77] The interaction free energy per unit volume at low concentrations can be written as virial expansion with the second virial term corresponding to 2-body repulsion

$$\frac{F_{int}}{V} = \frac{1}{2}k_BTvc^2 \tag{3.3}$$

where c is the Kuhn segment number density.

The Gaussian expression of the entropic free energy of a molecule with the root-mean-square end-to-end distance R is given by

$$F_{ent} = \frac{1}{2}k_BT\frac{R^2}{R_0^2} \tag{3.4}$$

where $R_0 \approx (bL)^{1/2}$ is the unperturbed root-mean-square end-to-end distance of the molecule. If the interaction free energy F_{int} of the molecule is less than the thermal energy k_BT, the chain conformations follow Gaussian statistics with $R_0 \approx (bL)^{1/2}$. If the interaction energy exceeds the thermal energy k_BT, the interaction energy balances the entropic contribution to the chain free energy and determines the chain size (root mean-square end-to-end distance) $R \approx (vb)^{1/5}L^{3/5}$. In such a case, a chain strand with interaction energy about k_BT is called a thermal blob. Any chain strands with size below thermal blob size $\xi_{th} \approx b^4/v$ have conformations with Gaussian statistics. Moreover, only chains with sizes larger than the thermal blob can swell. The minimal length of a swollen chain is $L_{th} \approx \xi_{th}^2/b \simeq 28\mu m$ for ds-DNA, which can be compared to the contour length $L \simeq 21\mu m$ for λ-DNA and $72\mu m$ for T4 DNA. The chain with contour length small than L_{th} will have an ideal-like conformation. The overlapping regime of such strands interpenetrating each other is called marginal solution.[106, 107] In this regime, the interactions between monomers are mean-field-like as opposed to the scaling cases of semidilute solutions.[77]

Section 3.3:   Single DNA molecules confined to a nanochannel

Consider a molecule localized inside a long narrow nanochannel with diameter D smaller than the chain size R in bulk solution. If the thermal blob size ξ_{th} is smaller than the molecule ($\xi_{th} < R$), the molecule will be extended along the nanochannel axis for moderate confinement $D < \xi_{th} < R$. This regime is known as de Gennes regime (Fig.3.1). In de Gennes regime, the conformation of the molecule can be treated as a

combination of isometric Flory blobs of size D.

If the confinement is relatively weak ($D^* < D \leq R_0$, where $D^* = b^{-5/4}v^{1/2}L^{3/4}$) and the excluded volume interaction energy of the confined molecule $F_{int} = k_B T \frac{vN^2}{R_0 D^2}$ is lower than the thermal energy $k_B T$, the molecule is not extended with longitudinal size along the nanochannel $R_{||} \approx \sqrt{Lb}$. A chain strand of size D (called confinement blob) is unperturbed and ideal-like in all directions. The chain free energy is $k_B T$ per such strand (confinement blob), $F_{ent} \approx k_B T (\frac{R_0}{D})^2$.

In narrower nanochannels with diameter $b < D \leq D^*$ (Fig.3.2a), the excluded volume interaction free energy between monomers is larger than $k_B T$ and the molecule elongates. A balance of the interaction free energy and entropic free energy $k_B T \frac{vN^2}{RD^2} \approx k_B T \frac{R^2}{b^2 N}$ determines the optimal chain elongation $R_{||} \approx L(\frac{v}{D^2 b})^{1/3}$. In this regime ($b < D \leq D^*$) the confinement free energy (Eq.3.4) is higher than the interaction free enegy. For ds-DNA in a nanochannel of diameter $D = 100nm$, which is approximately equal to the Kuhn monomer size, the length of the chain is $R_{||} \simeq 7\mu m$ for λ-DNA, while for T4 DNA, the length is $R_{||} \simeq 23\mu m$. If the nanochannel diameter $D < b$, then the chain can form hairpins in the nanochannel. For smaller nanochannel diameters ($D \ll b$), the confinement forces the molecule into a conformation of deflected strands in stead of coiled strands, known as the Odijk regime (Fig.3.1), where the bending energy increases and dominates the free energy.[86, 87, 88]

Section 3.4: Compressed DNA molecule in a nanochannel

Consider the case in which, in addition to the transverse confinement of the DNA molecule in the nanochannel of diameter $D < R_0$, the molecule is also longitudinally compressed to a size R smaller than its optimal length $R_{||}$ in an open nanochannel, i.e., $R < R_{||}$. The number density of Kuhn monomers is $c \approx \frac{N}{RD^2}$, where N is the total number of Kuhn segments per chain. The correlation length ξ is the range of the monomer pair-correlation function and is the screening length of the monomer density fluctuations. The interaction energy per strand of correlation length $1/2 k_B T v c \frac{\xi^2}{b^2}$ is on the order of $k_B T$ in marginal solvent giving $\xi \approx b/\sqrt{vc}$. The perturbation of monomer density is screened over the scale ξ. Therefore the distance from the wall over which the density increases from $c = 0$ at the repulsive wall to its average value is the correlation length ξ.

At relatively weak compression of the molecule $D < \xi$, and lower concentrations, $c < \frac{b^2}{vD^2}$, the radial density profile has a maximum in the center of the nanochannel and decays to zero at the nanochannel wall, similar to the case of the uncompressed molecule. The confinement free energy is still given by Eq.3.4 and the confinement free energy density is

$$\tilde{F}_{ent} \approx k_B T c \frac{b^2}{D^2} \qquad (3.5)$$

At higher monomer concentration $c > \frac{b^2}{vD^2}$ the correlation length $\xi < D$ and the monomer density is uniform in the central part of the nanochannel and decays to zero in the thin layer of thickness ξ near the wall (Fig.3.2b). The wall affects only conformations of chain strands on the scale ξ near the wall. Each strand of size ξ in the outer layer experiences a free energy penalty on the order of $k_B T$. Since the interaction energy of a strand of size ξ is also $k_B T$, the layer of thickness ξ near the wall has a confinement free energy on the same order as the interaction energy. Beyond this layer, there is no direct effect of the nanochannel wall on the DNA free energy, while an interaction energy of marginal solvent of $k_B T$ per correlation strand still exists.[8] The confinement energy within a correlation volume is $k_B T c \frac{\xi^3}{\xi^2/b^2}$, and the surface layer of thickness ξ occupies the fraction ξ/D of the nanochannel section volume. Therefore the confinement free energy per unit volume in this case of strong compression is $\frac{\frac{\xi}{D} k_B T c \xi^3}{(\frac{\xi^2}{b^2})\xi^3} = k_B T c^{3/2} v^{1/2} b D^{-1}$.

Combining both strong and weak compression cases we rewrite the confinement energy per unit volume within the nanochannel as

$$\tilde{F}_{conf}(D) = \begin{cases} k_B T c b^2 D^{-2} & \text{if } c < b^2/(vD^2), \\ k_B T c^{3/2} v^{1/2} b D^{-1} & \text{if } c > b^2/(vD^2) \end{cases} \qquad (3.6)$$

The higher monomer concentration implies greater overlap of chain strands. The interaction free energy per unit volume is the same as Eq.3.3 and the osmotic pressure is $\Pi \approx \frac{1}{2} k_B T v^2$.

Section 3.5:   Electrohydrodynamic force on DNA molecule in a nanochannel

Since the DNA backbone is negatively charged, the electric field exerts a force f_{el} on it. On the other hand, the positively charged ions within the Debye Layer (DL) have the same amount of charge as the backbone. Therefore electric field pulls the positive ions in the opposite direction with the force $-f_{el}$. The force on positive ions is transmitted due to the friction to the surrounding fluid, resulting in a fluid flow. The DNA backbone is dragged by the flow in the direction opposite to the direct electrostatic force f_{el} on it. The total electro-hydrodynamic force f_{eh} is the sum of both forces giving through $f_{eh} = f_{el} + f_{drag}$.

Since the flow around one strand of backbone can couple with flow around other strands, the flow profile within the molecule also depends on the conformation of the molecule. Besides the conformation, the channel where the molecule locates can put an additional restriction on the flow.

The electrohydrodynamic force is also studied for a compressed molecule in nanochannel. In order to illustrate how the boundary conditions (nanochannel or bulk solution) can change this force, we consider the molecule having the same conformation but in bulk solution. However, such conformation of DNA molecule is not physical in bulk solution. Therefore we use cross-linked microgel with mesh size ξ_H as an analog to the

compressed molecule in nanochannel. Below we discuss three special cases: i) electrophoresis of a microgel in bulk solution ii) immobile microgel in bulk solution iii) immobile microgel in a nanochannel. For each of those cases, the flow profile around microgel strand and forces acting on it will be discussed.

3.5.1:   Electrophoresis of microgel in bulk solution

The electrostatic force on the microgel pulls it and in the steady state the gel moves with velocity v. The constant velocity assumes that dragging force on the strand is equilibrated by electrostatic force

$$f_{drag} = -f_{el}$$

Thus the net force exerted on microgel is zero

$$f_e h = 0$$

The sum of all forces on the DL, including the electrostatic force on counterions $-f_{el}$ and dragging force $-f_{drag}$ from the strand, is also zero. This perfect cancellation implies that no forces act on the solvent at the boundary of the DL and the velocity of flow at that boundary at distance r_D from strand is zero. The flow profile is sketched in Fig.3.3a2 with maximum speed at the microgel strands, decreasing to zero at the distance on the order of Debye length r_D away from strands.

Due to this "local" force balance the drag force is only due to shear flow within the DL, and the resulting velocity of microgel does not depend both on fluid velocity outside of the DL and on the microgel size R.[106] The velocity is only determined by electric field and details of charge profile within the DL, $v \approx \mu E$, where μ is its electrophoretic mobility.

Due to the strong drag by the backbone, the fluid in the DL flows in opposite direction to the electric force on it.

3.5.2:   Immobile microgel in bulk solution

If the microgel is immobilized in a solution by the force, the flow direction within DL would be reversed with respect to free electrophoresis (EP) case above (see Fig 3.3b1). Within DL, the flow velocity starts from zero at the surface of stationary microgel strands and is increasing with distance away from these strands. In contrast to EP, the fluid no longer has zero velocity outside of the DL. Fluid flow is driven by counterion flow within the DL and is moving with velocity $v \approx \mu E$. In the case when there is no net flux through bulk solution, the flow through the microgel should eventually turn back forming a circulation of fluid through and

around the microgel. The backflow prefers a path with lowest hydraulic resistance to minimize dissipation. The flow with lowest resistance returns at distance from the gel on the order of its size R.

The solvent within the gel of size R moves with average velocity v and is dragged by viscous force $\eta R v$ from bulk solution. There are two additional forces acting on moving solvent in gel of size R: electrostatic force on counterions, $-f_{el}$ and the drag force from microgel backbone, $-f_{drag}$. In equilibrium, sum of these three forces has to be zero, $-\eta R v - f_{el} - f_{drag} = 0$. Therefore the dragging force with which the solvent acts on microgel backbone is $f_{drag} \approx -f_{el} - \eta R v$, where the velocity is $v = \mu E$. The resulting electro-hydrodynamic force is

$$f_{eh} = f_{drag} + f_{el} \approx -\eta R v \approx -\eta R \mu E \tag{3.7}$$

and it is equal to the stall force required to immobilize the gel $f_{stall} = -f_{eh}$.

3.5.3: Derivation of the electro-hydrodynamic force on semiflexible polyelectrolytes in nanochannels

Below we calculate the force needed to stall a semiflexible polymer with linear bare charge σ in the channel in the presence of both electric field E and electrolyte flow speed v. This force can be equilibrated by pressure difference in the channel or confinement and osmotic forces in the funnel.

We model the part of the polyelectrolyte inside the pore by a rigid cylindrical rod of radius a. Under the assumption that $b \gg a$, we approximately reduce the problem of many rods to a single rod problem by separating the space occupied by the polymer into non-overlapping cylindrical cells of radius about average distance between polymer chains ξ_H. The cylinder axis coincides with local direction of the polymer which, in general, is inclined by a certain angle θ_0 with respect to the field direction $\mathbf{E}$.

Double layer charge distribution

The electric potential and salt concentration are given by the Poisson-Nernst-Planck equations at the steady state

$$(\nabla \mathbf{J}_i (\mathbf{x})) = 0 \tag{3.8}$$

where $\mathbf{J}_i$ is the ionic flux

$$\mathbf{J}_i (\mathbf{x}) = -D_i \left[\nabla c_i (\mathbf{x}) + \frac{z_i c_i}{kT} \nabla \phi (\mathbf{x}) \right] \tag{3.9}$$

where the subscript i denotes the ion species with valence z_i, D_i and c_i are the diffusion coefficient and the concentration of the ion i, ϕ is the electric potential,

$$\varepsilon \Delta \phi (\mathbf{x}) = -\rho_e (\mathbf{x}) \tag{3.10}$$

, Δ is 2D Laplacian

$$\Delta = \frac{\partial^2}{\partial x^2} + \frac{\partial^2}{\partial y^2} \tag{3.11}$$

and ρ_e is the charge density

$$\rho_e (\mathbf{x}) = \sum_i z_i c_i (\mathbf{x}) \tag{3.12}$$

The potential $\phi (\mathbf{x})$ is determined by the Poisson-Boltzmann equation, and in Debye-Huckel approximation we find

$$\phi (\mathbf{x}) = (\mathbf{Ex}) + \phi_{Dl} (r) \tag{3.13}$$

where $\mathbf{E}$ denotes the electric field outside double layer, $r = \sqrt{x^2 + y^2}$, and the Double layer potential satisfies

$$\frac{1}{r} \frac{d}{dr} \left(r \frac{d\phi_{Dl} (r)}{dr} \right) = \phi''_{Dl} (r) + \frac{1}{r} \phi'_{Dl} (r) = \kappa^2 \phi_{Dl} (r) \tag{3.14}$$

where $\kappa = r_D^{-1} = \sqrt{2nz^2 e^2 / \varepsilon k T}$ is the inverse Debye length. The solution is

$$\phi_{Dl} (r) = \phi (a) \frac{K_0 (\kappa r)}{K_0 (\kappa a)} \tag{3.15}$$

Here K_n is the modified Bessel function of order n. Corresponding charge density forming the double layer is

$$\rho_e (r) = -\varepsilon \kappa^2 \phi_{Dl} (r) \tag{3.16}$$

Navier-Stokes equations

The motion of the electrolyte solution is coupled with the net charge density $\rho_e (r)$ via the Navier-Stokes equation

$$\eta \Delta \mathbf{v} = -\rho_e (r) \nabla \phi + \nabla p \tag{3.17}$$

with the continuity equation

$$(\nabla \mathbf{v}) = 0 \tag{3.18}$$

Here η is the dynamic viscosity of the electrolyte, p is local fluid pressure, and $\rho_e (\mathbf{x})$ is the electric charge distribution due to the co-ions and counterions. Neglecting boundary effects for long polymer, there is no dependence on the z coordinate along the polymer. In the linear approximation we get equations for three

velocity components

$$\eta \Delta v_x = -E_x \rho_e \left(r \right) + \frac{\partial p}{\partial x}, \tag{3.19}$$

$$\eta \Delta v_y = \frac{\partial p}{\partial y}, \tag{3.20}$$

$$\eta \Delta v_z = -E_z \rho_e \left(r \right) \tag{3.21}$$

where

$$E_x = E \sin \theta_0, \quad E_z = E \cos \theta_0 \tag{3.22}$$

and θ_0 is the angle between direction of external field $\mathbf{E}$ and the axis z of the polymer

The velocity $\mathbf{v}$ satisfies the continuity condition

$$\frac{\partial v_x}{\partial x} + \frac{\partial v_y}{\partial y} = 0 \tag{3.23}$$

Forces on a polymer strand

The total force per unit length of the polymer is the sum of the electric and viscous forces:

$$\mathbf{f}_{eh} = \mathbf{f}^{el} + \mathbf{f}_{drag} \tag{3.24}$$

The charge per unit length of the polymer is found by Gauss's law

$$\sigma = -2\pi a \varepsilon \phi' \left(a \right) \tag{3.25}$$

and the electric force $\mathbf{f}_{el} = \sigma \mathbf{E}$ is:

$$\mathbf{f}_{el} = \sigma \mathbf{E} \tag{3.26}$$

The drag force per unit length of polymer is given by expression

$$f_{drag}^\alpha = 2\pi a \int d\mathbf{n} \sum_\beta S_{\alpha\beta} n_\beta \tag{3.27}$$

where n_β is normal to polymer surface and the stress tensor is

$$S_{\alpha\beta} = \eta \left(\frac{\partial v_\beta}{\partial x_\alpha} + \frac{\partial v_\alpha}{\partial x_\beta} \right) - p\delta_{\alpha\beta} \tag{3.28}$$

42

Chain bending effects

The solution of the above equations is only valid on scales small with respect to the persistence length, while at larger scales the direction of the polymer randomly changes. The coordinates $\mathbf{x}' = \mathbf{R}\mathbf{x}$ and velocity $\mathbf{v}(\theta_0, \varphi_0) = \mathbf{R}\mathbf{v}$ in global coordinate system related to the channel are connected to that in local coordinate system which is rotated with polymer via the rotation matrix

$$
\mathbf{R} = \begin{pmatrix} \cos\varphi_0\cos\theta_0 & \sin\varphi_0 & -\cos\varphi_0\sin\theta_0 \\ -\sin\varphi_0\cos\theta_0 & \cos\varphi_0 & \sin\varphi_0\sin\theta_0 \\ \sin\theta_0 & 0 & \cos\theta_0 \end{pmatrix} \tag{3.29}
$$

Spherical angles $\theta_0 = \theta_0(s)$ and $\varphi_0 = \varphi_0(s)$, characterizing direction of the polymer, vary with contour length s of the polymer. At scales large with respect to persistence length of polymer they are randomly distributed in the interval $0 < \theta_0 < \pi/2$ and $0 < \varphi_0 < 2\pi$.

The force acting on the polymer is the sum of forces at all its sections and can be found by averaging the local force $\mathbf{f}_{eh}(\theta_0, \varphi_0)$:

$$
\mathbf{f} = \int_0^{2\pi} d\varphi \int_0^{\pi/2} d\theta_0 \sin\theta_0 \mathbf{f}_{eh}(\theta_0, \varphi_0) \tag{3.30}
$$

Longitudinal component of the forces

Using Eq. (3.14) we find $\phi_{Dl}(r) = \kappa^{-2}\Delta\phi_{Dl}(r)$ and Eq. (3.21) can be rewritten as

$$
\frac{1}{r}\frac{d}{dr}\left(r\frac{d\tilde{U}(r)}{dr}\right) = 0 \tag{3.31}
$$

for the function

$$
\tilde{U}(r) = v_z(r) - \frac{\varepsilon E_z}{\eta}\phi_{Dl}(r), \tag{3.32}
$$

with the solution

$$
\eta\tilde{U}(r) = C_1 + C_2\ln\frac{r}{a} \tag{3.33}
$$

From the boundary condition $v_z(a) = 0$ at $r = a$ we get the integration constant:

$$
C_1 = -\varepsilon E_z\phi_{Dl}(a) \tag{3.34}
$$

giving

$$
v_z(r) = \frac{\varepsilon E_z}{\eta}(\phi_{Dl}(r) - \phi_{Dl}(a)) + \frac{C_2}{\eta}\ln\frac{r}{a} \tag{3.35}
$$

43

The other undefined constant C_2 determines the velocity $v_z = v_z(R)$ at large scales $r = \xi_H$:

$$C_2 = \frac{\eta v_z(\xi_H) + \varepsilon E_z \phi_{Dl}(a)}{\ln(\xi_H/a)} \tag{3.36}$$

The non-zero components of the stress tensor (3.28) are

$$S_{xz} = \eta \frac{\partial v_z}{\partial x}, \qquad S_{yz} = \eta \frac{\partial v_z}{\partial y} \tag{3.37}$$

Substituting it into Eq. (3.27) and taking integral over **n** we get the contribution from the hydrodynamic drag force

$$f^z_{drag} = 2\pi a v'_z(a) \tag{3.38}$$

The bare contribution (3.26) is cancelled in the sum (3.24), and the total force per unit length comes only from partially screened hydrodynamic contribution:

$$f^z_{eh} = 2\pi \frac{\eta v_z(\xi_H) + \varepsilon E_z \phi_{Dl}(a)}{\ln(\xi_H/a)} \tag{3.39}$$

The hydrodynamic screening is only logarithmic for the straight chain.

Transversal components of the forces

The continuity condition (3.23) can be identically satisfied by the substitution

$$v_x = \frac{\partial \psi}{\partial y}, \qquad v_y = -\frac{\partial \psi}{\partial x} \tag{3.40}$$

for arbitrary stream function $\psi(x, y)$. By introducing new function

$$\Psi = \eta \Delta \psi \tag{3.41}$$

we define a system of equations for the x, y-components:

$$\frac{\partial \Psi}{\partial y} = -E_x \rho(r) + \frac{\partial p}{\partial x}, \tag{3.42}$$

$$\frac{\partial \Psi}{\partial x} = -\frac{\partial p}{\partial y} \tag{3.43}$$

44

Similarly to Eq. (3.40) the last of those equations is identically satisfied by the substitution

$$\Psi = \frac{\partial U}{\partial y}, \quad p = -\frac{\partial U}{\partial x} \tag{3.44}$$

with potential function $U(x, y)$. Substituting this Ψ to Eq. (3.42) we get

$$\Delta U = -E_x \rho(r) \tag{3.45}$$

with the solution

$$U(r) = \tilde{U}(r) + \varepsilon E_x \phi_{Dl}(r), \tag{3.46}$$

$$\tilde{U}(r) = A + B \ln(r/a) \tag{3.47}$$

where A and B are integration constants and we used Eq. (3.14) and (3.16) to present the double layer charge density in the form

$$\rho(r) = -\varepsilon \Delta \phi_{Dl} \tag{3.48}$$

Combining Eqs. (3.41) and (3.44) we get

$$\Psi = \eta \Delta \psi = \frac{\partial U}{\partial y} \tag{3.49}$$

from where we can introduce a new function u

$$\psi = \frac{\partial u}{\partial y} \tag{3.50}$$

which satisfies

$$\eta \Delta u = U \tag{3.51}$$

Using Eq. (3.14) we find

$$\phi_{Dl}(r) = \kappa^{-2} \Delta \phi_{Dl}(r) = \kappa^{-2} \left[\phi_{Dl}''(r) - \frac{1}{r} \phi_{Dl}'(r) \right] \tag{3.52}$$

and the above equation can be rewritten as

$$\eta \Delta \tilde{u} = \eta \frac{1}{r} \frac{d}{dr} \left(r \frac{d\tilde{u}(r)}{dr} \right) = \tilde{U}(r) \tag{3.53}$$

with

$$\tilde{u}(r) = u(r) - \frac{\varepsilon E_x}{\kappa^2 \eta} \phi_{Dl}(r) \tag{3.54}$$

and the solution becomes

$$\eta \tilde{u}(r) = \frac{1}{4} r^2 \left(A - B + B \ln \frac{r}{a} \right) + C \ln \frac{r}{a} \tag{3.55}$$

where C is a new integration constant.

According to Eqs. (3.40) and (3.56) the velocity distribution is related to the u as

$$v_x = \frac{\partial^2 u}{\partial y^2}, \quad v_y = -\frac{\partial^2 u}{\partial x \partial y} \tag{3.56}$$

As follows from Eq. (3.54) the velocity can be written as the sum of hydrodynamic and Double layer contributions, with the first of them:

$$\tilde{v}_x = \frac{\partial^2 \tilde{u}}{\partial y^2} = \frac{1}{\eta} \left[\frac{B}{4} \frac{y^2 - x^2}{r^2} - C \frac{y^2 - x^2}{r^4} + \frac{1}{2} \left(A + B \ln \frac{r}{a} \right) \right], \tag{3.57}$$

$$\tilde{v}_y = -\frac{\partial^2 \tilde{u}}{\partial x \partial y} = \frac{1}{\eta} \left(-\frac{B}{2} \frac{xy}{r^2} + 2C \frac{xy}{r^4} \right) \tag{3.58}$$

The Double layer contribution is

$$v_x^{Dl} = -\frac{\varepsilon E_x}{2\eta} \left[\frac{y^2 - x^2}{r^2} \left(\phi_{Dl}(r) - \frac{2}{\kappa^2 r} \phi'_{Dl}(r) \right) + \phi_{Dl}(r) \right], \tag{3.59}$$

$$v_y^{Dl} = -\frac{\varepsilon E_x}{\eta} \frac{xy}{r^2} \left(\phi_{Dl}(r) - \frac{2}{\kappa^2 r} \phi'_{Dl}(r) \right) \tag{3.60}$$

where Eq. (3.52) is applied for the derivation. From the boundary conditions $v_x(a) = v_y(a) = 0$ at $r = a$, we get relations between the integration constants:

$$\frac{B}{4} - \frac{C}{a^2} + \frac{\varepsilon E_x}{2} \left[\phi_{Dl}(a) - \frac{2}{\kappa^2 a} \phi'_{Dl}(a) \right] = 0,$$
$$A = -\varepsilon E_x \sin \theta_0 \phi_{Dl}(a) \tag{3.61}$$

where we used Eq. (3.14) ar $r = a$. The constant B determines the velocity at large scales $r \gg a$:

$$v_x \simeq \frac{1}{2\eta} \left(A + B \ln \frac{r}{a} \right), \quad v_y \simeq 0 \tag{3.62}$$

46

Using Eqs. (3.56) and (3.44), (3.51) we find components of the stress tensor (3.28)

$$S_{xx} = 2\eta \frac{\partial^3 u}{\partial x \partial y^2} - p, \quad S_{xy} = \eta \left(\frac{\partial^3 u}{\partial y^3} - \frac{\partial^3 u}{\partial x^2 \partial y} \right),$$
$$S_{yy} = -2\eta \frac{\partial^3 u}{\partial x \partial y^2} - p, \quad p = -\eta \left(\frac{\partial^3 u}{\partial x^3} - \frac{\partial^3 u}{\partial x \partial y^2} \right). \tag{3.63}$$

Substituting it into Eq. (3.27) and taking integral over $\mathbf{n}$ we get drag contribution

$$f^x_{drag} = 2\pi a \eta \left[u^{(3)}(r) + \frac{1}{r} u''(r) - \frac{1}{r^2} u'(r) \right]_{r=a} = 2\pi a U'(a) \tag{3.64}$$

$$f^y_{drag} = 0 \tag{3.65}$$

where we used relation (3.51) between functions u and U. Notice, that this equation is similar to Eq. (3.38), and similarly to the case with only the longitudinal component since the bare contribution (3.26) is cancelled in the sum (3.24). Combining the above equations we find

$$f^x_{eh} = 2\pi \frac{\eta v_x + \varepsilon E_x \phi_{Dl}(a)}{\ln(\xi_H/a)}, \quad f^y_{eh} = 0 \tag{3.66}$$

Eq. (3.39) and (3.66) can be written in vector form as

$$\mathbf{f}_{eh} = 2\pi \frac{\eta \mathbf{v} + \varepsilon \mathbf{E} \phi_{Dl}(a)}{\ln(\xi_H/a)} \tag{3.67}$$

where R is average distance between polymer chains.

We find from Eqs. (3.67) and (3.25) the reduction of the effective charge from the bare charge:

$$\frac{\sigma_{eff}}{\sigma} = \frac{1}{\kappa a} \frac{1}{\ln(\xi_H/a)} \frac{K_0(\kappa a)}{K_1(\kappa a)} \simeq \begin{cases} \dfrac{1}{\kappa a} \dfrac{1}{\ln(\xi_H/a)} & \text{at} \quad \kappa a \gg 1 \\[2ex] \dfrac{\ln[1/(\kappa a)]}{\ln(\xi_H/a)} & \text{at} \quad \kappa a \ll 1 \end{cases} \tag{3.68}$$

In the most limit $\kappa a \ll 1$ the effective charge almost do not depend on both salt and polymer concentrations.

3.5.4: A compressed DNA molecule in a nanochannel

The electrostatic potential applied along the longitudinal axis of the nanochannel creates a uniform electrostatic field inside of it. The result of this field is an electrostatic force acting in the direction opposite to the field on the negatively charged DNA molecule compressed and immobilized inside the nanochannel. There is also an electrostatic force acting on positive ions (counterions and positive salt ions) in the direction of the electrostatic field and opposite force acting on negative salt ions. Outside the Debye volume around

the DNA (and the charged walls of the nanochannel), the charge densities of positive and negative ions are the same and the net electrostatic force on fluid is zero (due to electroneutrality). Inside the Debye volume, however, there are more positive ions in the fluid, which results in the net electrostatic force acting on the fluid in the direction opposite to the field.

Within the Debye layer, the flow velocity is zero at the surface of the stationary DNA strands, and this velocity increases with distance from these strands to achieve a constant value at the boundary of the Debye layer. In the case of no net fluid flow through the solution, the fluid flow circulates through and around the molecule. Similar to Ohm's law, the path of the lowest hydrodynamic resistance determines the flux of the backflow. If the molecule is immobilized in bulk solution, the flow with lowest resistance circulates around the molecule at a distance from it on the order of molecular size R. However, the backflow for a molecule localized in a nanochannel is qualitatively different. The backflow is either primarily through the rest of the nanochannel (if its hydrodynamic resistance is lower than the resistance of the microgel) or through the molecule itself (if the molecule has a smaller hydraulic resistance than the nanochannel). In the latter case, the scale at which the flow circulates within the molecule is its "mesh size" ξ_H, defined as the average distance between two neighboring strands.

In the case of circulating fluid flow through the molecule (Fig.3.3), the flow velocity starts from zero at the polymer backbone, increases to a maximum value at the Debye length away from the backbone, and then decreases (and may even change direction) at the length scale of hydrodynamic screening length ξ_H.

$$\xi_H \approx \left[c(x)b^2\right]^{-1} \tag{3.69}$$

The flow profile in the case of strands distributed as a set of parallel rods in a very long nanochannel was studied recently.[100] We demonstrate that the force acting on a compressed molecule with randomly oriented strands separated by the average distance ξ_H in a nanochannel is similar to the force acting on a set of parallel rods separated by a distance ξ_H. The viscous drag force on the molecule is $f_{drag} \approx -f_{el} + f_{el}/\ln(\frac{\xi_H}{a})$, where a is the backbone diameter. The resulting electrohydrodynamic force is

$$f_{eh} = f_{drag} + f_{el} \approx f_{el}/\ln(\frac{\xi_H}{a}) \tag{3.70}$$

In other words, the force on the DNA molecule is reduced from the electrostatic force f_{el} by the factor of $\ln(\frac{\xi_H}{a})$ with its typical value around 5. If the surface of the nanochannel is charged, the counterions within a Debye length from the surface are driven by the electric field. This then drags the fluid in the nanochannel and creates electro-osmotic flow with flux Q. In this case, a molecule is not only pulled by the electric field

but is also driven by the electro-osmotic fluid flow in the nanochannel with non-zero flux Q. This additional contribution modifies the electrohydrodynamic force as

$$f_{eh} = (f_{el} - 2\pi\eta l Q/A)/\ln(\frac{\xi_H}{a}) \tag{3.71}$$

where η is the viscosity of the fluid, A is the cross-sectional area of the nanochannel, l is the length of the rod by analogy with the molecule strand.

This chapter focuses on the theoretical results of the free energies, conformations of single ds-DNA molecules in nanochannels as well as the forces on the molecules in presence of an electric bias. This study allows for exploration of biological interests, including the expression of genes based on chromatin conformation, mechanisms responsible for bacterial chromosome separation during cell division, packaging of long DNA strands in viral phages, etc.[96, 83] It also provides the theoretical foundation for the study of nanofunnel-confined DNA molecules in next chapter.
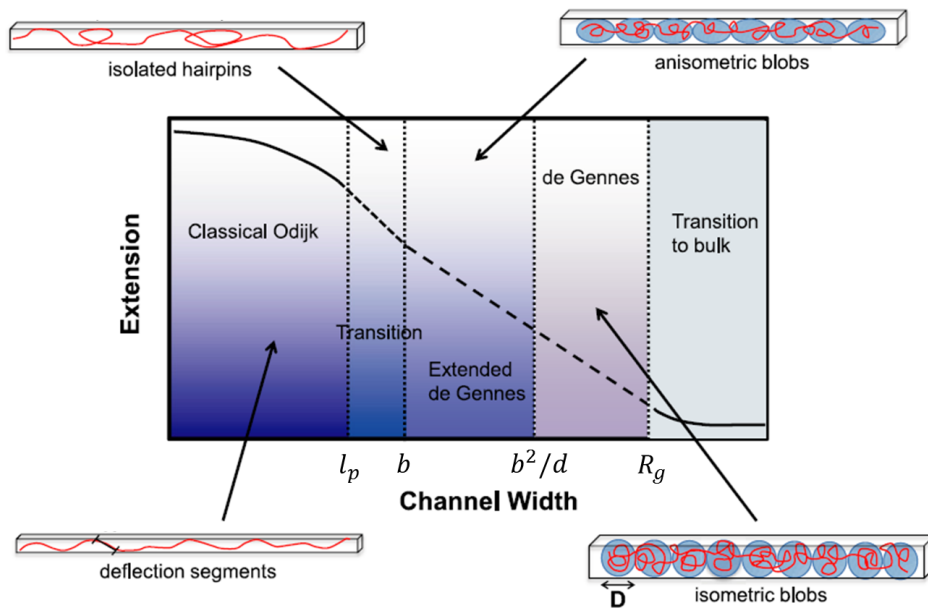
Figure 3.1: Regimes of the conformations of free semiflexible polymers in nanochannel confinement. At small channel width, the chain has a conformation of deflections with the wall. At a larger channel width, $D > b$, the polymer chain starts to coil and forms anisometric blobs and isometric blobs. Reprinted from reference[97], © IOP Publishing
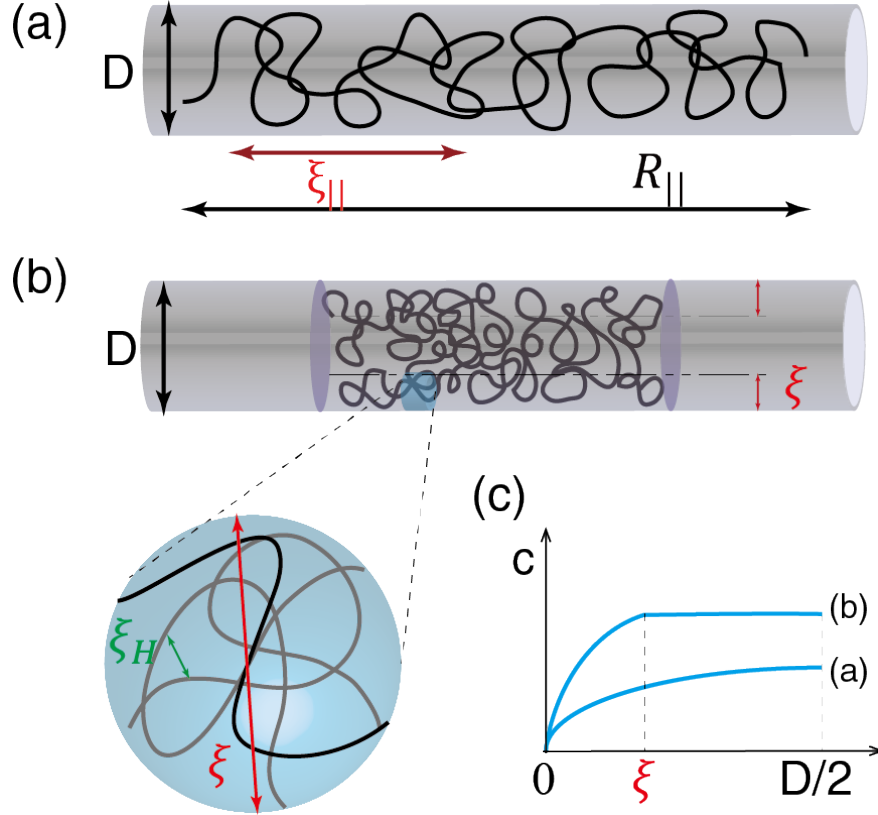
Figure 3.2: Conformation of a single molecule in a nanochannel.(a) A ds-DNA molecule confined in a long nanochannel of diameter D. It extends along the axis of the nanochannel to longitudinal size $R_{||}$. The chain strands swell on the length scale of $\xi_{||}$, within which the strand's conformation is ideal. (b) Compression in the longitudinal direction increases the monomer density c and decreases the size of the correlation length scale $\xi \propto c^{-1/2}$. On a length scale larger than correlation length ξ, the fluctuations of monomer density become uncorrelated. The hydrodynamic screening length ξ_H is smaller than correlation length ξ and is on the order of the distance between neighbouring polymer strands. At length scales larger than ξ_H, the monomers of one strand begin to couple hydrodynamically with monomers belonging to a different strand. (c) The monomer concentration c increases from its minimal value at the channel wall to a maximum concentration at the correlation length ξ away from the wall in case (b). However, the concentration in case (a) keeps increasing up to the center of the nanochannel.
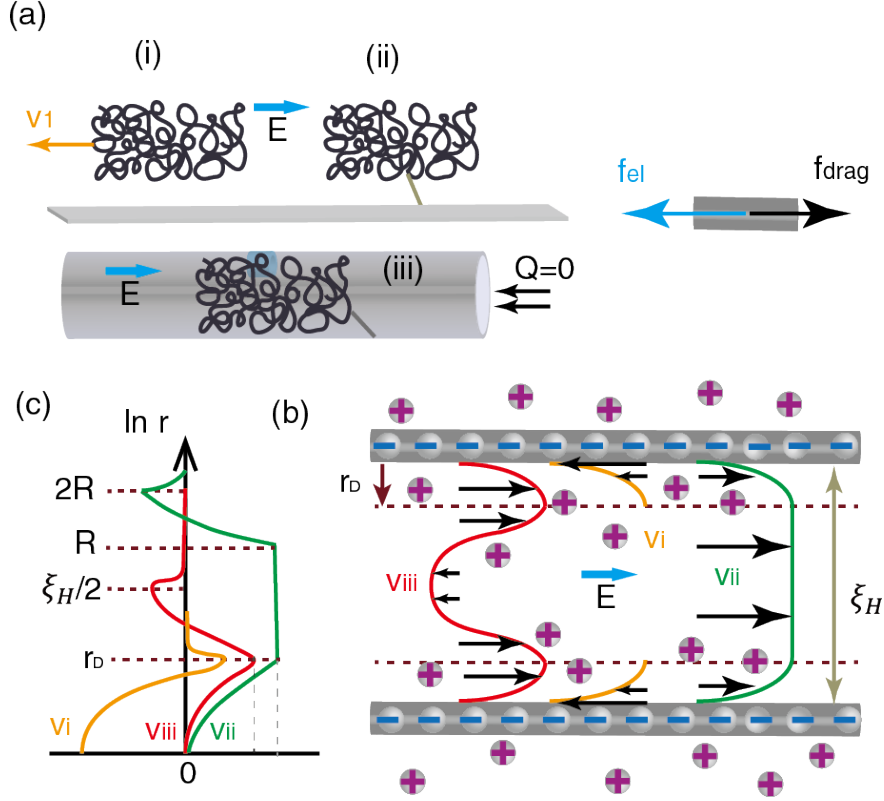
Figure 3.3: Flow profile within and around the molecules. (a) shows three cases: (i) free microgel in bulk solution (ii) stalled microgel in bulk solution (iii) stalled microgel in a long channel. The flow profile between two neighbouring stands seperated by distance ξ_H is show as v_i, v_{ii}, v_{iii} respectively. (b) The microgel in case (i) moves in a direction opposite to electric field with velocity μE, where μ is its electrophoretic mobility. The gel drags the solvent surrounding its strand. The motion of the solvent is reduced by the electrostatic force acting on positive ions primarily distributed within Debye layer r_D around polymer strands and the fluid is stationary outside of the Debye Layer. The flow around the stalled microgel in (ii) is driven by the electrostatic force on counterions and reaches its maximum speed at Debye length. The solvent within the microgel moves together and a back flow is generated immediately outside of the microgel. The backflow mostly passes through the molecule in (iii) instead of outside of the molecule in (ii) while the fluid flow within the DL would be similar to the one in (ii). (c) shows the dependence of the average flow velocity on distance away from the backbone surface.

52

CHAPTER 4: Enhanced nanochannel translocation and localization of genomic DNA molecules using three-dimensional nanofunnels

Section 4.1: Introduction

Threading a macromolecule such as DNA through a nanopore or nanochannel forces its extension and ensures the sequential passage of molecular segments through a nanoscale volume. Electrical or optical probing of this volume produces a highly localized signal that can be correlated to the structure or nucleotide sequence of the DNA.[71, 16, 89, 51, 73] The transport of DNA molecules through nanoscale conduits is most often achieved by applying an electric field across the conduit, which induces an electrostatic force on the negatively charged DNA and pulls it into the confines of the nanopore or nanochannel. The geometry of the region where critical dimensions decrease from the microscale to the nanoscale has been found to affect the dynamics of this process in nanofluidic platforms based on biological pore complexes or channels fabricated in insulating substrates.[51, 36] Control over transport dynamics in turn affects the throughput and resolving power of such platforms vis-á-vis the efficiency with which DNA molecules are introduced to the nanoscale region and the speed with which the DNA passes through the detection volume. Despite the acknowledged importance of geometry on performance, however, it is difficult to develop a detailed understanding of its role in the nanofluidic platforms thus far reported. The direct-write fabrication method of focused ion beam (FIB) milling, can be used to pattern nanofluidic structures in a substrate with control over both their width and depth. We fabricated nanochannels having three-dimensional nanofunnel entrances of various shapes, visualized DNA behavior in these nanofunnels, and modeled the observed behavior in order to better understand how controlling the geometry of the nanochannel entrance can enhance the electrokinetic manipulation of DNA molecules in nanofluidic platforms.[1]

4.1.1: Funnel shapes

Consider a nanofunnel vestibule between a nanochannel and a microchannel that has its narrow end attached to a nanochannel as shown in Fig.3. The funnel radius is assumed to have a power law dependence on the coordinate along the nanofunnel axis with exponent α characterizing the shape of the nanofunnel.

---

[1]The experimental work was accomplished by Mike J Ramsey's group. Jinsheng Zhou and Laurent D Menard performed experiments and analysed data. Yanqian Wang, Sergey Panyukov and Michael Rubinstein developed the theoretical model of nanofunnel-confined DNA molecules.

The diameter of the nanofunnel matches the nanochannel diameter D at $x = x_D$, where x_D is the coordinate of the nanochannel-nanofunnel interface. Thus the nanofunnel profile is

$$y(x) = z(x) = D(x/x_D)^{\alpha} \text{ for } x > x_D \tag{4.1}$$

where $y(x)$ and $z(x)$ are the funnel width and depth, respectively, at position x¿0 along the funnel's longitudinal axis, D is the widest dimension of the nanofunnel, and x_D is the nanofunnel length. In this study, $D = 1.5\mu m$, $x_D = 22\mu m$, the nanochannel width and depth were each 100 nm, and α values of 0, 0.45 and 0.78 were used to define the nanofunnel shapes. The cross-sectional area of the nanofunnel at coordinate x is

$$A(x) = D^2(x/x_D)^{2\alpha} \tag{4.2}$$

For an electrostatic potential applied across the nanochannel-nanofunnel device Gausss law specifies that the flux of the electric field through each cross-section of the nanofunnel is the same. Therefore the electric field E decreases with coordinate x reciprocally proportional to cross-sectional area A(x) (Eq.4.2) as

$$E(x) = E_D(x/x_D)^{-2\alpha} \tag{4.3}$$

The voltage drop across the nanofunnel is related to the electric field in the nanochannel E_D as $\Delta V = \int_{x_D}^{L_{funnel}} dx E_D (x/x_D)^{-2\alpha}$, where the nanofunnel length $L_{funnel} \gg x_D$ usually holds. For small exponents $\alpha < 1/2$, the voltage diverges with the nanofunnel length

$$\Delta V = \frac{1}{1 - 2\alpha} E_D x_D \left(\frac{L_{funnel}}{x_D}\right)^{1-2\alpha} \tag{4.4}$$

For large exponents $\alpha > 1/2$ the voltage drop is almost independent of the nanofunnel length

$$\Delta V = \frac{1}{2\alpha - 1} E_D x_D \left[1 - \left(\frac{x_D}{L_{funnel}}\right)^{2\alpha-1}\right] \simeq \frac{1}{2\alpha - 1} E_D x_D \tag{4.5}$$

while for $\alpha = 1/2$ the dependence of the voltage drop ΔV on the nanofunnel length D is logarithmic

$$\Delta V = E_D x_D \ln \left(L_{funnel}/x_D\right) \tag{4.6}$$

Although the forces on DNA molecule in a nanofunnel may differ from forces in a nanochannel, the electrohydrodynamic force has the same expression (Eq.4.3) except for the dependence of electric field $E(x)$ and cross-sectional area $A(x)$ on the nanofunnel coordinate. Compared to the zero axial forces on a molecule

confined in nanochannel, however, there are net forces directed along the nanofunnel axis due to both location dependent confinement and interaction energy. We will discuss how the geometry of the nanofunnel modifies the forces by examing the location-dependent effective free energy of the molecule.

Section 4.2:   Models

In this section we present a theoretical description of the behavior of a DNA molecule confined in a three-dimensional nanofunnel by the applied electric field. The double-stranded DNA is modeled as a semi-flexible chain having a Kuhn length, b, of 100 nm; a geometric backbone diameter, a, of 2 nm; and an effective diameter, w, of 6 nm that includes the contribution of the double layer formed by counterions around the backbone. [S3] The widths and depths of the nanochannels and nanofunnels used in this study are sufficiently large (i.e., greater than b) to allow the random coiling of the DNA molecule. The large aspect ratio b/w of the double-stranded DNA results in relatively weak excluded volume, three-body, and higher-body interactions between Kuhn segments. Solutions of polymers with such large aspect ratio Kuhn segments, called marginal solutions,[S4] are qualitatively different from ordinary polymer solutions in theta or good solvents, as will be discussed below. At a given electric field strength, the DNA molecule assumes a mean position and conformation that is determined by the local balance of the forces acting upon each of its segments. These are the confinement force, the elastic force, the electrohydrodynamic force, and the osmotic gradient force. The confinement and elastic forces are both entropic in origin and together constitute the entropic force referred to in this chapter.

4.2.1:   Confinement force

The narrower the funnel cross-section, the more contacts the DNA molecule has with the funnel walls and the greater its confinement free energy. The confinement free energy per unit volume, F_{conf}, is given by

$$F_{conf} = \begin{cases} k_B T c(x) b^2 A^{-1}(x) & \text{if } c(x) < b^2/(vA(x)) \\ k_B T c^{3/2}(x) v^{1/2} b A^{-1/2}(x) & \text{if } c > b^2/(vA(x)) \end{cases} \tag{4.7}$$

where $c(x)$ is the number density of Kuhn segments at coordinate x along the funnel axis, $A(x)$ is the cross-sectional area at coordinate x, and v is the excluded volume parameter ($v \approx b^2 w$).[106, 6] Two cases of Equation 4.7 correspond to regimes of low and high monomer density, respectively. The low monomer density regime is defined by a polymer correlation length, $\xi(x) \approx b/\sqrt{c(x)v}$, that is greater than the nanofunnel width and depth, in which case all of the DNA segments in volume $A(x)dx$ feel the effects of confinement.

The high monomer density regime occurs if the compression of the DNA molecule reduces the correlation length so that it is smaller than the nanofunnel width and depth. In this case only those DNA segments that are within a distance $\xi(x)$ from the nanofunnel walls are perturbed by the walls. DNA segments in the nanofunnel interior (located farther than $\xi(x)$ away from the nanofunnel walls) do not incur an entropic penalty. We found that, for the nanofunnels and DNA molecules investigated in this study, nearly all of the DNA segments were described by the low density regime and Equation 4.7 is used in the equations below.

The variation of the confinement free energy with the location x of the molecules segments gives rise to a confinement gradient force that pushes the molecule towards the mouth of the nanofunnel. This confinement gradient force, f_{conf}, expressed per Kuhn monomer, is the derivative of the confinement free energy density:

$$f_{conf} = -\frac{\partial}{\partial x}\left(\frac{\partial F_{conf}}{\partial c}\right) \tag{4.8}$$

The expression in the parentheses can be thought of as the contribution of the confinement to the effective monomeric chemical potential.

4.2.2: Elastic force

The conformational entropy of a macromolecule is also reduced when it is forcibly stretched by pulling on one or both ends of the molecule.[6, 17] The general expression for the elastic free energy of a randomly coiled polymer is $k_B T R^2/R_0^2$, where R is the end-to-end distance of the extended molecule and R_0 is its unperturbed end-to-end distance.[6] In the case of the nanofunnel-confined DNA molecule, we consider a segment of length dx containing $c(x)A(x)dx$ monomers. The unperturbed mean-square end-to-end distance of each such segment is $R_0^2 = b^2 c(x)A(x)dx$. The elastic free energy of the segment is $k_B T(dx)^2/[b^2 c(x)A(x)dx]$. Since the volume occupied by this segment is $A(x)dx$, the elastic free energy per unit volume, F_{elas}, can be written as

$$F_{elas} = \frac{k_B T}{[bA(x)]^2 c(x)} \tag{4.9}$$

The elastic force per Kuhn monomer is then

$$f_{elas} = -\frac{\partial}{\partial x}\left(\frac{\partial F_{elas}}{\partial c}\right) \tag{4.10}$$

where the expression in the parentheses is the elastic contribution to the effective monomeric chemical potential. This elastic contribution is particularly significant for the "transition state" conformations where the leading end of the DNA molecule is inserted into the nanochannel and is significantly stretched by the nanochannel electric field.

4.2.3: Electrohydrodynamic force

The electrostatic force acting on a Kuhn monomer of the DNA molecule is

$$f_{el} = qE(x) \tag{4.11}$$

where q is the charge per Kuhn monomer and E(x) is the electric field at coordinate x. While each nucleotide pair has a nominal charge of $2e$, counterion condensation partially shields the backbone charge, reducing the charge per Kuhn monomer to $q = eb/l_B = 143e$, where $l_B = 0.7nm$ is the Bjerrum length at which two elementary charges e interact with thermal energy k_BT.[6] Given the polarity of the applied electric field (Figure 4.1), the electrostatic force pulling on the DNA monomers is directed from the mouth to the narrow end of the nanofunnel.

The DNA backbone is further surrounded by a cloud of uncondensed counterions (cations) localized within the double layer, delimited by the Debye length, λ_D, of the solution. The electrostatic force acting on the counterions drives them from the narrow end to the wide end of the nanofunnel, in the direction opposite to the force acting on the polyanionic DNA molecule. The migrating cations transmit the electrostatic force through friction to the surrounding fluid, inducing electro-osmotic flow and resulting in a hydrodynamic drag force, f_{drag}, acting from the induced flow onto the DNA. The magnitude of f_{drag}, averaged over the cross-sectional area defined by the nanofunnel shape, depends on the fluid flow profile between DNA strands, which in turn depends on the molecular conformation of the DNA and on the presence of the nanofunnel walls. It is important to note that the DNA molecule acts as a weak electro-osmotic pump, generating a pressure difference across the molecule. Whether this pressure difference forces fluid flow towards the mouth of the nanofunnel or results in a backflow through the "pores" (paths between strands) in the DNA molecule depends on the relative hydraulic resistances of the two paths. Based on the dimensions of the micro- and nanoscale channels and the monomer density of a nanofunnel-trapped T4 DNA molecule, we estimate that the backflow through the DNA molecule has a resistance that is two orders of magnitude lower than flow towards the nanofunnel mouth. Note that in contrast to the case of a DNA molecule stalled in bulk solution, where fluid flow is circulated around the exterior of the DNA molecule, the presence of the nanofunnel walls forces the flow through the DNA molecule (Figure 4.2).[63, 31] The resulting flow profile therefore corresponds to that seen in the case of electro-osmotic flow with a counteracting pressure driven flow.[100]

If there were no force transmitted to the bulk fluid and no pressure gradient created by it, all of the force from the electric field acting on the counterions would be transmitted back to the DNA backbone by the hydrodynamic flow created by counterions migrating within the double layer. Therefore, the drag force on a stationary DNA molecule in general consists of two parts: the direct drag force,$f_{drag}^{el} = -f_{el}$, compensating

the electrostatic force and the drag force f_{drag}^{u} due to electro-osmotic flow through the pores of the molecule and the coincident backflow with combined velocity u:

$$f_{drag}(x) = -qE(x) + f_{drag}^{u}(x) \tag{4.12}$$

As noted above, the backflow observed for a DNA molecule filling the cross-section of the nanofunnel proceeds through the pores inside the entire volume of the molecule. The hydrodynamic resistance of the compressed DNA to the flow through it is analogous to the resistance of a porous medium with a pore size on the order of the mesh size, $\xi_H(x)$, which is the average distance between neighboring strands:

$$\xi_H(x) \approx [c(x)b^2]^{-1} \tag{4.13}$$

varying reciprocally with the monomer number density, $c(x)$. We note that the mesh size (also referred to as the hydrodynamic screening length) is distinct from the correlation length, $\xi(x)$, determining concentration fluctuations and osmotic pressure. $\xi_H(x)$ is a purely geometric distance between neighboring strands of double-stranded DNA and does not depend on the chain thickness or the strength of excluded volume repulsions. For the marginal solvent case, $\xi(x) > \xi_H(x)$ with the ratio $\xi(x)/\xi_H(x) = b^2 c^{(1/2)} w^{-1/2} \gg 1$.

The hydrodynamic friction force acting on chain section with size ξ_H due to flow with velocity u depends on the relative values of this mesh size and the Kuhn length b. In the case where $\xi_H \gg b$, corresponding to coil-like chain sections, the Stokes-like friction force on a section of size ξ_H is on the order of $-6\pi\eta u\xi_H$. In the opposite case where $\xi_H \ll b$ the frictional force on the rod-like chain sections is on the order of $-2\pi\eta u\xi_H/\ln(\xi_H/a)$, where $a = 2nm$ is the geometric backbone diameter. The corresponding friction force on a DNA molecule per Kuhn monomer is then $-6\pi\eta ub^2/\xi_H$ in the case of coil-like mesh segments and $-2\pi\eta ub/ln(\xi_H/a)$ for rod-like mesh segments. These two limiting cases can be combined in a cross-over expression for the drag force per Kuhn monomer

$$f_{drag}^{u} \approx -\frac{2\pi\eta ub}{\ln(\xi_H/a) + \xi_H/(3b)} \tag{4.14}$$

In general, the flow velocity through the DNA molecule can be due to an external pressure gradient, background electro-osmotic flow within the nanofunnel resulting from surface charges on the device walls, and the electro-osmotic flow induced by counterions associated with the DNA molecule plus the coincident backflow. In our experiments there is no external pressure gradient, but the negative charge of the fused silica walls of the device results in the electro-osmotic fluid flux Q through it with velocity $u_{eo}(x) = Q/A(x)$.[76]

By analogy with the electrophoretic velocity of a free-flowing molecule, the DNA counterion-induced

velocity is proportional to the product of the electric field E(x) and effective linear charge density q/b:

$$u_{bf} = -\frac{q}{b}\frac{E\lambda_D}{2\pi\eta a} \tag{4.15}$$

where λ_D is the Debye length of the solution. The total drag force per Kuhn monomer is:

$$f_{drag} = f_{drag}^{el} + f_{drag}^{v} \tag{4.16}$$

$$= -qE(x) - \frac{2\pi\eta b(u_{bf} + u_{eo})}{\ln[\xi_H(x)/a] + \xi_H(x)/(3b)}$$

$$= -qE(x) + \frac{q(\lambda_D/a)E(x) - 2\pi\eta bQ/A(x)}{\ln[\xi_H(x)/a] + \xi_H(x)/(3b)}$$

In our experiments, the mesh size ξ_H is smaller than $3b\ln[\xi_H(x)/a]$ and we therefore ignore the second term in the denominator in Equation 4.16. Combining Equations 4.12 and 4.16 gives the total electrohydrodynamic force, f_{eh}, per Kuhn monomer.

$$f_{eh} = f_{el} + f_{drag} = \frac{q_{red}(\lambda_D/a)E(x)}{\ln[\xi_H(x)/a]} \tag{4.17}$$

In Equation 4.17, we account for the electro-osmotic flow due to the surface charges on the walls of the device as a reduction in the effective charge on the DNA molecule:

$$q_{red} = q - \frac{2\pi\eta ab}{\lambda_D}\frac{Q}{EA_{nc}} \tag{4.18}$$

where E is the electric field in the nanochannel with cross-sectional area A_{nc}. This approach can be considered as an extension of the electrohydrodynamic equivalence principle formulated in Reference [63], where in the current work the backflow of solvent is through the molecule rather than around it due to the presence of the nanofunnel walls.

Electrophoresis is inherently a non-equilibrium phenomenon but the stalled DNA molecule can be approximated as having a quasi-equilibrium conformation. The impact of the electric field on the DNA conformation and its location along the funnel can then be considered as resulting from an effective potential

$$V(x) = \int^{x} \frac{(\lambda_D/a)E(x')}{\ln[\xi_H(x')/a]}dx' \tag{4.19}$$

and the effective free energy density, F_{eh}, of the electrohydrodynamic forces is

$$F_{eh} = q_{red}V(x)c(x) \tag{4.20}$$

4.2.4: Osmotic gradient force

There is also a free energy contribution from the interactions between segments of the DNA molecule, F_{int}. The interaction free energy density between the segments of a worm-like chain with high-aspect-ratio Kuhn segments can be expressed in the marginal solvent regime as a two-body repulsion term:

$$F_{int} = \frac{k_B T}{2} v c^2(x) \tag{4.21}$$

Since the concentration of DNA segments varies along the longitudinal axis of the nanofunnel (Figure 4.3), there is a gradient of the interaction free energy that induces a force pushing chain segments from high to low density regions. This force, f_{osm}, has the characteristics of an osmotic gradient force as it opposes the localized concentration of DNA monomers.

$$f_{osm} = -\frac{\partial}{\partial x}\left(\frac{\partial F_{int}}{\partial c}\right) = -k_B T v \frac{dc(x)}{dx} \tag{4.22}$$

Total effective free energy. Combining the four free energy density terms (Equations 4.7, 4.9, 4.20, 4.21) and integrating their sum over the DNA volume $\int_{x_0}^{x_N} \dots A(x)dx$ results in the expression for the total effective free energy of the molecule:

$$\frac{F}{k_B T} = P_1 \int_{x_0}^{x_N} b^2 c(x)dx + P_2 \int_{x_0}^{x_N} \frac{1}{b^2 A(x)c(x)}dx + P_3 \int_{x_0}^{x_N} \frac{v}{2}c^2(x)A(x)dx + \int_{x_0}^{x_N} \frac{qe}{k_B T}c(x)V(x)A(x)dx \tag{4.23}$$

with three numerical coefficients P_1, P_2, and P_3 of order unity and the potential $V(x)$ defined in Equation 4.19.

4.2.5: Effective free energy barrier

The effective free energy was evaluated to determine the DNA conformation at the lowest energy, F_{min}- the quasi-equilibrium conformation. Figure 4.3a shows the concentration profile for T4-phage DNA molecules in the $\alpha = 0.45$ nanofunnel at the energy minimum for two field strengths for which residence time measurements were made. As the electric field increases, it forces the molecule towards the nanochannel entrance where DNA compression by the funnel is greater and monomer concentration is therefore higher. Numerical minimization of the effective free energy in equation 4.23 provides average coordinates, $\bar{x}_0$, $\bar{x}_N$ of the leading and trailing ends and the length $L = \bar{x}_N - \bar{x}_0$ of DNA molecule, as shown in Figure 4.4a and Figure 4.5a. Equation SI.17 can also be used to determine the location and the conformation of the molecule at the effective free energy maximum, F_{max}. At this state the leading section of the DNA molecule has been

pulled into the nanochannel. Figure 4.3b shows the concentration profiles corresponding to these maximum energy conformations for the same field strengths as the quasi-equilibrium conformations in Figure 4.3a. At lower electric field strengths, the leading end of the molecule must penetrate deeper into the nanochannel to initiate successful entry of the entire DNA molecule into the nanochannel. The minimum and maximum effective free energy states of the DNA molecule described above correspond to the two balanced force conformations. For the first conformation, where the DNA molecule is wholly within the nanofunnel, the position and conformation of a trapped DNA molecule reflects the position of an effective free energy well (Fig. 4.6c). For the second conformation, the maximum effective energy corresponds to a molecule in a transition state, from which complete nanochannel entry or recoil back into the nanofunnel are equally probable.

As the molecule is displaced from this minimum position towards the nanochannel, the effective free energy increases and reaches a maximum at a position where a certain number of monomers are inserted into the nanochannel. The maximum energy conformation at a given electric field is analogous to the transition state in chemical kinetics. The difference between the maximum and minimum effective free energies, which is the effective free-energy barrier, $\Delta F = F_{max} - F_{min}$ (Fig. 4.6c). ΔF was used to calculate the mean residence time, τ, of the molecule in the nanofunnel.

4.2.6: Thermal fluctuations

The experimentally measured thermal fluctuations, σ_{x_0} and σ_{x_N}, and their correlation, ρ, can be evaluated theoretically by analyzing the effective free energy surface near its minimum. The effective free energy difference with respect to this minimum is the minimal work, R_{min}, performed to displace the molecule from its quasi-equilibrium state, which can be calculated as the sum of the work R_i done on each Kuhn monomer:

$$R_{\mathrm{min}} = \sum_{i=0}^{N} R_i \tag{4.24}$$

If the i-th monomer is displaced from its quasi-equilibrium position x_i by a small value δx, the restoring force on this monomer linearly depends on the displacement, $f(x_i + \delta x) \sim \delta x$. The work performed upon shifting the monomer by a small displacement δx_i is

$$R_i = -\int_{x_i}^{x_i + u_i} f_i(x)dx \simeq \frac{1}{2} f_i(x_i + \delta x_i)\delta x_i \tag{4.25}$$

For given displacements of chain ends, δx_0 and δx_N, we approximate the monomer displacement $\delta x_0 =$

61

$\delta x(x_i)$ by a linear function $\delta x(x)$ of the monomer position $x = x_i$ in the undeformed state:

$$\delta x(x) = \delta x_0 + \frac{x - x_0}{x_N - x_0}(\delta x_N - \delta x_0) = \delta x_0 + (x - x_0)\frac{\delta L}{L} \tag{4.26}$$

Here $\delta L = \delta x_N - \delta x_0$ is the variation of the molecule's extension along the funnel axis from the equilibrium value $L = x_N - x_0$. Combining Equations 4.24 and 4.25 and approximating the sum over i by integration over the number of monomers $dN(x)$ in the layer of thickness dx,

$$dN(x) = c(x)A(x)dx \tag{4.27}$$

we obtain

$$R_{min} = -\frac{1}{2}\sum_{i=0}^{N} f_i(x_i + \delta x_i)\delta x_i \simeq -\frac{1}{2}\int_{x=x_0}^{x=x_N} f(x + \delta x(x))\delta x(x)dN(x) \tag{4.28}$$

We calculate the concentration, $c'(x')$, of a displaced DNA molecule, by considering the number of monomers, $dN(x)$, that was displaced from a chain segment with length dx in the quasi-equilibrium conformation to a segment with the same number of monomers $dN(x)$ in the higher effective free energy conformation with length dx':

$$dN(x) = c'(x')A(x')dx' = c(x)A(x)dx \tag{4.29}$$

We further obtain:

$$(c(x) + \delta c(x))(A(x) + \delta A(x))(L + \delta L) = c(x)A(x)L \tag{4.30}$$

where $\delta c(x) = c'(x') - c(x)$ is the density variation produced by the displacement δx. The solution of Equation 4.30 for $\delta c(x)$, evaluated up to the second order in δA and δL is

$$\delta c(x) \simeq c(x)\left[-\frac{\delta A(x)}{A(x)} - \frac{\delta L}{L} + \left(\frac{\delta A(x)}{A(x)}\right)^2 + \left(\frac{\delta L}{L}\right)^2 + \frac{\delta A}{A}\frac{\delta L}{L}\right] \tag{4.31}$$

Given the relationship between $A(x)$ and x we find that

$$\frac{\delta A(x)}{A(x)} \simeq 2\alpha\frac{u}{x} \tag{4.32}$$

The segments of a stably trapped DNA molecule are typically wholly inside the funnel (they do not penetrate into the nanochannel) and the contribution of entropic elasticity (f_{el}) is much smaller than that of confinement (f_{conf}) and is excluded from our consideration. In the quasi-equilibrium state, the confinement

and osmotic forces acting on the monomers are:

$$f_{conf} = P_1 k_B T \frac{c(x)b^2}{A^2(x)} \frac{\partial A(x)}{\partial x} \tag{4.33}$$

$$f_{osm} = -P_3 k_B T v \frac{dc}{dx} \tag{4.34}$$

and the electrohydrodynamic force, f_{eh}, is defined in Eq. 4.16. Below we calculate these forces for a DNA molecule with ends displaced by δx_0 and δx_N from their average positions:

$$f_{conf}(x + \delta x(x)) = [1 - 2\frac{\delta A(x)}{A(x)}]f_{conf} \tag{4.35}$$

$$f_{osm}(x + \delta x(x)) = -P_3 k_B T v \frac{d(c(x) + \delta c(x))}{(1 + \delta L/L)dx} \tag{4.36}$$

$$f_{eh}(x + \delta x(x)) = \left[1 - \frac{\delta A(x)}{A(x)} + \frac{\delta c(x)}{c(x) \ln(\xi_H(x)/a)}\right] f_{eh} \tag{4.37}$$

Using the condition of quasi-equilibrium,

$$f_{conf}(x) = f_{osm}(x) - f_{eh}(x) \tag{4.38}$$

one can exclude the confinement force $f_{conf}(x)$ from Eq.4.35

$$f_{conf}(x + \delta x(x)) = -[1 - 2\frac{\delta A(x)}{A(x)}][f_{osm}(x) + f_{eh}(x)] \tag{4.39}$$

Combining Equations 4.25-4.39 we find the minimal work in the case of a funnel with $\alpha=0.5$:

$$\frac{R_{\min}}{k_B T} = \frac{1}{2} \int_{x_0}^{x_N} \left[(\frac{\delta x(x)}{x} - \frac{\delta L}{L \ln(\xi_H(x)/a)}) \delta x(x)(-f_{eh}(x)) - 2\frac{\delta x(x)}{x} \delta x(x) f_{osm}(x) \right] c(x)A(x)dx$$
$$+ P_3 \frac{v}{2} \int_{x_0}^{x_N} \left[(\frac{\delta x(x)}{x})^2 + \frac{\delta x(x)}{x} \frac{\delta L}{L} + (\frac{\delta L}{L})^2 \right] c^2(x)A(x)dx \tag{4.40}$$

where upon substituting in the equations for f_{eh} and f_{osm} we obtain

$$\frac{R_{\min}}{k_B T} \simeq \frac{1}{2} \int_{x_0}^{x_N} \left(\frac{\delta x(x)}{x} - \frac{\delta L}{L \ln(\xi_H(x)/a)} \right) \frac{\delta x(x)}{x} \frac{q_{red} E_D x_D}{k_B T \ln(\xi_H(x)/a)} c(x)A(x)dx$$
$$+ P_3 \frac{v}{2} \int_{x_0}^{x_N} \left[\left(\frac{\delta x(x)}{x} \right)^2 - \frac{\delta x(x)}{x} \frac{\delta L}{L} + \left(\frac{\delta L}{L} \right)^2 \right] c(x)^2 A(x)dx \tag{4.41}$$

Note that only adjustable coefficient P_3 enters equation SI.35 explicitly, while coefficient P_1 enters this

minimum work implicitly through the equilibrium concentration profile c(x). Coefficient P_2 is omitted from the analysis of stably trapped DNA molecules as f_{el} is negligible in this case as noted above (P_2 does enter into the analysis of nanofunnel residence times, Figure 4.7a. Substituting Eq. 4.28 and collecting similar terms in powers of δx_0 and δL we get

$$\frac{R_{\min}}{kT} = A\left(\frac{\delta x_0}{x_0}\right)^2 + B\frac{\delta x_0}{x_0}\frac{\delta L}{L} + C\left(\frac{\delta L}{L}\right)^2 \tag{4.42}$$

where coefficients A,B, and C are

$$A = \frac{D^2 x_0^2}{2x_D}\left[P_3 v \int_{x_0}^{x_N}\frac{c^2(x)}{x}dx + \int_{x_0}^{x_N}\frac{q_{red}Ex_D}{k_BTx\ln\left(\xi_H(x)/a\right)}c(x)dx\right] \tag{4.43}$$

$$
\begin{aligned}
B = \frac{D^2 x_0 L}{2x_D}&\left[2P_3 v \int_{x_0}^{x_N}\frac{(x - x_0)c^2(x)}{x}dx - P_3 v\int_{x_0}^{x_N}c^2(x)dx\right.\\
&\left.+2\int_{x_0}^{x_N}\frac{q_{red}Ex_D}{k_BTx\ln(\xi_H(x)/a)}(x - x_0)c(x)dx\right]
\end{aligned}
\tag{4.44}
$$

$$
\begin{aligned}
C = \frac{D^2}{2x_D}&\left[P_3 v \int_{x_0}^{x_N}\frac{(x - x_0)\,c^2(x)}{x}dx + P_3 v\int_{x_0}^{x_N}c^2(x)x_0 dx\right.\\
&\left.+\int_{x_0}^{x_N}\frac{q_{red}Ex_D(x - x_0)^2}{k_BTx\ln\left(\xi_H(x)/a\right)}c(x)dx - \int_{x_0}^{x_N}\frac{q_{red}Ex_D(x - x_0)}{k_BT\ln^2\left(\xi_H(x)/a\right)}c(x)dx\right]
\end{aligned}
\tag{4.45}
$$

The probability, $P(\delta x_0, \delta x_N)$, of a DNA conformation where the respective ends have deviated by distances $\delta x_0, \delta x_N$ is

$$P(\delta x_0, \delta x_N) = \frac{1}{2\pi\sigma_{x_0}\sigma_{x_N}}\exp\left[-\frac{z}{2(1 - \rho^2)}\right] \tag{4.46}$$

and z is defined as

$$z = \frac{(\delta x_0)^2}{\sigma_{x_0}^2} - \frac{2\rho\delta x_0\delta x_N}{\sigma_{x_0}\sigma_{x_N}} + \frac{(\delta x_N)^2}{\sigma_{x_N}^2}$$

where

$$\sigma_{x_0} = \frac{x_0}{\sqrt{A - B^2/C}} \tag{4.47}$$

$$\sigma_{x_N} = \frac{x_N}{\sqrt{C - B^2/A}} \tag{4.48}$$

and

$$\rho = -B/\sqrt{AC} \tag{4.49}$$

Figure 4.3 shows the probability distributions calculated with the above method for two representative trapping field strengths, and its comparison with corresponding experimental results. There is good agreement between the theoretical and experimental distributions despite the approximations in the calculations above. The calculations assume a harmonic quasi free energy well centered on the lowest energy conformation and position. Equations 4.36-4.45 also consider a nanofunnel with $\alpha=0.5$ to keep the algebra more tractable (experimental measurements were made in a nanofunnel with $\alpha=0.45$).

Section 4.3:   Results

4.3.1:   Comparison of theoretical and experimental values

The theoretical predictions were fit to the experimental data by adjusting the relative contributions of the electrohydrodynamic, entropic, and osmotic gradient forces using a weighted least squares method. This was realized in practice by multiplying each of the electrohydrodynamic, entropic, and osmotic gradient contributions to the effective free energy calculated from first principles by a coefficient of order unity, resulting in three fitting parameters. These three fitting parameters were determined by simultaneously optimizing across the various λ-phage and T4-phage data sets: (1) the residence time measurements of the various nanofunnels and (2) the mean position and extension length measurements and (3) fluctuation measurements in the $\alpha = 0.45$ nanofunnel. That is, the fit was performed across eighteen independent data sets. Each data point was weighted by the reciprocal of its variance and the sum of squared residuals was minimized using the steepest descent algorithm. Determining the values of the fitting parameters P_1, P_2, and P_3 in Equations 4.23 and 4.39-4.45 above that yielded the optimal fit of theoretical predictions to experimental values was achieved using a weighted least squares method. The independent data sets that were included in the analysis were the residence times of λ-phage and T4-phage DNA molecules in the absence of a nanofunnel and in the $\alpha=0$, $\alpha=0.45$, and $\alpha=0.78$ nanofunnels (8 data sets, Fig 4.7 a); the electric field dependent average positions, x_0 and x_N, of λ-phage and T4-phage DNA molecules in the $\alpha=0.45$ nanofunnel (4 data sets, Fig.4.4a and Fig. 4.5a); and the electric field-dependent fluctuations, σ_{x_0} and σ_{x_N}, and their correlation, ρ, of λ-phage and T4-phage DNA molecules in the $\alpha=0.45$ nanofunnel (6 data sets, Fig. 4.4d and Fig.4.5d). The optimal values of the fitting parameters were found to be $P_1 = 2.3, P_2 = 1.1$, and $P_3 = 1.4$.

4.3.2: Lowering threshold electric field using nanofunnels

In the absence of a nanofunnel (Fig.4.1a), the high electric field in the nanochannel acts only on those nucleotides closest to the entrance, which in turn pull the entire DNA molecule into the nanochannel if the force is sufficient to overcome the opposing entropic force.[68, 86, 109] Although the frequency of DNA threading can be increased by applying a larger voltage, this approach is problematic if the resulting DNA transport velocity exceeds the sampling rates of electronic or optical detection modes.[117, 14, 99, 25, 18, 47, 24] By incorporating a three-dimensional nanofunnel with the appropriate geometry at the nanochannel entrance (Fig. 4.1b), DNA can be more efficiently introduced to the nanochannel without an increase in the nanochannel electric field. The nanofunnel can be shaped such that at its mouth the electrohydrodynamic (coupled electrostatic and hydrodynamic) force gradient is greater than the entropic force gradient and DNA entry into the nanofunnel is unimpeded. As the net force acting on the DNA molecule within the nanofunnel drives it towards the nanochannel entrance, the increasing confinement partially extends the DNA molecule, reducing its conformational entropy. The forces in the nanofunnel have thus done some work on the DNA molecule and the molecule is in a conformation that can more easily enter the nanochannel than in the case without a nanofunnel. The presence of the nanofunnel furthermore generates an additional force acting on the entire DNA molecule and pushing it into the nanochannel entrance, an osmotic gradient force that arises from variation in the DNA monomer concentration along the longitudinal axis of the nanofunnel. Our theoretical model shows, and experimental measurements confirm, that the forces experienced by the DNA molecule in the nanofunnel result in compression of the DNA leading sections towards the nanochannel entrance by DNA trailing sections, an effect that we refer to as an electro-osmotic piston.

We imaged individual fluorescently stained DNA molecules as they were electrokinetically driven towards a nanochannel through a three-dimensional nanofunnel having a square cross-sectional profile that decreased gradually in both width and depth from 1500 to 100 nm (Fig.4.6a).[102] When the electric field was sufficiently high, a molecule would immediately enter the nanochannel upon reaching the nanofunnel-nanochannel junction (Fig. 4.6b, red line i). At intermediate electric fields, a molecule would reside for a time, τ, at the nanochannel entrance, repeatedly attempting to overcome the free-energy barrier before successfully entering (Fig.4.6b, blue line ii, $\tau = 47$ s). At low electric fields, the residence time increased so that a DNA molecule was in effect sustainably trapped within the nanofunnel (Fig. 4.6b, green line iii). The low and intermediate field behaviors were modeled by balancing the confinement, electrohydrodynamic, and osmotic gradient forces acting on each of the sections of a DNA molecule. The positional dependence of these forces can be represented by an effective free-energy profile of the DNA molecule (Fig. 4.6c) with the difference between the energy minimum and maximum corresponding to the effective free-energy barrier

(ΔF) to nanochannel entry. Increasing the electric field reduces the barrier height, decreasing the residence time according to the Arrhenius relation:

$$\tau \sim \tau_0 \exp(\Delta F/k_B T) \tag{4.50}$$

where τ_0 is the minimum time needed for the molecule's leading sections to diffusively enter the nanochannel,[96, 97]. At electric field strengths where ΔF is sufficiently greater than $k_B T$, the free-energy minimum corresponds to the trapping position of the DNA molecule located some distance from the nanochannel entrance (Fig. 4.6c, green line iii). The field-dependent residence times were measured in three funnels with comparable dimensions but different shapes, as well as for DNA entry into a nanochannel without an incorporated nanofunnel. Measurements were carried out using DNA molecules of two different lengths λ-phage and T4-phage genomic DNA, having stained contour lengths of 21 and 72 μm, respectively. Expected residence times were also calculated theoretically by determining the molecular conformations corresponding to the minimum and maximum effective free-energy at each nanochannel electric field strength and then calculating ΔF and therefore τ. We found that in each device with a nanofunnel, the longer T4-phage DNA molecules entered the nanochannel more readily than λ-phage DNA molecules (Fig. 3a). This effect is due to the increased size of the molecule's trailing portion that contributes to a stronger electro-osmotic piston effect. DNA entry into the nanochannel was easiest in funnels with larger α values. The high electric field of the nanochannel extends farther into the nanofunnel as does the region of greater confinement. The increased gradients of the opposing electrohydrodynamic and entropic forces therefore result in greater compression and a greater osmotic gradient force. We used the nanochannel electric field E_0 at which $\Delta F = 0$ to compare the effectiveness of various nanofunnels (Fig.4.7b). Since this is the field strength at which $\tau = \tau_0$, values for E_0 can be estimated by extrapolating the experimental data to short residence times. The greater than 30-fold reduction in E_0 that is observed experimentally is in close agreement to the reduction predicted theoretically by direct calculation of the electric field at which $\Delta F = 0$ (Fig. 4.7b).

4.3.3:   Trapping of DNA using electro-osmotic tweezers

The controlled trapping of both λ-phage and T4-phage DNA were experimentally investigated and theoretically modeled. Figure 4.5 shows the results for a T4-phage DNA molecule trapped in a α=0.45 nanofunnel at various electric field strengths. In Figure 4.5a, the evidence of DNA compression is more noticeable than in the case of the smaller λ-phage DNA molecule (Figure 4.4a). As the molecule moves from the nanofunnel mouth to the nanochannel entrance with increasing field strength, its extension length, L, first increases slightly as a result of the increased confinement but then is almost constant across a range of electric field

strengths and even decreases slightly, despite experiencing a continued increase in confinement.[96] Representative results are shown in Figures 4.5b and 4.5c for the relative probability of various combinations of end coordinates, x_0, x_N, at nanochannel electric fields of 8 V/cm and 21 V/cm, respectively. The values of σ_{x_0}, σ_{x_N}, and ρ determined from such distributions are compared in Figure 4.5d to the theoretical predictions of T4-phage DNA's thermal fluctuations. Not surprisingly, the correlation, ρ, between the fluctuation of the leading and trailing ends is lower for the T4-phage DNA molecule than for the case of the smaller λ-phage DNA molecule. As was the case for a λ-phage DNA molecule, the fluctuations of the leading end, σ_{x_0}, decrease more strongly with increasing electric field than the fluctuations of the trailing end, σ_{x_N}. This effect is more dramatic in the case of T4-phage DNA and is indicative of a greater difference between the monomer concentration at the leading and trailing segments in the longer molecule.

Within each of the three nanofunnels, the electric field strength could be reduced to achieve stable trapping of a DNA molecule for minutes or even hours. Such trapping was systematically measured in the α = 0.45 nanofunnel by imaging a single DNA molecule at several trapping field strengths. The mean position of the trapped molecule is sensitive to the strength of the applied electric field and we refer to nanofunnels operated in this mode as "electro-osmotic tweezers" by analogy to optical or magnetic tweezers. Figure 4.4a compares the experimental mean positions of the leading end (x_0) and trailing end (x_N) of a λ-phage DNA molecule trapped over a range of field strengths to the respective values predicted by theory. As the molecule moves from the nanofunnel mouth to the nanochannel entrance with increasing field strength, its extension length $(L = (\bar{x}_N - \bar{x}_0)$ increases. The electro-osmotic compression makes this observed increase less dramatic than predicted in the absence of an electric field.[96]

In addition to tuning the trapping position, varying the applied electric field of the electro-osmotic tweezers also affects the stiffness of the trap and therefore the magnitude of DNA thermal fluctuations. Measured values of various combinations of end coordinates x_0, x_N for a DNA molecule trapped at the representative nanochannel electric fields of 12.7 V/cm and 22 V/cm are shown in Figures 4.4b and 4.4c, respectively. Such data were fit to bivariate normal distributions (red ellipses in Fig. 4.4b,c) to determine the fluctuations of the end positions $(\sigma_{x_0}$, $\sigma_{x_N})$ and their correlation (ρ). The experimental results were compared to values determined theoretically by calculating the minimal work necessary to displace the molecule's ends from their mean positions (Fig. 4.4d). At the lowest field strengths the molecule is weakly trapped and thermal fluctuations are larger and highly correlated as the molecule fluctuates as a whole along the longitudinal nanofunnel axis. At higher electric fields, the correlations between fluctuations of the ends are reduced as compression of the leading sections of the molecule suppresses the fluctuations of this end, while the less constrained trailing end of the molecule is freer to fluctuate.

In summary, the force gradients experienced by a DNA molecule as it is electrokinetically driven from a

microscale reservoir into a nanochannel are highly dependent on the geometry at the nanochannel entrance that defines how abruptly or gradually a DNA molecule experiences increased confinement. Through a combination of experimental and theoretical results, we demonstrated that nanofunnels where $\alpha \simeq 1.5$ were most effective at lowering the field strength needed to drive DNA transport through a nanochannel. Nanofunnels defined by smaller values were more useful for trapping DNA molecules at voltage-dependent positions within the nanofunnel. We expect that the theoretical model of DNA behavior described here will guide future refinements in structures that can provide enhanced transport control in nanofluidic-based nucleic acid and protein analysis platforms.[128]
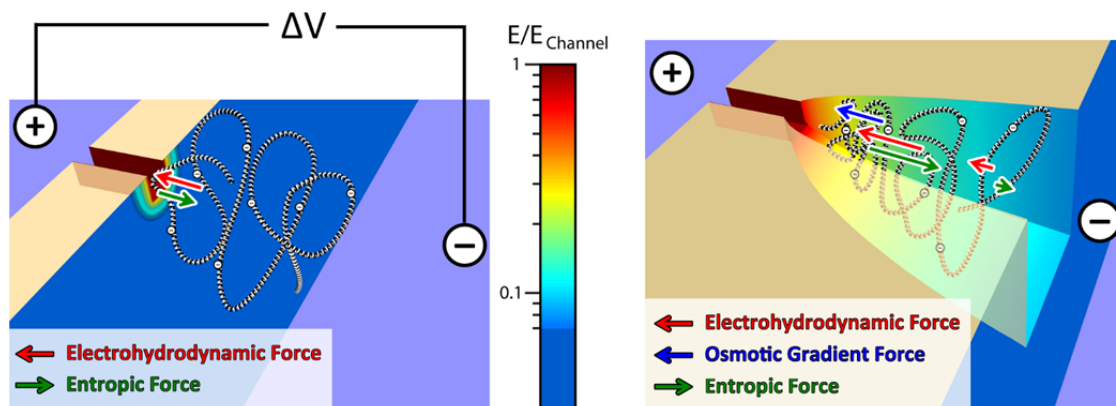
Section 4.4:   Figures

Figure 4.1:   Comparison of DNA threading into a nanochannel directly or through a three-dimensional nanofunnel. a, Cartoon illustrating the electrohydrodynamic (red arrow) and entropic (green arrow) forces affecting the leading portion of the DNA molecule as it is electrophoretically pulled into a nanochannel. b, These forces and an additional osmotic gradient force (blue arrows) act on a larger portion of the DNA molecule than in (a) due to the extended high electric field region and the confining effects of the nanofunnel. The osmotic gradient force acts as an "electro-osmotic piston," providing further assistance for DNA entry into the nanochannel. The relative electric field strengths are shown by different colors using a logarithmic scale for clarity.
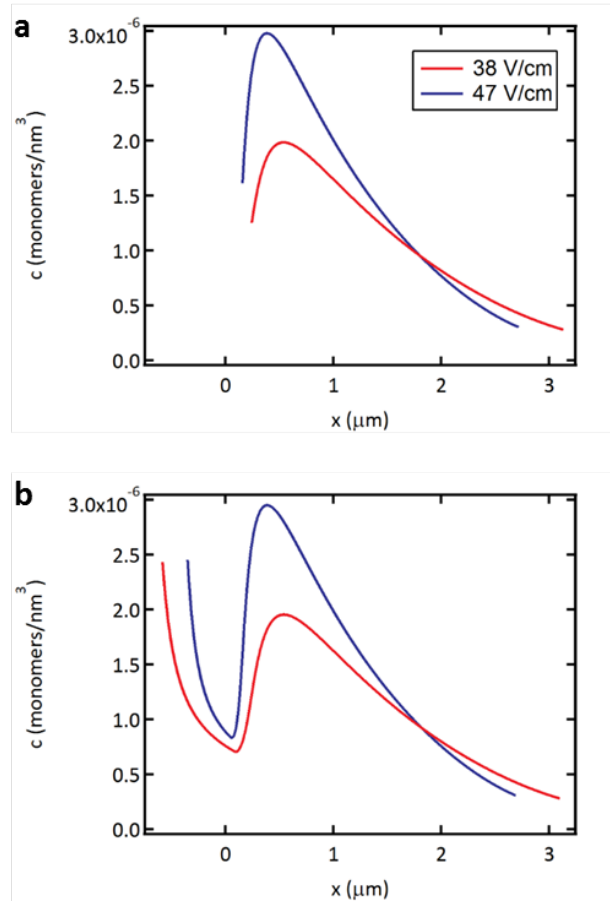
Figure 4.2: — Concentration profiles for T4-phage DNA in the $\alpha = 0.45$ nanofunnel at two field strengths. a,b, Profiles corresponding to the quasi-equilibrium conformation and highest energy ("transition state") conformation, respectively. These field strengths coincide with those used in the residence time measurements summarized in Figure 4.7.
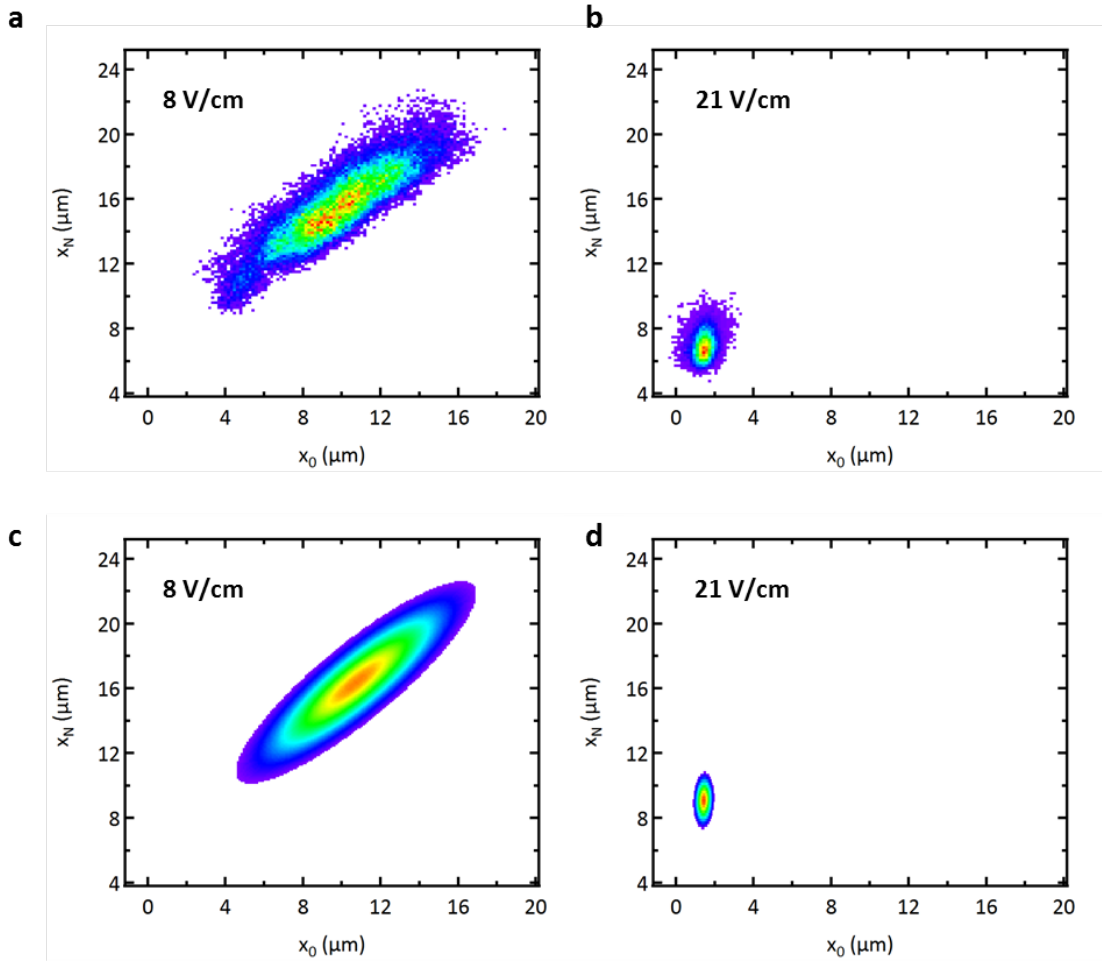
Figure 4.3: Comparison of experimental and theoretical x_0, x_N distributions for trapping of T4-phage DNA in the $\alpha = 0.45$ nanofunnel. a,b, Filled contour plots showing the probabilities of x_0, x_N values measured from each fluorescence image at the low field (8 V/cm) and high field (21 V/cm) limits of the stable trapping regime, respectively. c,d, Contour plots derived from the probability of displacement from the "equilibrium" position at the same low and high field conditions as (a,b) , respectively, as determined by calculating the work necessary for the displacement.
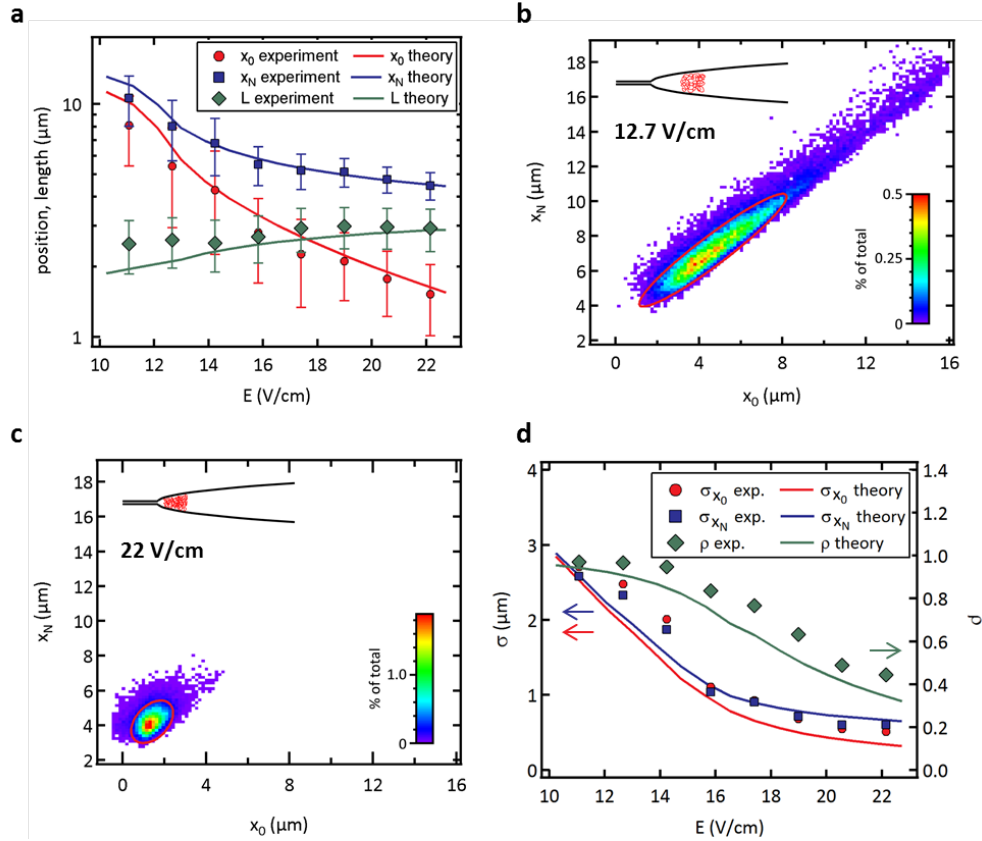
Figure 4.4: Electric field dependent average positions and fluctuations of λ- phage DNA molecules trapped in a three-dimensional (α=0.45) nanofunnel. a, Experimentally measured mean values of DNA end positions and length (symbols) at each electric field compared to the theoretically predicted values (curves). The error bars are the standard deviations of each measurement over the entire imaging period at a given electric field strength and thus include the contribution of thermal fluctuations. b,c, Filled contour plots showing the probabilities of x_0, x_N coordinates measured from each fluorescence image at the low field (12.7 V/cm) and high field (22 V/cm) limits of the stable trapping regime, respectively. The color scales indicate the percentage of measurements corresponding to the various x_0, x_N pairs. The insets show schematically the DNA conformations (position, length, packing density) associated with these operating conditions. The red ellipses indicate the best-fit bivariate normal distributions (2σ) to the data. d, Comparison of parameters of the bivariate normal distribution fitting analysis of the experimental data (symbols) and theoretical probability distributions (curves). Changes in the positional standard deviations reflect a decrease in thermal fluctuations at increased field strengths (i.e., stronger trapping). These fluctuations are highly correlated ($\rho > 0.95$) at low field strengths as the molecule diffuses along the nanofunnel's longitudinal axis.
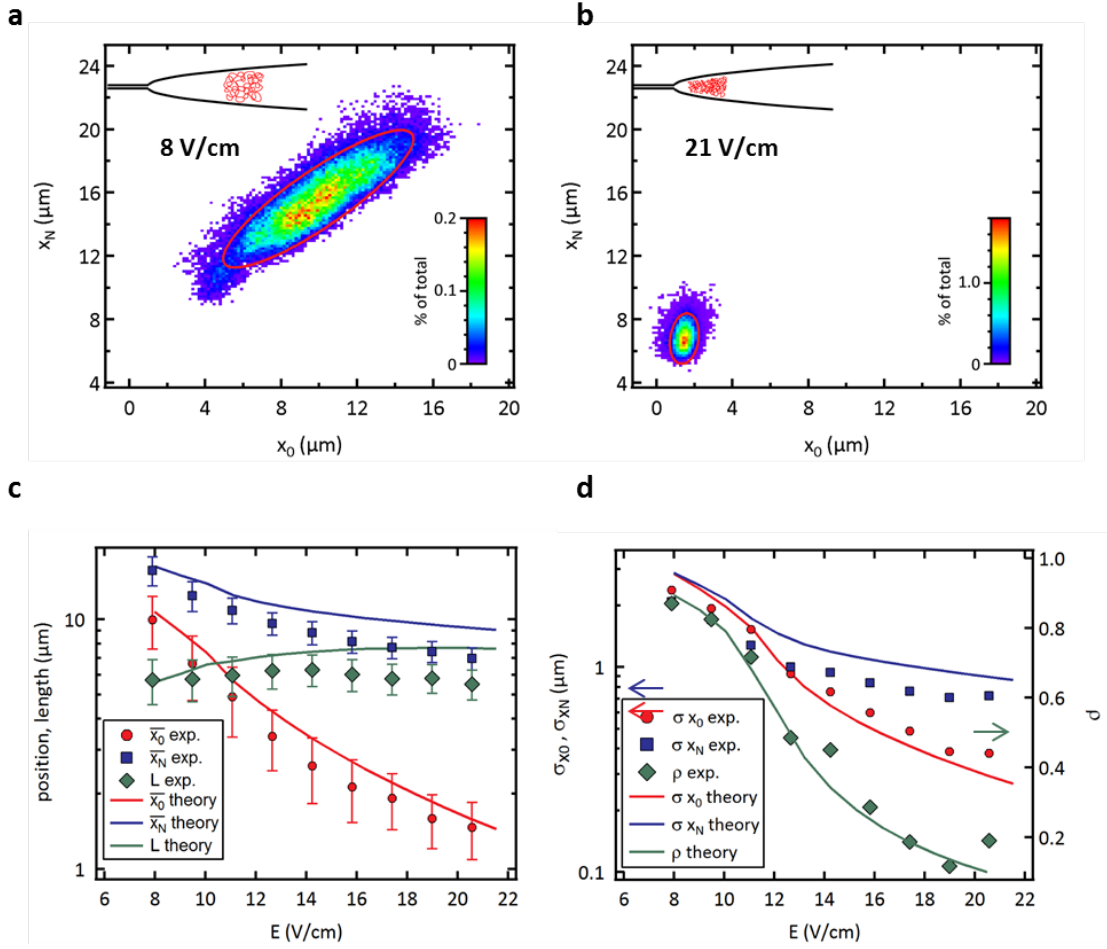
Figure 4.5: Electric field dependent average positions and fluctuations of T4 -phage DNA molecules trapped in a three-dimensional (α=0.45) nanofunnel. a,b, Filled contour plots showing the probabilities of x_0, x_N coordinates measured from each fluorescence image at the low field (8 V/cm) and high field (21 V/cm) limits of the stable trapping regime, respectively. The color scales indicate the percentage of measurements corresponding to the various x_0, x_N pairs. The insets show schematically the DNA conformations (position, length, packing density) associated with these operating conditions. The red ellipses indicate the best-fit bivariate normal distributions (2σ) to the data. c, Experimentally measured mean values of DNA end positions and length (markers) at each electric field compared to the theoretically predicted values (curves). d, Comparison of parameters of the bivariate normal distribution fitting analysis of the experimental data (markers) and theoretical probability distributions (curves).
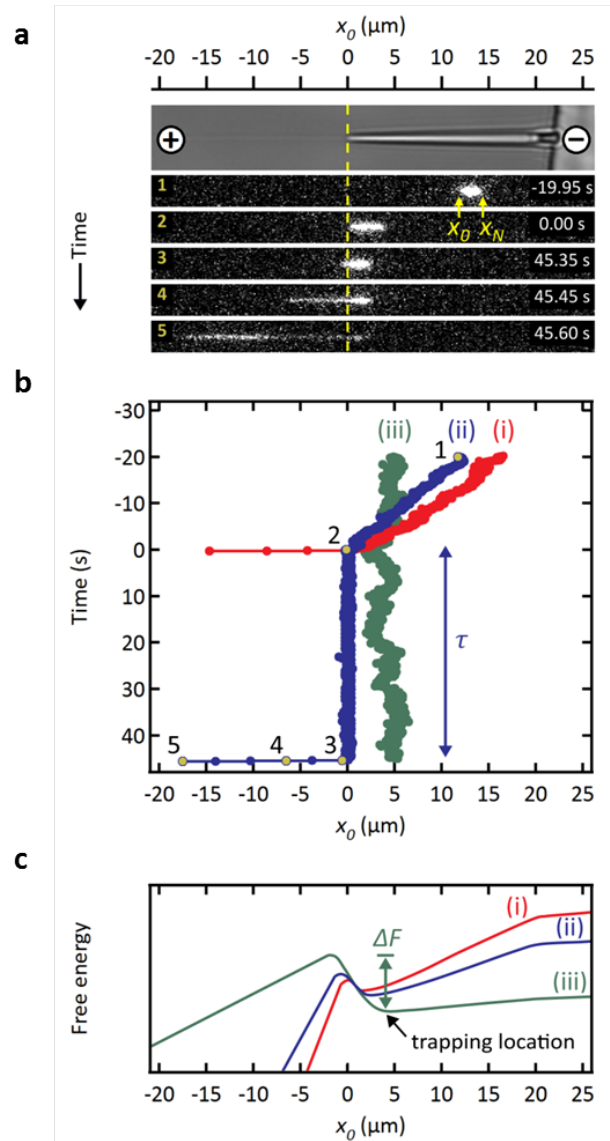
Figure 4.6: Measurement of DNA molecules within a three-dimensional nanofunnel. a, Representative images recording the position and conformation of a λ-phage DNA molecule at various time points as it is electrokinetically driven from right to left through a nanofunnel and into the associated nanochannel. The top panel is a bright-field image showing the position of the nanofunnel (positive x coordinates) and nanochannel (negative x coordinates) and the voltage polarity applied across the nanofunnel- nanochannel device. The numbered frames (1-5) are fluorescence images of the DNA molecule stained with an intercalating dye recorded at the indicated time points. Image analysis determined the positions of the molecule's leading (x_0) and trailing (x_N) ends at each time point. b, The position of a molecules leading end within a nanofunnel measured at three different nanochannel electric field strengths: 77.5 V/cm (red line, i), 54.3 V/cm (blue line, ii), and 15.5 V/cm (green line, iii). The blue line (ii) represents behavior at an intermediate electric field strength where the DNA molecule has a finite residence time ($\tau = 47$ s) at the nanochannel entrance prior to entry. The numbered orange circles indicate the leading edge measured from the numbered fluorescence images in (a). c, Relative effective free energies at different nanochannel electric field strengths of a DNA molecule as a function of its leading end position within the nanofunnel-nanochannel. The line colors and labels correspond to the same electric field conditions as in (b). As the electric field strength decreases the energy barrier to nanochannel entry (ΔF) increases and the energy minimum, which corresponds to a trapping location, moves away from the nanochannel entrance towards the nanofunnel mouth.
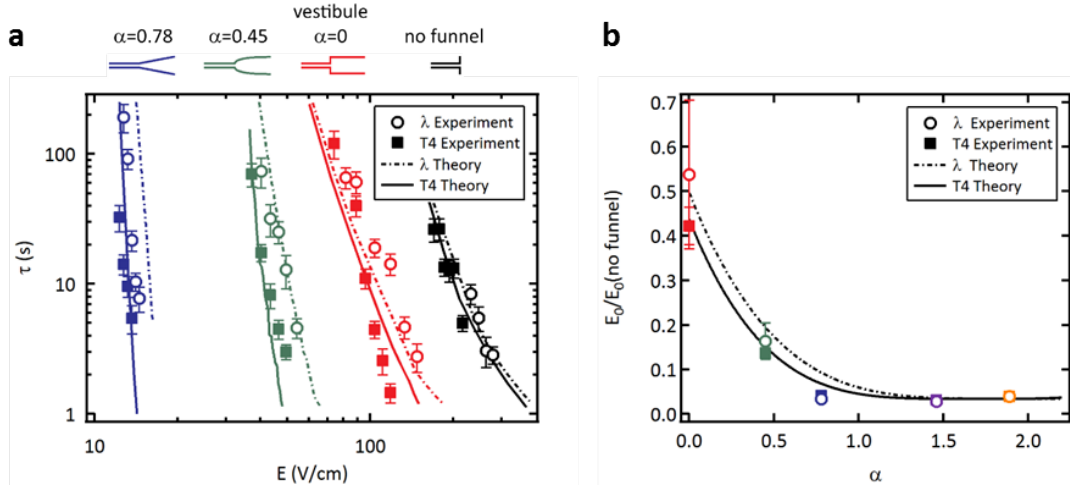
75

Figure 4.7: Residence time measurements and threshold electric field reduction by nanofunnels. a, Mean residence times measured at various nanochannel electric field strengths in three different nanofunnels (defined by α=0.78, α=0.45, and α=0; see Equation 2) and in the absence of a nanofunnel. Each data set is associated with the nanofunnel indicated directly above it in the figure and is color coded accordingly. Data were collected using stained λ-phage (48.5 kbp, open circles) and T4- phage (165.6 kbp, filled squares) DNA molecules. The error bars indicate the standard deviations of at least 20 independent measurements per experimental data point. The curves represent the best fit of the theoretical model to these experimental data. b, Extrapolating the experimental electric field data in (a) to the characteristic relaxation time τ_0=6 ms results in the characteristic threshold electric field strength (normalized to the threshold electric field strength measured in the absence of a nanofunnel) for each of the three nanofunnels (red, green, and blue symbols obtained from the data in (a) of the same colors). The solid and dashed black lines are interpolations of theoretical values calculated for T4-phage and λ-phage DNA, respectively, over a wider range of α values. The theoretical predictions were tested by measuring the electric field strengths required to thread DNA molecules through nanofunnels where α=1.46 and α=1.89 (purple and orange symbols, respectively). The error bars indicate the 68% (1σ) confidence level of the threshold electric field strengths determined from the experimental data and are smaller than the symbols for the results from nanofunnels where α >0.45.

REFERENCES

[1] Akahori, R., Haga, T., Hatano, T., Yanagi, I., Ohura, T., Hamamura, H., Iwasaki, T., Yokoi, T., and Anazawa, T. (2014). Slowing single-stranded dna translocation through a solid-state nanopore by decreasing the nanopore diameter. *Nanotechnology*, 25(27).

[2] Akca, S., Foroughi, A., Frochtzwajg, D., and Postma, H. W. (2011). Competing interactions in dna assembly on graphene. *PLoS One*, 6(4):e18442.

[3] Akeson, M., Branton, D., Kasianowicz, J. J., Brandin, E., and Deamer, D. W. (1999). Microsecond time-scale discrimination among polycytidylic acid, polyadenylic acid, and polyuridylic acid as homopolymers or as segments within single rna molecules. *Biophys J*, 77(6):3227–33.

[4] Aksimentiev, A., Heng, J. B., Timp, G., and Schulten, K. (2004). Microscopic kinetics of dna translocation through synthetic nanopores. *Biophys J*, 87(3):2086–97.

[5] Anderson, B. N., Muthukumar, M., and Meller, A. (2013). ph tuning of dna translocation time through organically functionalized nanopores. *ACS Nano*, 7(2):1408–14.

[6] Andrey V. Dobrynin, M. R. (2005). Theory of polyelectrolytes in solutions and at surfaces. *Prog. Polym. Sci.*, 30:1049–1118.

[7] Auger, T., Mathe, J., Viasnoff, V., Charron, G., Di Meglio, J. M., Auvray, L., and Montel, F. (2014). Zero-mode waveguide detection of flow-driven dna translocation through nanopores. *Phys Rev Lett*, 113(2):028302.

[8] Ausserre, D. (1989). Polymer melt confined between 2 plates. *Journal De Physique*, 50(19):3021–3042. At355 Times Cited:29 Cited References Count:26.

[9] Bhattacharya, A. and Binder, K. (2010). Out-of-equilibrium characteristics of a forced translocating chain through a nanopore. *Physical Review E*, 81(4).

[10] Bhattacharya, A., Morrison, W. H., Luo, K., Ala-Nissila, T., Ying, S. C., Milchev, A., and Binder, K. (2009). Scaling exponents of forced polymer translocation through a nanopore. *European Physical Journal E*, 29(4):423–429.

[11] Branton, D., Deamer, D. W., Marziali, A., Bayley, H., Benner, S. A., Butler, T., Di Ventra, M., Garaj, S., Hibbs, A., Huang, X., Jovanovich, S. B., Krstic, P. S., Lindsay, S., Ling, X. S., Mastrangelo, C. H., Meller, A., Oliver, J. S., Pershin, Y. V., Ramsey, J. M., Riehn, R., Soni, G. V., Tabard-Cossa, V., Wanunu, M., Wiggin, M., and Schloss, J. A. (2008). The potential and challenges of nanopore sequencing. *Nat Biotechnol*, 26(10):1146–53.

[12] Branton, D. and Meller, A. (2002). Using nanopores to discriminate between single molecules of dna. *Structure and Dynamics of Confined Polymers*, 87:177–185.

[13] Bustamante, C., Bryant, Z., and Smith, S. B. (2003). Ten years of tension: single-molecule dna mechanics. *Nature*, 421(6921):423–7.

[14] Chang, S., Huang, S., He, J., Liang, F., Zhang, P., Li, S., Chen, X., Sankey, O., and Lindsay, S. (2010). Electronic signatures of all four dna nucleosides in a tunneling gap. *Nano Lett*, 10(3):1070–5.

[15] Chen, P., Mitsui, T., Farmer, D. B., Golovchenko, J., Gordon, R. G., and Branton, D. (2004). Atomic layer deposition to fine-tune the surface properties and diameters of fabricated nanopores. *Nano Letters*,

4(7):1333–1337.

[16] Cherf, G. M., Lieberman, K. R., Rashid, H., Lam, C. E., Karplus, K., and Akeson, M. (2012). Automated forward and reverse ratcheting of dna in a nanopore at 5-a precision. *Nat Biotechnol*, 30(4):344–8.

[17] Dai, L. & Doyle, P. (2013). Comparisons of a polym er in confinement verus applied force. *Macromolecules*, 46:6336–6344.

[18] de Zoysa, R. S., Jayawardhana, D. A., Zhao, Q., Wang, D., Armstrong, D. W., and Guan, X. (2009). Slowing dna translocation through nanopores using a solution containing organic salts. *J Phys Chem B*, 113(40):13332–6.

[19] Dekker, C. (2007). Solid-state nanopores. *Nature Nanotechnology*, 2(4):209–215.

[20] Deng, T., Li, M. W., Wang, Y. F., and Liu, Z. W. (2015). Development of solid-state nanopore fabrication technologies. *Science Bulletin*, 60(3):304–319.

[21] Dobrynin, A. V. (2006). Effect of counterion condensation on rigidity of semiflexible polyelectrolytes. *Macromolecules*, 39(26):9519–9527.

[22] Fanget, A., Traversi, F., Khlybov, S., Granjon, P., Magrez, A., Forro, L., and Radenovic, A. (2014). Nanopore integrated nanogaps for dna detection. *Nano Letters*, 14(1):244–249.

[23] Farimani, A. B., Min, K., and Aluru, N. R. (2014). Dna base detection using a single-layer mos2. *ACS Nano*, 8(8):7914–22.

[24] Feng, J., Liu, K., Graf, M., Lihter, M., Bulushev, R. D., Dumcenco, D., Alexander, D. T. L., Krasnozhon, D., Vuletic, T., Kis, A., and Radenovic, A. (2015). Electrochemical reaction in single layer mos2: Nanopores opened atom by atom. *Nano Letters*, 15(5):3431–3438.

[25] Fologea, D., Uplinger, J., Thomas, B., McNabb, D. S., and Li, J. (2005). Slowing dna translocation in a solid-state nanopore. *Nano Lett*, 5(9):1734–7.

[26] Fuller, D. N., Gemmen, G. J., Rickgauer, J. P., Dupont, A., Millin, R., Recouvreux, P., and Smith, D. E. (2006). A general method for manipulating dna sequences from any organism with optical tweezers. *Nucleic Acids Research*, 34(2).

[27] Fyta, M., Melchionna, S., and Succi, S. (2011). Translocation of biomolecules through solid-state nanopores: Theory meets experiments. *Journal of Polymer Science Part B-Polymer Physics*, 49(14):985–1011.

[28] Galla, L., Meyer, A. J., Spiering, A., Sischka, A., Mayer, M., Hall, A. R., Reimann, P., and Anselmetti, D. (2014). Hydrodynamic slip on dna observed by optical tweezers-controlled translocation experiments with solid-state and lipid-coated nanopores. *Nano Lett*, 14(7):4176–82.

[29] Gauthier, M. G. and Slater, G. W. (2008). A monte carlo algorithm to study polymer translocation through nanopores. i. theory and numerical approach. *Journal of Chemical Physics*, 128(6).

[30] Granick, S. and Rubinstein, M. (2004). Polymers: a multitude of macromolecules. *Nat Mater*, 3(9):586–7.

[31] Grosberg, A. Y. and Rabin, Y. (2010). Dna capture into a nanopore: Interplay of diffusion and electrohydrodynamics. *Journal of Chemical Physics*, 133(16).

[32] Gu, Z. L., Zhang, Y. Z., Luan, B. Q., and Zhou, R. H. (2016). Dna translocation through single-layer boron nitride nanopores. *Soft Matter*, 12(3):817–823.

[33] Gunther, K., Mertig, M., and Seidel, R. (2010). Mechanical and structural properties of yoyo-1 complexed dna. *Nucleic Acids Res*, 38(19):6526–32.

[34] Guo, B. Y., Zeng, T., and Wu, H. C. (2015). Recent advances of dna sequencing via nanopore-based technologies. *Science Bulletin*, 60(3):287–295.

[35] Hall, A. R., van Dorp, S., Lemay, S. G., and Dekker, C. (2009). Electrophoretic force on a protein-coated dna molecule in a solid-state nanopore. *Nano Lett*, 9(12):4441–5.

[36] Henrickson, S. E., Misakian, M., Robertson, B., and Kasianowicz, J. J. (2000). Driven dna transport into an asymmetric nanometer-scale pore. *Physical Review Letters*, 85(14):3057–3060.

[37] Hoogerheide, D. P., Lu, B., and Golovchenko, J. A. (2014). Pressure-voltage trap for dna near a solid-state nanopore. *ACS Nano*, 8(7):7384–91.

[38] Hu, H., Banerjee, S., Estrada, D., Bashir, R., and King, W. P. (2015). Tip-based nanofabrication of arbitrary shapes of graphene nanoribbons for device applications. *Rsc Advances*, 5(46):37006–37012.

[39] Huang, S., He, J., Chang, S., Zhang, P., Liang, F., Li, S., Tuchband, M., Fuhrmann, A., Ros, R., and Lindsay, S. (2010). Identifying single bases in a dna oligomer with electron tunnelling. *Nat Nanotechnol*, 5(12):868–73.

[40] Huopaniemi, I., Luo, K. F., Ala-Nissila, T., and Ying, S. C. (2007). Polymer translocation through a nanopore under a pulling force. *Physical Review E*, 75(6).

[41] Ikonen, T., Bhattacharya, A., Ala-Nissila, T., and Sung, W. (2012). Unifying model of driven polymer translocation. *Physical Review E*, 85(5).

[42] Jain, M., Fiddes, I. T., Miga, K. H., Olsen, H. E., Paten, B., and Akeson, M. (2015). Improved data analysis for the minion nanopore sequencer. *Nature Methods*, 12(4):351–U115.

[43] Kasianowicz, J. J., Brandin, E., Branton, D., and Deamer, D. W. (1996). The detection of individual nucleic acid polymers traversing a protein ion channel. *Progress in Biophysics & Molecular Biology*, 65:Pb127–Pb127. Suppl. 1 We753 Times Cited:0 Cited References Count:0.

[44] Keyser, U. F., Koeleman, B. N., Van Dorp, S., Krapf, D., Smeets, R. M. M., Lemay, S. G., Dekker, N. H., and Dekker, C. (2006a). Direct force measurements on dna in a solid-state nanopore. *Nature Physics*, 2(7):473–477.

[45] Keyser, U. F., van der Does, J., Dekker, C., and Dekker, N. H. (2006b). Optical tweezers for force measurements on dna in nanopores. *Review of Scientific Instruments*, 77(10).

[46] Kim, Y., Kim, E. S., Lee, Y., Kim, J. H., Shim, B. C., Cho, S. M., Lee, J. S., and Park, J. W. (2014). Reading single dna with dna polymerase followed by atomic force microscopy. *Journal of the American Chemical Society*, 136(39):13754–13760.

[47] Kowalczyk, S. W., Wells, D. B., Aksimentiev, A., and Dekker, C. (2012). Slowing down dna translocation through a nanopore in lithium chloride. *Nano Lett*, 12(2):1038–44.

[48] Krasilnikov, O. V., Rodrigues, C. G., and Bezrukov, S. M. (2006). Single polymer molecules in a protein nanopore in the limit of a strong polymer-pore attraction. *Physical Review Letters*, 97(1).

[49] Lagerqvist, J., Zwolak, M., and Di Ventra, M. (2006). Fast dna sequencing via transverse electronic transport. *Nano Lett*, 6(4):779–82.

[50] Lagerqvist, J., Zwolak, M., and Di Ventra, M. (2007). Influence of the environment and probes on rapid dna sequencing via transverse electronic transport. *Biophys J*, 93(7):2384–90.

[51] Lam, E. T., Hastie, A., Lin, C., Ehrlich, D., Das, S. K., Austin, M. D., Deshpande, P., Cao, H., Nagarajan, N., Xiao, M., and Kwok, P. Y. (2012). Genome mapping on nanochannel arrays for structural variation analysis and sequence assembly. *Nature Biotechnology*, 30(8):771–776.

[52] Larkin, J., Henley, R., Bell, D. C., Cohen-Karni, T., Rosenstein, J. K., and Wanunu, M. (2013). Slow dna transport through nanopores in hafnium oxide membranes. *ACS Nano*, 7(11):10121–8.

[53] Lee, N., Obukhov, S., and Rubinstein, M. (1996). Deterministic model of dna gel electrophoresis in strong electric fields. *Electrophoresis*, 17(6):1011–7.

[54] Leggett, R. M., Heavens, D., Caccamo, M., Clark, M. D., and Davey, R. P. (2016). Nanook: multi-reference alignment analysis of nanopore sequencing data, quality and error profiles. *Bioinformatics*, 32(1):142–144.

[55] Lehtola, V. V., Linna, R. P., and Kaski, K. (2010). Unforced polymer translocation compared to the forced case. *Physical Review E*, 81(3).

[56] Lemay, S. G., van den Broek, D. M., Storm, A. J., Krapf, D., Smeets, R. M., Heering, H. A., and Dekker, C. (2005). Lithographically fabricated nanopore-based electrodes for electrochemistry. *Anal Chem*, 77(6):1911–5.

[57] Levy, S. L. and Craighead, H. G. (2010). Dna manipulation, sorting, and mapping in nanofluidic systems. *Chem Soc Rev*, 39(3):1133–52.

[58] Li, J., Yu, D. P., and Zhao, Q. (2016). Solid-state nanopore-based dna single molecule detection and sequencing. *Microchimica Acta*, 183(3):941–953.

[59] Liang, X. G. and Chou, S. Y. (2008). Nanogap detector inside nanofluidic channel for fast real-time label-free dna analysis. *Nano Letters*, 8(5):1472–1476.

[60] Lindsay, S. (2016). The promises and challenges of solid-state sequencing. *Nature Nanotechnology*, 11(2):109–111.

[61] Liu, K., Feng, J., Kis, A., and Radenovic, A. (2014). Atomically thin molybdenum disulfide nanopores with high sensitivity for dna translocation. *ACS Nano*, 8(3):2504–11.

[62] Liu, S., Lu, B., Zhao, Q., Li, J., Gao, T., Chen, Y., Zhang, Y., Liu, Z., Fan, Z., Yang, F., You, L., and Yu, D. (2013). Boron nitride nanopores: highly sensitive dna single-molecule detectors. *Adv Mater*, 25(33):4549–54.

[63] Long, D., Viovy, J. L., and Ajdari, A. (1996). Simultaneous action of electric fields and nonelectric forces on a polyelectrolyte: Motion and deformation. *Physical Review Letters*, 76(20):3858–3861.

[64] Lu, B., Hoogerheide, D. P., Zhao, Q., Zhang, H., Tang, Z., Yu, D., and Golovchenko, J. A. (2013). Pressure-controlled motion of single polymers through solid-state nanopores. *Nano Lett*, 13(7):3048–52.

[65] Luan, B., Stolovitzky, G., and Martyna, G. (2012). Slowing and controlling the translocation of dna in a solid-state nanopore. *Nanoscale*, 4(4):1068–77.

[66] Lubensky, D. K. and Nelson, D. R. (1999). Driven polymer translocation through a narrow pore. *Biophys J*, 77(4):1824–38.

[67] Luo, K. F., Ala-Nissila, T., Ying, S. C., and Bhattacharya, A. (2008). Sequence dependence of dna translocation through a nanopore. *Physical Review Letters*, 100(5).

[68] M. Daoud, P. D. G. (1977). Statistics of macromolecular solutions trapped in small pores. *Journal de Physique*, 38(1):85–93.

[69] M. Doi, S. F. E. (1986). *The Theory of Polymer Dynamics*. The International Series of Monographs on Physics. Oxford University Press, New York.

[70] Manning, G. S. (1981). Limiting laws and counterion condensation in poly-electrolyte solutions .6. theory of the titration curve. *Journal of Physical Chemistry*, 85(7):870–877. Lk187 Times Cited:94 Cited References Count:24.

[71] Manrao, E. A., Derrington, I. M., Laszlo, A. H., Langford, K. W., Hopper, M. K., Gillgren, N., Pavlenok, M., Niederweis, M., and Gundlach, J. H. (2012). Reading dna at single-nucleotide resolution with a mutant mspa nanopore and phi29 dna polymerase. *Nat Biotechnol*, 30(4):349–53.

[72] Mardis, E. R. (2011). A decade's perspective on dna sequencing technology. *Nature*, 470(7333):198–203.

[73] McNally, B., Singer, A., Yu, Z., Sun, Y., Weng, Z., and Meller, A. (2010). Optical recognition of converted dna nucleotides for single-molecule dna sequencing using nanopore arrays. *Nano Lett*, 10(6):2237–44.

[74] Meller, A., Nivon, L., Brandin, E., Golovchenko, J., and Branton, D. (2000). Rapid nanopore discrimination between single polynucleotide molecules. *Proc Natl Acad Sci U S A*, 97(3):1079–84.

[75] Meller, A., Nivon, L., and Branton, D. (2001). Voltage-driven dna translocations through a nanopore. *Phys Rev Lett*, 86(15):3435–8.

[76] Menard, L. D. and Ramsey, J. M. (2013). Electrokinetically-driven transport of dna through focused ion beam milled nanofluidic channels. *Analytical Chemistry*, 85(2):1146–1153.

[77] Michael Rubinstein, R. H. C. (2003). *Polymer Physics*. OUP Oxford.

[78] Mikheyev, A. S. and Tin, M. M. Y. (2014). A first look at the oxford nanopore minion sequencer. *Molecular Ecology Resources*, 14(6):1097–1102.

[79] Min, S. K., Kim, W. Y., Cho, Y., and Kim, K. S. (2011). Fast dna sequencing with a graphene-based nanochannel device. *Nature Nanotechnology*, 6(3):162–165.

[80] Mirsaidov, U., Comer, J., Dimitrov, V., Aksimentiev, A., and Timp, G. (2010). Slowing the translocation of double-stranded dna using a nanopore smaller than the double helix. *Nanotechnology*, 21(39):395501.

[81] Murade, C. U., Subramaniam, V., Otto, C., and Bennink, M. L. (2009). Interaction of oxazole yellow dyes with dna studied with hybrid optical tweezers and fluorescence microscopy. *Biophys J*, 97(3):835–43.

[82] Muthukumar, M. (2010). Theory of capture rate in polymer translocation. *Journal of Chemical Physics*, 132(19).

[83] Muthukumar, M. (2011). *Polymer Translocation*. CRC Press.

[84] Nakane, J. J., Akeson, M., and Marziali, A. (2003). Nanopore sensors for nucleic acid analysis. *Journal*

of Physics-Condensed Matter, 15(32):R1365–R1393.

[85] Nam, S. W., Rooks, M. J., Kim, K. B., and Rossnagel, S. M. (2009). Ionic field effect transistors with sub-10 nm multiple nanopores. *Nano Lett*, 9(5):2044–8.

[86] Odijk, T. (1983). On the statistics and dynamics of confined or entangled stiff polymers. *Macromolecules*, 16(8):1340–1344. Rd787 Times Cited:314 Cited References Count:42.

[87] Odijk, T. (2006). Dna confined in nanochannels: Hairpin tightening by entropic depletion. *Journal of Chemical Physics*, 125(20).

[88] Odijk, T. (2008). Scaling theory of dna confined in nanochannels and nanoslits. *Physical Review E*, 77(6).

[89] Ohshiro, T., Matsubara, K., Tsutsui, M., Furuhashi, M., Taniguchi, M., and Kawai, T. (2012). Single-molecule electrical random resequencing of dna and rna. *Sci Rep*, 2:501.

[90] Olasagasti, F., Lieberman, K. R., Benner, S., Cherf, G. M., Dahl, J. M., Deamer, D. W., and Akeson, M. (2010). Replication of individual dna molecules under electronic control using a protein nanopore. *Nat Nanotechnol*, 5(11):798–806.

[91] Osaki, T., Suzuki, H., Le Pioufle, B., and Takeuchi, S. (2009). Multichannel simultaneous measurements of single-molecule translocation in alpha-hemolysin nanopore array. *Anal Chem*, 81(24):9866–70.

[92] Peng, H. and Ling, X. S. (2009). Reverse dna translocation through a solid-state nanopore by magnetic tweezers. *Nanotechnology*, 20(18):185101.

[93] Persson, F., Utko, P., Reisner, W., Larsen, N. B., and Kristensen, A. (2009). Confinement spectroscopy: probing single dna molecules with tapered nanochannels. *Nano Lett*, 9(4):1382–5.

[94] Qing, Q., Chen, F., Li, P., Tang, W., Wu, Z., and Liu, Z. (2005). Finely tuning metallic nanogap size with electrodeposition by utilizing high-frequency impedance in feedback. *Angew Chem Int Ed Engl*, 44(47):7771–5. Qing, Quan Chen, Fang Li, Peigang Tang, Weihua Wu, Zhongyun Liu, Zhongfan eng Germany International ed. in English 2005/11/04 09:00 Angew Chem Int Ed Engl. 2005 Dec 2;44(47):7771-5.

[95] Reisner, W., Larsen, N. B., Silahtaroglu, A., Kristensen, A., Tommerup, N., Tegenfeldt, J. O., and Flyvbjerg, H. (2010). Single-molecule denaturation mapping of dna in nanofluidic channels. *Proc Natl Acad Sci U S A*, 107(30):13294–9.

[96] Reisner, W., Morton, K. J., Riehn, R., Wang, Y. M., Yu, Z., Rosen, M., Sturm, J. C., Chou, S. Y., Frey, E., and Austin, R. H. (2005). Statics and dynamics of single dna molecules confined in nanochannels. *Phys Rev Lett*, 94(19):196101.

[97] Reisner, W., Pedersen, J. N., and Austin, R. H. (2012). Dna confinement in nanochannels: physics and biological applications. *Reports on Progress in Physics*, 75(10).

[98] Riehn, R., Lu, M., Wang, Y. M., Lim, S. F., Cox, E. C., and Austin, R. H. (2005). Restriction mapping in nanofluidic devices. *Proc Natl Acad Sci U S A*, 102(29):10012–6.

[99] Rosenstein, J. K., Wanunu, M., Merchant, C. A., Drndic, M., and Shepard, K. L. (2012). Integrated nanopore sensing platform with sub-microsecond temporal resolution. *Nat Methods*, 9(5):487–92.

[100] Rowghanian, P. and Grosberg, A. Y. (2013). Two cases of reciprocal relations for electric and hy-

drodynamic currents: A rigid polymer in a nano-channel and a polyelectrolyte gel. *Journal of Chemical Physics*, 139(2).

[101] Rubinstein, M., Colby, R. H., and Dobrynin, A. V. (1994). Dynamics of semidilute polyelectrolyte solutions. *Phys Rev Lett*, 73(20):2776–2779. Rubinstein Colby Dobrynin ENG 1994/11/14 00:00 Phys Rev Lett. 1994 Nov 14;73(20):2776-2779.

[102] Rye, H. S., Yue, S., Wemmer, D. E., Quesada, M. A., Haugland, R. P., Mathies, R. A., and Glazer, A. N. (1992). Stable fluorescent complexes of double-stranded dna with bis-intercalating asymmetric cyanine dyes: properties and applications. *Nucleic Acids Res*, 20(11):2803–12.

[103] Sakaue, T. (2010). Sucking genes into pores: Insight into driven translocation. *Physical Review E*, 81(4).

[104] Sanger, F., Nicklen, S., and Coulson, A. R. (1977). Dna sequencing with chain-terminating inhibitors. *Proceedings of the National Academy of Sciences of the United States of America*, 74(12):5463–5467. Eh421 Times Cited:65890 Cited References Count:14.

[105] Sawafta, F., Clancy, B., Carlsen, A. T., Huber, M., and Hall, A. R. (2014). Solid-state nanopores and nanopore arrays optimized for optical detection. *Nanoscale*, 6(12):6991–6.

[106] Schaefer, D. W., Joanny, J. F., and Pincus, P. (1980). Dynamics of semiflexible polymers in solution. *Macromolecules*, 13(5):1280–1289. Km679 Times Cited:183 Cited References Count:37.

[107] Shafran, E., Yaniv, A., and Krichevsky, O. (2010). Marginal nature of dna solutions. *Physical Review Letters*, 104(12).

[108] Shi, J. D., Hou, J. F., and Fang, Y. (2016). Recent advances in nanopore-based nucleic acid analysis and sequencing. *Microchimica Acta*, 183(3):925–939.

[109] Singer, A., Wanunu, M., Morrison, W., Kuhn, H., Frank-Kamenetskii, M., and Meller, A. (2010). Nanopore based sequence specific detection of duplex dna for genomic profiling. *Nano Lett*, 10(2):738–42.

[110] Skinner, G. M., van den Hout, M., Broekmans, O., Dekker, C., and Dekker, N. H. (2009). Distinguishing single- and double-stranded nucleic acid molecules using solid-state nanopores. *Nano Lett*, 9(8):2953–60.

[111] Smeets, R. M., Keyser, U. F., Krapf, D., Wu, M. Y., Dekker, N. H., and Dekker, C. (2006). Salt dependence of ion transport and dna translocation through solid-state nanopores. *Nano Lett*, 6(1):89–95.

[112] Smeets, R. M. M., Kowalczyk, S. W., Hall, A. R., Dekker, N. H., and Dekker, C. (2009). Translocation of reca-coated double-stranded dna through solid-state nanopores. *Nano Letters*, 9(9):3089–3095.

[113] Stigter, D. (1977). Interactions of highly charged colloidal cylinders with applications to double-stranded. *Biopolymers*, 16(7):1435–48.

[114] Tang, Z., Lu, B., Zhao, Q., Wang, J., Luo, K., and Yu, D. (2014). Surface modification of solid-state nanopores for sticky-free translocation of single-stranded dna. *Small*, 10(21):4332–9.

[115] Trepagnier, E. H., Radenovic, A., Sivak, D., Geissler, P., and Liphardt, J. (2007). Controlling dna capture and propagation through artificial nanopores. *Nano Lett*, 7(9):2824–30.

[116] van Dorp, S., Keyser, U. F., Dekker, N. H., Dekker, C., and Lemay, S. G. (2009). Origin of the electrophoretic force on dna in solid-state nanopores. *Nature Physics*, 5(5):347–351.

[117] Venkatesan, B. M. and Bashir, R. (2011). Nanopore sensors for nucleic acid analysis. *Nat Nanotechnol*, 6(10):615–24.

[118] Wanunu, M., Morrison, W., Rabin, Y., Grosberg, A. Y., and Meller, A. (2010). Electrostatic focusing of unlabelled dna into nanoscale pores using a salt gradient. *Nat Nanotechnol*, 5(2):160–5.

[119] Wanunu, M., Sutin, J., McNally, B., Chow, A., and Meller, A. (2008). Dna translocation governed by interactions with solid-state nanopores. *Biophys J*, 95(10):4716–25.

[120] Wanunu, M., Sutin, J., and Meller, A. (2009). Dna profiling using solid-state nanopores: detection of dna-binding molecules. *Nano Lett*, 9(10):3498–502.

[W.R. Hogg] W.R. Hogg, W. C. Apparatus and method for measuring a dividing particle size of a particulate system.

[122] Xiao, M., Phong, A., Ha, C., Chan, T. F., Cai, D., Leung, L., Wan, E., Kistler, A. L., DeRisi, J. L., Selvin, P. R., and Kwok, P. Y. (2007). Rapid dna mapping by fluorescent single molecule detection. *Nucleic Acids Res*, 35(3):e16.

[123] Yeh, L. H., Zhang, M., Joo, S. W., and Qian, S. (2012). Slowing down dna translocation through a nanopore by lowering fluid temperature. *Electrophoresis*, 33(23):3458–65.

[124] Yusko, E. C., Johnson, J. M., Majd, S., Prangkio, P., Rollings, R. C., Li, J., Yang, J., and Mayer, M. (2011). Controlling protein translocation through nanopores with bio-inspired fluid walls. *Nat Nanotechnol*, 6(4):253–60.

[125] Zhang, H., Zhao, Q., Tang, Z., Liu, S., Li, Q., Fan, Z., Yang, F., You, L., Li, X., Zhang, J., and Yu, D. (2013). Slowing down dna translocation through solid-state nanopores by pressure. *Small*, 9(24):4112–7.

[126] Zhang, J. and Shklovskii, B. I. (2007). Effective charge and free energy of dna inside an ion channel. *Phys Rev E Stat Nonlin Soft Matter Phys*, 75(2 Pt 1):021906.

[127] Zhang, X. G., Krstic, P. S., Zikic, R., Wells, J. C., and Fuentes-Cabrera, M. (2006). First-principles transversal dna conductance deconstructed. *Biophys J*, 91(1):L04–6.

[128] Zhao, Y., Ashcroft, B., Zhang, P., Liu, H., Sen, S., Song, W., Im, J., Gyarfas, B., Manna, S., Biswas, S., Borges, C., and Lindsay, S. (2014). Single-molecule spectroscopy of amino acids and peptides by recognition tunnelling. *Nat Nanotechnol*, 9(6):466–73.

[129] Zhou J, Wang Y, M. L. P. S. R. M. R. J. (2016). Enhanced nanochannel translocation and localization of genomic dna molecules using three-dimensional nanofunnels.

[130] Zikic, R., Krstic, P. S., Zhang, X. G., Fuentes-Cabrera, M., Wells, J., and Zhao, X. (2006). Characterization of the tunneling conductance across dna bases. *Phys Rev E Stat Nonlin Soft Matter Phys*, 74(1 Pt 1):011919.